Ex Libris
Universitatis
Albertaensis

Digitized by the Internet Archive
in 2026 with funding from
University of Alberta Library

https://archive.org/details/0162004872238

UNIVERSITY OF ALBERTA

LIBRARY RELEASE FORM

NAME OF AUTHOR:	**Xiang Gui**
TITLE OF THESIS:	**Study of Diffusion Phenomena in VLSI Metallization Structures by the Transmission-Line Matrix Method**
DEGREE:	**Doctor of Philosophy**
YEAR THIS DEGREE GRANTED:	**1996**

Permission is hereby granted to the University of Alberta Library to reproduce single copies of this thesis and to lend or sell such copies for private, scholarly, or scientific research purposes only.

The author reserves all other publication and other rights in association with the copyright in the thesis, and expect as hereinbefore provided, neither the thesis nor any substantial portion thereof may be printed or otherwise reproduced in any material form whatever without the author's prior written permission.

University of Alberta

STUDY OF DIFFUSION PHENOMENA IN VLSI METALLIZATION STRUCTURES BY THE TRANSMISSION-LINE MATRIX METHOD

by

Xiang Gui

A thesis submitted to the Faculty of Graduate Studies and Research

in partial fulfillment of the requirements for the degree of Doctor of Philosophy

Department of Electrical Engineering

Edmonton, Alberta

Spring 1996

University of Alberta

Faculty of Graduate Studies and research

The undersigned certify that they have read, and recommend to the Faculty of Graduate Studies and Research for acceptance, a thesis entitled *Study of Diffusion Phenomena in VLSI Metallization Structures by the Transmission-Line Matrix Method* submitted by Xiang Gui in partial fulfillment of the requirements for the degree of Doctor of Philosophy.

Abstract

With the continuing trend of miniaturization of very large scale integrated (VLSI) devices, the technological problems associated with metallization have become of central concern. Considerable understanding of diffusion phenomena in thin films and microelectronic materials is required to overcome these problems. This thesis demonstrates the numerical solution to some fundamental and important diffusion problems in VLSI metallization structures. Compared with the analytical method and more traditional numerical techniques, the transmission-line matrix (TLM) approach is shown to be favorable for the simulation of diffusion processes as it can easily incorporate nonlinear properties, is numerically stable, computationally efficient and convenient for modeling complex geometries. Along with developments of the numerical routines, two main issues of practical engineering significance are discussed. The first is concerned with simulations of thermal diffusion, including steady-state analyses for generic high-density multilevel metallizations and transient analyses specifically important for interconnections used in field-programmable gate array (FPGA) devices with voltage programmable links (VPL's). The second deals

with the modeling of atomic diffusion processes in metallization systems. Grain-boundary diffusion and electromigration behavior in thin-film diffusion barriers have been studied by utilizing the TLM method for the first time. Moreover, it has been used in conjunction with a two-dimensional Monte Carlo film-growth simulator, so that the simulation of impurity diffusion in a thin-film diffusion barrier as well as the evaluation of its effectiveness can be performed with a realistic microstructure pertinent to a particular film growth technology. The present research would pave the way for further in-depth investigations into diffusion phenomena and provide valuable tools for optimizing VLSI metallization structures.

Acknowledgment

I would like to express my most grateful thanks to my supervisors, Dr. M. J. Brett and Dr. S. K. Dew, for their constant encouragement and unfailing enthusiasm throughout the course of the present work. They have provided me with valuable supervision and advice, and were willing to let me pursue my own directions. Without their help and inspiration, this project would have certainly been impossible.

I must acknowledge the Alberta Microelectronic Centre, the Natural Sciences and Engineering Council, the Micronet Network of Centres of Excellence, and the Electrical Engineering Department at the University of Alberta for financial assistance. Special thanks are due to Dr. D. de Cogan of the University of East Anglia, U.K., Dr. P. W. Webb of the University of Birmingham, U.K., and Dr. P. Enders of Max-Born-Institut, Germany, for many precious communications. I am also deeply indebted to Dr. R. P. W. Lawson, Dr. T. Smy, Dr. R. N. Tait, G. McKinnon, L. J. Friedrich, K. Robbie, T. Janacek, C. Shafai, M. Lam, T. Tran, D. A. Tilroe, N. Poon and all those who have helped me for my thesis work in one or another way.

Finally, a big thank you goes to my wife, Xiaoli Li, my son, my parents and my sister for their unlimited moral support and for cheering me on to the completion of this work.

Table of Contents

Chapter 1. Introduction 1

1.1 Metallization 1

1.2 Diffusion Phenomena in Metallization Structures 6

1.2.1 Thermal diffusion 6

1.2.2 Particle diffusion 7

1.3 Diffusion Modeling and Simulation 9

Chapter 2. TLM Basics 14

2.1 Introduction 14

2.2 Equivalent Circuit Model of Transmission Lines 17

2.3 Theoretical Background of TLM Diffusion Modeling 20

2.3.1 RC network vs TLM network 20

2.3.2 Diffusion equation vs lossy wave equation 23

2.4 Basic TLM Algorithm for Diffusion 24

Chapter 3. Numerical Aspects of TLM Diffusion Modeling 27

3.1 Introduction 27

3.2 Simple examples 28

3.3 Boundary Conditions 32

3.3.1 Boundaries defined by the voltage reflection coefficient 32

3.3.2 Boundaries defined by voltage sources 34

3.3.3 Matched-load boundaries 37

3.4 Variable Meshes 39

3.5 Nonlinearities 42

3.6 Multiple Dimensions 43

3.7 Time-Step Changes and Control 47

3.8 Extended TLM Diffusion Node 51

3.9 Dynamic Matrix Expansion 52

3.10 Concluding Comments 53

Chapter 4. Thermal Diffusion: Steady-State Analysis 54

4.1 Introduction 54

4.2 Statements of the Problem and Models 55

4.3 Results and Discussion 59

4.4 Conclusions 65

Chapter 5. Thermal Diffusion: Transient Analysis 66

5.1 Introduction 66

5.2 Models of Single-Level Metallization Systems 67

5.3 Results and Discussion 68

5.4 Energetic Transients in Multilevel Metallization Systems 74

5.5 Conclusion 77

Chapter 6. TLM Modeling Applied to Grain-Boundary Diffusion in Thin Films 78

6.1 Introduction 78

6.2 Grain-Boundary Diffusion Kinetics 80

6.3 Numerical Model for Grain-Boundary Diffusion 84

6.4 Calculated results and Discussion 86

6.5 Summary 95

Chapter 7. Three-Dimensional Simulation of Impurity Diffusion in Thin-Film Diffusion Barriers 97

7.1 Introduction 97

7.2 Physical Models 98

7.3 Results and Discussion 101

7.4 Conclusions 110

Chapter 8. Simulation of Electromigration in Thin-Film Diffusion Barriers 112

8.1 Introduction 112

8.2 Model Formulation 113

8.3 Results and Discussion 116

8.4 Summary 124

Chapter 9. Efficiency Evaluation of Diffusion Barriers with Microstructural Details 125

9.1 Introduction 125

9.2 Modeling Method 126

9.3 Results and Discussion 128

9.4 Concluding Comments 141

Chapter 10. Concluding Remarks 143

Appendix. Further Comments on a General Boundary Condition in TLM Diffusion Modeling 147

References 151

Vita and Publication List 168

Vita 168

Publication List 169

List of Tables

1.1	Trends in some device parameters	6
3.1	Directional notation for the 3D TLM diffusion algorithm	46
4.1	Some physical properties of selected materials	58
6.1	Grain-boundary and intra-grain diffusivities in thin films	81
9.1	Boundary conditions applied to diffusion barrier structures	128

List of Figures

1.1	Schematic cross-section of a VLSI metallization structure	3
1.2	Schematic of a diffusion-barrier layer	8
2.1	Three consecutive steps in the propagation of an input impulse	15
2.2	A circuit representation of a transmission-line segment	17
2.3	An RC network for diffusion modeling	20
2.4	One-dimensional TLM node	22
2.5	Incidence and reflection between adjacent nodes	25
3.1	Example 1: comparison of the analytical and TLM solutions	30
3.2	Example 2: comparison of the analytical and TLM solutions	31
3.3	Several commonly-used TLM boundary conditions	33
3.4	Constant and controlled voltage sources at boundaries	35
3.5	ML boundary and a special case of the mixed boundaries	36
3.6	Boundary concentration vs time for the ML boundary condition	38
3.7	Construction of a variable mesh	41

3.8 Mesh layout for a TLM thermal simulator 42

3.9 Single 2D and 3D TLM nodes 44

3.10 Cartesian coordinate with the numbers denoting the six orthogonal directions 45

3.11 Change of impedance and time step 48

3.12 Transients for constant and variable time steps 49

3.13 An extended TLM diffusion node 51

4.1 Single- and triple-level metallization lines 56

4.2 Temperature rise vs current density in single- and triple-level lines 59

4.3 Temperature distribution of single-level lines 60

4.4 Temperature distribution of triple-level lines with SiO_2 as ILD and PD 61

4.5 Temperature distribution of triple-level lines with Si_3N_4 as ILD and PD 63

4.6 Temperature rise in the triple-level metallization structure 64

5.1 Elemental cross-sections of metallization structures used in the simulation 68

5.2 Pulse width vs maximum current density of single-level Al lines 70

5.3 Transient temperature distributions under various passivation conditions 72

5.4 Temperature of Al lines vs pulse width for single- and triple-level structures 75

5.5 Pulse width vs maximum current density of triple-level Al lines 76

6.1 TEM image of a grain boundary in Au thin films 81

6.2 Grain-boundary diffusion kinetics A, B and C 83

6.3 Geometric model of grain-boundary and lattice diffusion 85

6.4 Concentration distribution ($D_b/D_g = 10^4$, $D_s/D_g = 10^4$, $D_i/D_s = 1$) 88

6.5 Concentration distribution ($D_b/D_g = 10^4$, $D_i/D_g = 10^3$, $D_s/D_g = 10$) 89

6.6 Concentration distribution ($D_b/D_g = 10^4$, $D_i/D_g = 10^4$, $D_s/D_g = 10$) 90
6.7 Average concentration vs distance (substrate effects) 92
6.8 Average concentration vs distance (substrate and interface effects) 93

7.1 2D and 3D models of grain-boundary diffusion in diffusion barriers 99
7.2 2D simulation results of concentration vs distance 102
7.3 3D simulation results of concentration vs distance 103
7.4 Comparisons of 2D and 3D simulations 105
7.5 2D and 3D average concentration at diffusion-barrier backside 106
7.6 Average backside concentration vs D_b/D_g 109

8.1 2D simulation results of concentration vs distance 117
8.2 3D simulation results of concentration vs distance 119
8.3 2D average concentration vs vertical distance 120
8.4 3D average concentration vs vertical distance 121
8.5 Average backside concentration vs time 123

9.1 A simplified test microstructure of diffusion barriers 129
9.2 Steady-state impurity concentration vs α for the structure in Fig. 9.1 132
9.3 Impurity penetration vs time for the structure in Fig. 9.1 134
9.4 Impurity penetration vs position at steady state for the structure in Fig. 9.1 134
9.5 GROFILMS-generated diffusion-barrier microstructure 137
9.6 SEM photograph of TiW thin films deposited by sputtering 138
9.7 Impurity penetration vs time for the structure in Fig 9.5 139
9.8 Impurity penetration vs position at steady state for the structure in Fig. 9.5 139

9.9 Concentration distribution at steady state for the structure in Fig. 9.5 140

A.1 Termination of a TLM network with a boundary resistor 148

List of Symbols and Acronyms

Below is a list of common symbols and acronyms employed in the thesis. Several symbols may have different meanings in different chapters or sections, where this occurs, they are clearly defined and the significance can be known from the context. Some occasionally-occurring symbols are not listed, and are instead defined within the body of the text where they are used.

Symbols

C	-	concentration
	-	capacitance
C_d	-	distributed capacitance
D	-	diffusion coefficient
D_b	-	film grain-boundary diffusion coefficient
D_g	-	film lattice diffusion coefficient
D_i	-	film/substrate interfacial diffusion coefficient
D_s	-	substrate lattice diffusion coefficient

d	-	penetration distance of diffusing species
d_g	-	penetration distance into grains
d_b	-	grain-boundary penetration distance
$\mathcal{E}$	-	electric field
ΔE	-	activation energy
G	-	conductance
G_d	-	distributed conductance
g_m	-	transconductance for a controlled voltage source
I	-	current
J	-	current density
k	-	Boltzmann's constant
L	-	inductance
	-	half of the average spacing between grain boundaries
L_d	-	distributed inductance
l	-	diffusion-barrier thickness
Δl	-	elemental length
m	-	error parameter for TLM diffusion modeling (1)
R	-	resistance
	-	universal gas constant
R_d	-	distributed resistance
T	-	temperature
	-	reduced time for grain-boundary diffusion
t	-	time
Δt	-	time step

V	-	voltage
V_c	-	magnitude of constant voltage source
V_b	-	magnitude of boundary voltage source
${}_kV_L{}^i(n)$	-	voltage pulse incident on node n from the left-hand side at the kth time step
${}_kV_R{}^i(n)$	-	voltage pulse incident on node n from the right-hand side at the kth time step
${}_kV_L{}^s(n)$	-	voltage pulse scattered on node n from the left-hand side at the kth time step
${}_kV_R{}^s(n)$	-	voltage pulse scattered on node n from the right-hand side at the kth time step
v	-	velocity of impulses traveling along transmission lines
	-	drift velocity under an electric field
X	-	reduced position in the x direction
Δx	-	elemental distance in the x direction
Y	-	reduced position in the y direction
Δy	-	elemental distance in the y direction
Z	-	reduced position in the z direction
	-	characteristic impedance of transmission lines
Δz	-	elemental distance in the z direction

Greek Symbols

α	-	out-diffusion velocity in the mixed boundary condition
β	-	ratio of time steps (or ratio of impedances)

γ	-	factor of electric field
δ	-	average grain-boundary width
ε	-	error parameter for TLM diffusion modeling (2)
ζ	-	reduced diffusion time
θ	-	normalized electromigration extent
θ_f	-	metal fracture temperature
Λ	-	error parameter for TLM diffusion modeling (3)
ρ	-	reflection coefficient of voltage pulses
	-	electrical resistivity
τ	-	transmission coefficient of voltage pulses
Φ	-	potential
${}_k\Phi(n)$	-	potential of node n at the kth time step

Acronyms

ARM	-	Anti-Reflective Material
CVS	-	Constant Voltage Source
DB	-	Diffusion Barrier
EOS	-	Electrical OverStress
FD	-	Finite Difference
FE	-	Finite Element
FET	-	Field-Effect Transistor
FPGA	-	Field-Programmable Gate Array
GROFILMS	-	GRain Oriented FILm Microstructure Simulator
ILD	-	Inter-Level Dielectrics

LI	-	Local Interconnect
ML	-	Matched Load
MOS	-	Metal-Oxide-Semiconductor
MTF	-	Median Time to Failure
OC	-	Open Circuit
PD	-	Passivation Dielectrics
PDE	-	Partial Differential Equation
SC	-	Short Circuit
SEM	-	Scanning Electron Microscope
TEM	-	Transmission Electron Microscope
TLM	-	Transmission-Line Matrix
VLSI	-	Very Large Scale Integration
VPL	-	Voltage Programmable Link

1D	-	one-dimensional
2D	-	two-dimensional
3D	-	three-dimensional

Chapter 1

Introduction

1.1 Metallization

It is well known that the electrically active regions of today's electronic devices are made of Si, GaAs, InP or other semiconductor materials. For electrical accessibility, some form of conductive metal films for contacts and interconnections are required. A variety of different bipolar and field-effect transistor (FET) technologies, such as integrated injection logic (I^2L), emitter coupled logic (ECL), Schottky transistor logic (STL), n-channel metal-oxide-semiconductor (NMOS), complementary MOS (CMOS), and bipolar CMOS (BiCMOS), have been used for very large scale integration (VLSI). With the help of computer-aided design (CAD), tens of millions of devices can be integrated on a single semiconductor chip. Whatever the technology is, one must use thin-film interconnect lines to link all these devices or components in a certain way to form a functioning VLSI circuit as designed. Since the early 1970's, the density of integrated circuits has grown exponentially. Such a trend dramatically

increased device speed, decreased fabrication cost per unit of operation, and led to much smaller and more complex device structures. For the purpose of realizing proper interconnections, metal lines may take up as much as two-thirds of the chip area. A large circuit packing density with a greater design flexibility can be achieved by utilizing a metallization system with multiple levels [1], [2]. In recent years, multilevel metallization is becoming increasingly popular to minimize on-chip resistance-capacitance (RC) time delays and to optimize interconnect line layout. This results in a significant impact on device performance. The CMOS 100-MHz microprocessor developed by Intel in 1991 [3] is a good example. It was architecturally identical to the Intel-486 central processing unit (CPU), while the higher operating frequency was obtained mainly due to its more aggressive design and successful realization of an efficient triple-level metallization scheme. With the continued quest for higher degrees of complexity in VLSI metallization, more technological problems are critically involved. These require a better understanding of electrical, metallurgical and chemical properties of thin conducting as well as insulating films, refined deposition processing techniques, and stringent reliability considerations. In other words, the trend of device miniaturization has effectively moved metallization issues from a peripheral position to one of the central concerns [4].

Figure 1.1 shows schematically a cross-sectional view of a VLSI metallization structure. A number of representative features of the multilevel metallization system are illustrated in the diagram. This structure consists of three metal layers (M1, M2, and M3) with interlevel and passivation dielectrics (ILD and PD) in between and on

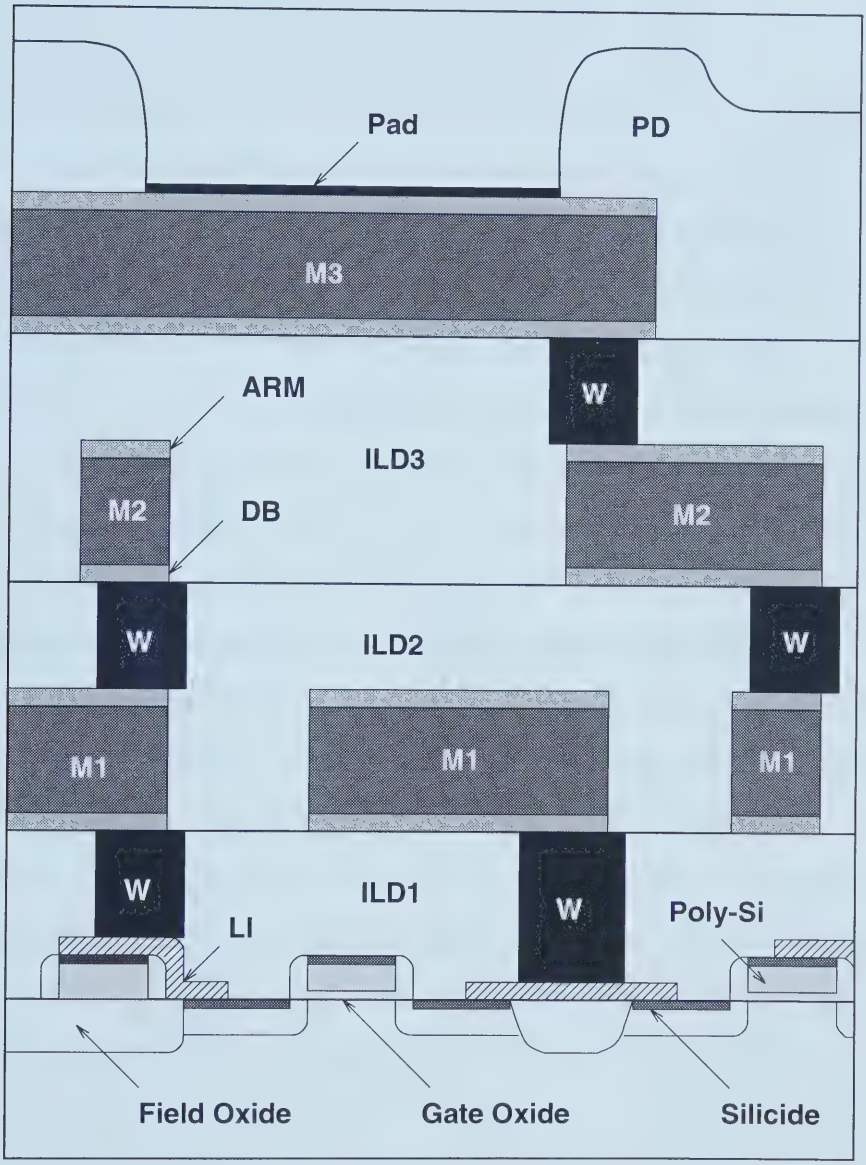

Figure 1.1 Schematic representation of a mutilevel VLSI metallization structure.

the top, respectively. A planarization process is applied to each dielectric layer to improve lithography and metal step coverage. The use of a silicide in the active semiconductor regions can reduce the contact resistance. Local interconnects (LI's) may be formed along with the silicide process to reduce parasitic effects. Contacts (usually with a relatively large depth-to-diameter aspect ratio) and vias for connecting different metal levels are opened in the dielectric films and filled with tungsten (W) plugs [5]. W is one of the refractory metal elements that has received extensive attention for its low mechanical stress and high resistance to electromigration (The current-induced displacement of metal atoms at an elevated temperature is referred to as electromigration, which has been identified as a significant source of interconnect failure in integrated circuits [6]). The metal lines consist of a stack of films. Aluminum (Al) and Al-based alloys [7], [8] have been most widely employed as the primary conductor for carrying electrical current, although copper (Cu) metallization [9] with its lower electrical resistivity and higher electromigration reliability is now being considered as a possible alternative to replace Al. In Figure 1.1, an anti-reflective material (ARM) is used on the top of Al to prevent the distortion of ultraviolet (UV) light mask image during resist exposure. With the shrinkage of device geometries, the problem of close proximity of different material components becomes more conspicuous. Unwanted interdiffusion and reactions between different materials are of concern, especially in the presence of structural defects. Diffusion barriers (DB's) [10]-[12] are thereby necessary for isolating adjacent materials which tend to react. Titanium nitride (TiN) [13] is a widely used barrier material because of its barrier efficiency and processing simplicity.

There are several methods for depositing metallization layers. Evaporation [14] is the simplest technique. It involves a vacuum system in which the metallic vapor from a heated source is condensed on a substrate. Sputtering [15] is currently the dominant process. It is a better-controlled physical process involving high-energy ion bombardment of the source. The evaporated or sputtered atoms follow line-of-sight trajectories. As a result, shadowing effects may lead to a poor metal coverage and the growth of microcracks over topographical substrate features with vertical walls. Chemical vapor deposition (CVD) [15], [16] is becoming important for growing both dielectric materials and metal layers due to its potential for uniform or "conformal" coating of non-planar substrates. In this technique, the deposition species is introduced into a chamber in the form of gaseous compounds. A chemical reaction is initiated by heat or a plasma on or near the substrate surface, creating the desired film as the reaction product. Typically, deposited metal films by these different processing techniques are all polycrystalline and characterized by columnar microstructures [17]. There is a growing influence of the film metallurgical inhomogeneities on device behavior with the downward scaling of dimensions.

From the above discussion, we have seen many advantages inherent in the miniaturization trend of VLSI devices. On the other hand, there are also many potential problems and reliability implications in device design, manufacturing and usage. Apparently, making efficient and reliable interconnections in VLSI devices requires advanced knowledge and practice of multiple disciplines, and the study of device reliability can often instigate novel technological developments [18]. In this thesis, thermal and particle diffusion phenomena in VLSI interconnect structures as

fundamental and important metallization issues will be highlighted and investigated in some detail through modeling and simulation approaches.

1.2 Diffusion Phenomena in Metallization Structures

1.2.1 Thermal diffusion

Table I lists the feature size, current density and Joule heating of metal lines for FET's and bipolar devices during different periods of technological development [19]. Over the last two decades, the minimum features that can be manufactured on a chip have been found to decrease by a factor of 2 in each five years. Comparing the values for the 1970's with those for the early 1990's, as much as fifteen and two hundred times increase in the corresponding current density (J) are found for FET's and bipolar devices, respectively. The Joule heating ($J^2\rho$, where ρ is electrical resistivity of the metal film) has increased by fifteen times for FET's and by twenty times for bipolar devices.

TABLE 1.1 Trends in Some Device Parameters

Period	Line Width (μm)	Current Density (10^5A/cm^2) FET	Bipolar	Joule Heating * FET	Bipolar
1970's	3-6	0.2-0.5	0.5-1	1	4
Mid 1980's	1.5-3	0.5	1	2-4	4-15
Early 1990's	0.5-1.5	1-2	8-15	15	~ 200

* The figures given for Joule heating are normalized with respect to the value of FET's in the 1970's.

Further device shrinkage will scale the minimum feature size of interconnect lines down to the deep sub-half-micron range in the coming century [20]. Technologies in memories, for example, are proceeding in minimum feature sizes from 0.25 μm of the state-of-the-art 256-Mbit dynamic random-access memory (DRAMs) [21] to 0.18 μm of a future 1-Gbit DRAM. The interconnect width and spacing are normally about twice the minimum feature size in the circuit. This means that a minimum metal pitch of 0.35-0.4 μm will be required. The increased current density and Joule heating carried by the thin-film metallization could be severe driving forces for many different failure mechanisms such as electromigration [6] at a large time scale and instantaneous electrical overstress (EOS). As most degradation processes occurring in microelectronic devices are strongly temperature-dependent, a higher temperature in thin-film conductors will unquestionably endanger device reliability; hence, careful thermal study and design are crucial for the development of VLSI devices.

1.2.2 Particle diffusion

In addition to the thermal diffusion effects, an improved understanding of impurity particle diffusion in polycrystalline thin-film materials is also very important because its impact on many aspects of microelectronic technology has been found to be detrimental. Although a number of different processes are involved in metal-metal and metal-semiconductor interfaces widespread in a solid state device, most of the effects can be interpreted in terms of grain boundary and interfacial diffusion in thin-film materials. This is mainly due to the facts that thin metallic films used in practical VLSI devices are polycrystalline materials and that diffusion along grain boundaries

is orders of magnitude more rapid than bulk lattice diffusion [22]. As one of the primary metallization failure mechanisms, electromigration in thin films has almost universally been attributed to grain-boundary transport processes [6]. During electromigration, voids or hillocks are formed along grain boundaries where discontinuities in atomic flux occur (*e.g.*, at grain-boundary triple points), which could induce metallization open circuits and short circuits, respectively.

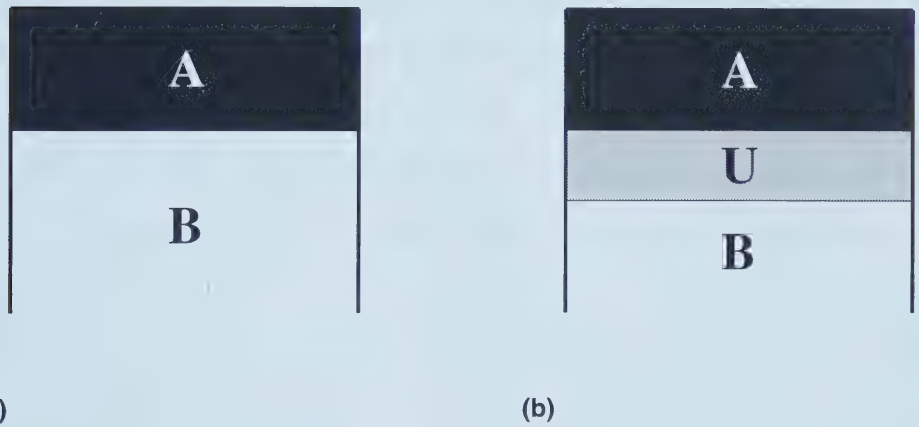

Figure 1.2 An intermediate diffusion-barrier layer U, imposed between two materials A and B. The addition of this barrier layer makes Structure (b) much more chemically stable and thus reliable than Structure (a).

Another degradation phenomenon associated with grain-boundary diffusion is failure of diffusion barriers. Figure 1.2 shows schematically a diffusion-barrier layer, U, inserted between materials A and B to prevent their direct contact and reduce the rate of interactions between A and B. A perfect diffusion barrier is intrinsically impossible due to the abundance of diffusion paths through the barrier and the

existence of large concentration gradients in such a sandwiched thin-film structure. During the fabrication and subsequent use of a device, there will be some intermixing or interdiffusion of materials A and B at the A-U and U-B interfaces. This problem is further complicated by the surface topography over which the metallization is formed and by the metallurgical inhomogeneity of the deposited barrier films. It is desirable that more quantitative information can be gained through simulations, *e.g.*, to evaluate the "effectiveness" of diffusion barriers at a microstructural level and to optimize the deposition process accordingly. Al-spike formation in a Si substrate [23] is a real example of diffusion-barrier failures, where material A in Figure 1.2 may represent the commonly-used Al metallization, and B the Si substrate. Since the grains of the polycrystalline barrier metal tend to be oriented perpendicular to the Si substrate surface, the atoms of the Al contact overlayer may diffuse through the grain boundaries of the diffusion barrier. After a certain period of elapsed diffusion time, a shallow junction may be shorted at a particular position corresponding to a higher diffusivity path in the barrier layer and the device rendered inoperable. This effect could be worsened furthermore in the presence of a current flow ("vertical" electromigration) in the same direction as the Al atomic diffusion. Evidently, the study of grain-boundary diffusion and electromigration as well as the evaluation of diffusion-barrier effectiveness are issues of practical engineering importance.

1.3 Diffusion Modeling and Simulation

Besides the economic benefits in terms of both cost and time, device performance and reliability in a specific aspect may also be investigated by modeling and simulation at

a more fundamental level, difficult to reach through experiments. The governing mathematical expressions are in general given as partial differential equations (PDE's) with a set of appropriate initial and boundary conditions. It is usually not possible to obtain tractable analytical solutions to these equations for a realistic structure in multiple dimensions. Conventional numerical methods, such as finite difference (FD) [24] or finite element (FE) [25] techniques, are utilized most frequently. In this thesis, a relatively new and powerful alternative approach, the transmission-line matrix (TLM) method [26], will be used for modeling thermal and particle diffusion phenomena in VLSI metallization structures.

In a traditional numerical technique, the problem in dealing with a function dictated by a PDE and distributed continuously in a region of interest is changed in such a way as to find the function value approximated at discrete points over the same region. The mathematical basis of the FD method is to replace the derivatives in the PDE directly by difference quotients, while the discretization process of the FE method is based on the functional principles and value interpolation in sub-divided elemental domains.

There are two important concepts in the time-dependent numerical analysis: one is the *explicit* or *implicit* nature, and the other is the numerical *stability*. Explicit methods evaluate the function $f(x,t)$ at time $t + \Delta t$ solely upon the basis of the solution obtained at time t. The solution for each time step is therefore very fast. Implicit methods determine the solution at time $t + \Delta t$ based upon the values of $f(x,t)$ at both time t and time $t + \Delta t$. Thus, a boundary value problem with all its associated simultaneous global equations in space must be solved at each time step. This

involves more programming work and computer run time. Stability of a numerical method is dependent on the time and spatial quantization. A numerical routine becomes unstable if the solution oscillates and does not converge to the final "real" answer, which often occurs in an explicit method when the time step is too long for a given spatial quantization size to satisfy the stability requirement.

Common numerical techniques tend to be either explicit but not unconditionally stable, or stable but implicit. In contrast, there are two most remarkable features of the TLM method for simulating diffusion processes. First, it is explicit. This means that only the variables local to a calculation point are involved. Therefore, it is easy to implement nonlinear effects without the need to manipulate a matrix as in the implicit FD method. Any variations of material properties may be updated at each time-stepping iteration [27]-[29]. This is of course more straightforward than FE simulators. Secondly, the TLM method is unconditionally stable. Owing to this nature, the time step can be changed without loss of stability [30]-[32]. This is especially useful for transient simulations with a time-varying diffusion source, where the versatility of choosing a proper time step could make the computation much more efficient in comparison with FD or FE techniques.

In addition, it should be appreciated that the philosophy of the TLM method [33] is quite different from the conventional one which is based on the discretization of a continuous differential equation. The TLM method is a *modeling* approach by utilizing electrical network analogies. Its intrinsically discrete algorithms are based on an understanding of the physical processes, rather than abstract mathematical concepts. Consequently, a TLM simulator program is more "user-friendly",

particularly for electrical engineers. Although it is comparatively more complex than an explicit FD simulator (note that the computer run time of such a simulator is often unbearable for a realistic problem due to the time step constrained by the numerical stability), to write an FE diffusion simulator with similar capabilities would be much more difficult. So, the simplicity is a further advantage of the TLM method compared with other numerical techniques.

The main purpose of this research is threefold. First, to investigate the dependence of the thermal response on some of the most relevant physical and geometrical parameters in interconnections. Second, to analyze atomic diffusion and electromigration through grain boundaries as well as bulk lattices in metallization materials and subsequently evaluate the effectiveness of thin-film diffusion barriers at a microstructural level. Third, to demonstrate the utility and development of the TLM method in dealing with both transient and steady-state analyses for heat and particle diffusion processes in VLSI metallization structures.

* * *

This thesis is organized as follows. In the next chapter, TLM basics and modeling philosophy are first outlined. A description of various numerical aspects of the TLM method is then presented in Chapter 3, with emphasis on several distinctive features of the method. These two chapters are necessary to clarify why the particular method is chosen for analysis and to show some new algorithm developments which will be used in solving the specific problems in the following chapters. In Chapter 4, three-dimensional (3D) steady-state thermal simulations are performed for high-density

multilevel interconnect lines. Chapter 5 concentrates on transient thermal analysis, which is of particular importance for field-programmable gate array (FPGA) devices that use voltage-programmable links (VPL's). Chapter 6 describes grain-boundary diffusion modeling in general and introduces, for the first time, the application of the TLM method in this field. In Chapter 7, 3D simulation of combined grain and grain-boundary diffusion of impurities in thin-film diffusion barriers for VLSI device metallizations is performed. Chapter 8 further discusses the implications of grain-boundary electromigration in thin-film diffusion barriers. These analyses are extended to include microstructure effects in Chapter 9, so that the prediction and evaluation of diffusion-barrier efficiency can be performed with a more realistic microstructure generated by a film-growth simulator. The final chapter, Chapter 10, contains some concluding remarks.

Chapter 2

TLM Basics

2.1 Introduction

Transmission-line matrix (TLM) modeling is a time domain numerical technique which involves the use of electrical circuit analogs to model field or other physical phenomena. This method, pioneered by the late Professor P. B. Johns in the early 1970s [34], was based on the equivalence between Maxwell's equation and equations for voltages and currents on a matrix of transmission lines. Voltage delta impulses are injected into an electronic network and the iterative progress of the pulses is monitored in space and time, both of which are rendered discrete. The motion of the delta impulses inherent in the solution of the transmission-line network can be likened intuitively to the propagation of waves. This illustrates not only an interesting and realistic approach to modeling a variety of physical processes, but also provides a means suitable to computing implementation.

It would be appropriate, therefore, to consider the TLM method as a powerful alliance between the Huygen's principle of light propagation proposed about 300 years ago [35] and the modern digital computer. Johns himself demonstrated the linkage shortly after he invented the TLM numerical routine [36].

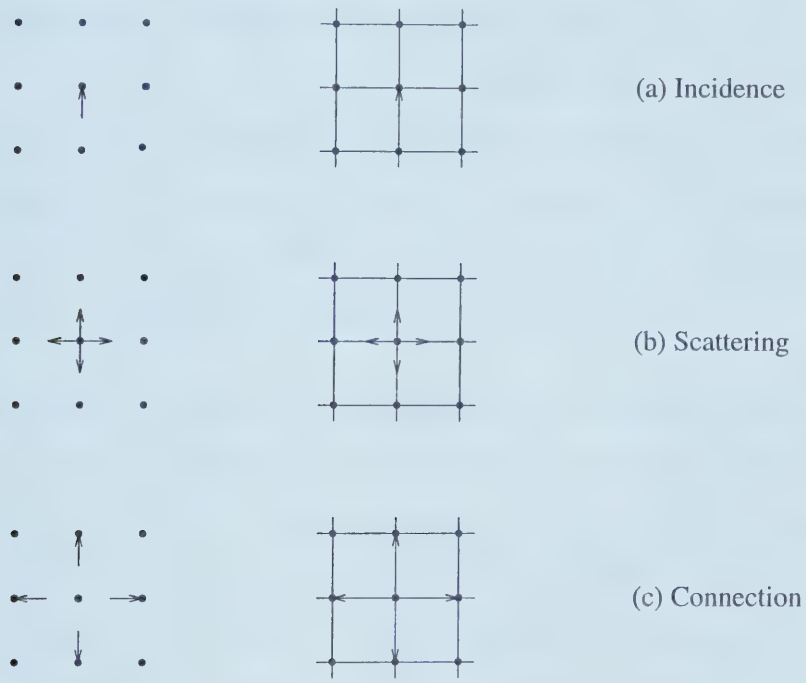

Figure 2.1 The first three steps in the propagation of an input impulse in a two-dimensional space and in the equivalent transmission-line network, shown on the left- and right-hand sides, respectively.

According to Huygens, the process of light propagation at a finite velocity was a time sequence of impulsive shocks, which may be presented in terms of the emission, transmission and reflection of light. This step-by-step process is indeed simulated by

the TLM method. Figure 2.1 shows the concept by a two-dimensional (2D) Cartesian array of nodes. Assume that a delta impulse with energy E is incident upon one of the nodes, (x, y), in the discretized isotropic space. The pulse is scattered in all four directions, each carrying one fourth of the energy, $E/4$. These pulses travel outwards and connect to the four adjacent node points within one time step. A new iteration starts immediately since they become automatically new incident impulses at $(x\text{-}1, y)$, $(x\text{+}1, y)$, $(x, y\text{-}1)$, and $(x, y\text{+}1)$. Obviously, the energy carried by each pulse when it scatters (including the reflection) at this stage is $E/16$. The time-dependent pulse scattering and connection process is repeated in the same way. The elemental distance and the time step between iterations can be easily characterized if the above 2D space is replaced by an equivalent Cartesian mesh of transmission lines.

Although the TLM method was originally developed for solving electromagnetic problems and has extensively been investigated in this field [37], [38], it is by no means restricted to wave-related issues only. The method has found many other applications with success [39], such as diffusion [26], [40], vibration and acoustics [41], as well as linear or nonlinear network problems [42]. The essential spirit of the TLM method remains the same for different applications; however, there are some specifics in each area. In this chapter, the fundamental equivalent circuit model of transmission lines will be described and methods of using it outlined. The theoretical background of TLM diffusion modeling will also be analyzed from several different viewpoints.

2.2 Equivalent Circuit Model of Transmission Lines

I start the analysis with a section of the general transmission-line circuit as shown in Figure 2.2. This is a T-type equivalent lumped network with an elemental length of Δx. The line resistance R, inductance L, conductance G, and capacitance C can be represented, respectively, by the corresponding parameters per unit length, R_d, L_d, G_d and C_d, namely,

$$R = R_d \frac{\Delta x}{2} \tag{2.1a}$$

$$L = L_d \frac{\Delta x}{2} \tag{2.1b}$$

$$G = G_d \Delta x \tag{2.1c}$$

$$C = C_d \Delta x \tag{2.1d}$$

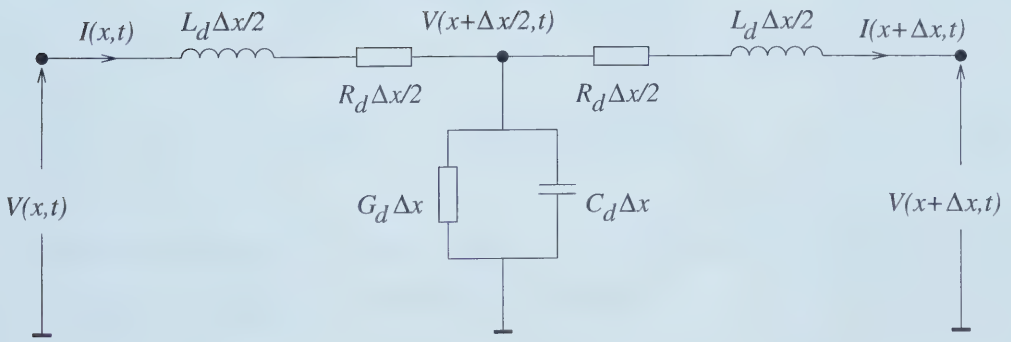

Figure 2.2 A circuit representation of a transmission-line segment of length Δx

Applying Kirchhoff's voltage law to the loop on the left-hand side of Figure 2.2 yields

$$V(x,t) = L_d \frac{\Delta x}{2} \frac{\partial I(x,t)}{\partial t} + R_d \frac{\Delta x}{2} I(x,t) + V(x+\frac{\Delta x}{2},t) \tag{2.2}$$

where V is the voltage and I is the current in the circuit. Rearranging Equation (2.2) and taking the limit as $\Delta x \rightarrow 0$, we obtain

$$-\frac{\partial V(x,t)}{\partial x} = L_d \frac{\partial I(x,t)}{\partial t} + R_d I(x,t) \tag{2.3}$$

Similarly, applying Kirchhoff's current law to the central node at the top gives

$$I(x,t) = I(x+\Delta x,t) + G_d \Delta x \, V(x+\frac{\Delta x}{2},t) + C_d \Delta x \frac{\partial V(x+\Delta x/2,t)}{\partial t} \tag{2.4}$$

or

$$-\frac{\partial I(x,t)}{\partial x} = G_d V(x,t) + C_d \frac{\partial V(x,t)}{\partial t} \tag{2.5}$$

Differentiating Equations (2.3) and (2.5) with respect to x and t, respectively, we have

$$-\frac{\partial^2 V(x,t)}{\partial x^2} = R_d \frac{\partial I(x,t)}{\partial x} + L_d \frac{\partial^2 I(x,t)}{\partial x \partial t} \tag{2.6}$$

and

$$-\frac{\partial^2 I(x,t)}{\partial x \partial t} = G_d \frac{\partial V(x,t)}{\partial t} + C_d \frac{\partial^2 V(x,t)}{\partial t^2} \tag{2.7}$$

Substituting Equations (2.5) and (2.7) into (2.6), and denoting the quantity of nodal potential by the commonly-used TLM symbol Φ gives

$$\frac{\partial^2 \Phi}{\partial x^2} = L_d C_d \frac{\partial^2 \Phi}{\partial t^2} + (R_d C_d + G_d L_d) \frac{\partial \Phi}{\partial t} + R_d G_d \Phi \tag{2.8}$$

Several important special cases can be identified if certain transmission-line parameters in Equation (2.8) are ignored. These include

a) $L_d = C_d = 0$:

$$\frac{\partial^2 \Phi}{\partial x^2} = k_1 \Phi \tag{2.9}$$

where $k_1 = R_d G_d$. Equation (2.9) is the one-dimensional (1D) elliptic PDE called the *Poisson equation.*

b) $R_d = C_d = 0$ or $G_d = L_d = 0$:

$$\frac{\partial^2 \Phi}{\partial x^2} = k_2 \frac{\partial \Phi}{\partial t} \tag{2.10}$$

where $k_2 = G_d L_d$ or $R_d C_d$. Equation (2.10) is the 1D parabolic PDE called the *diffusion equation* (the diffusion coefficient $D = 1/k_2$).

c) $R_d = G_d = 0$:

$$\frac{\partial^2 \Phi}{\partial x^2} = k_3 \frac{\partial^2 \Phi}{\partial t^2} \tag{2.11}$$

where $k_3 = L_d C_d$. Equation (2.11) is the 1D hyperbolic PDE called the *wave equation.*

Thus the 1D transmission line may be used to model problems involving elliptic, parabolic, or hyperbolic PDE's by making appropriate choice of the employed parameters. The retention, omission and/or addition of electrical components in the circuit illustrated in Figure 2.1 would make it possible to solve some other PDEs (see Section 3.8 in Chapter 3); for example, the transport continuity equation [43] which serves as one of the key equations in the analysis of various types of semiconductor devices.

2.3 Theoretical Background of TLM Diffusion Modeling

2.3.1 RC network vs TLM network

Based on the analysis in Section 2.2, an RC ladder shown in Figure 2.3 models the 1D diffusion equation and the network equations may be written as follows

$$I_n = \frac{1}{2R}[\, V_{n-1} - V_n \,] \tag{2.12}$$

and

$$I_n - I_{n+1} = C\frac{\partial V_n}{\partial t} \tag{2.13}$$

Combining Equations (2.12) and (2.13) yields a set of ordinary differential equations for the entire network

$$\frac{\partial V_n}{\partial t} = \frac{1}{2RC}[\, V_{n-1} - 2V_n + V_{n+1}] \tag{2.14}$$

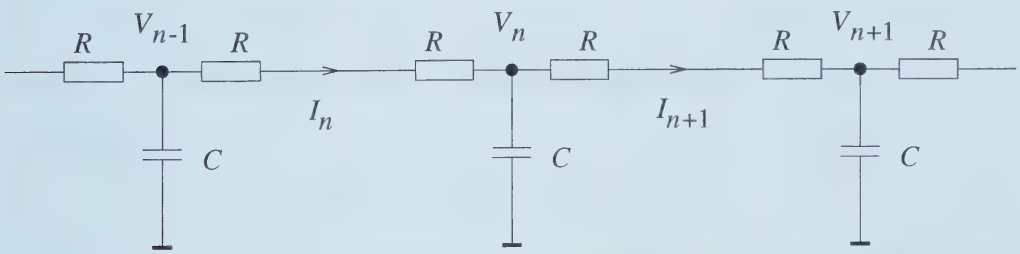

Figure 2.3 An RC network for diffusion modeling

The right-hand side of Equation (2.14) is apparently the discretization form of the second-order derivative of voltage with respect to space. Differencing of the time differential in Equation (2.14) gives

$${}_{k+1}V_n = {}_kV_n + \frac{\Delta t}{2RC}[\, {}_kV_{n-1} - 2\,{}_kV_n + {}_kV_{n+1}] \tag{2.15}$$

where ${}_kV_n$ is the voltage of node n at the kth time step. This is a simple explicit FD routine for diffusion problems. Although the spatial discretization can be understood intuitively, the temporal differencing is chosen arbitrarily. A signal appearing at a node point is observable instantly at any other points as resistor is not an energy storage device. Indeed, this routine becomes unstable and the results meaningless when $\Delta t/(2RC) > 0.5$ [44] (*i.e.*, the time step is greater than the RC time constant).

The major innovation of the TLM method over the FD one in solving the diffusion equation is the inclusion of sections of lossless transmission line within each node. Consider the case where only $G_d = 0$ in Figure 2.1, Equation (2.8) becomes

$$\frac{\partial^2 \Phi}{\partial x^2} = R_d C_d \frac{\partial \Phi}{\partial t} + L_d C_d \frac{\partial^2 \Phi}{\partial t^2} \tag{2.16}$$

This equation is normally called the *lossy wave equation*, or *telegrapher's equation*. If the second-order derivative term with respect to time on the right-hand side of Equation (2.16) is negligibly small,† then the correspondence of Equations (2.16) and (2.10) gives

$$R_d C_d = \frac{1}{D} \qquad \text{or} \qquad RC = \frac{(\Delta x)^2}{D} \tag{2.17}$$

In the TLM technique, the resistors remain clustered around each node, but the capacitance and inductance are modeled in terms of a lossless transmission line that connects the node to its neighbors and acts as a time-delay line. A 1D TLM node is shown in Figure 2.4. An iterative process is initiated by injecting voltage impulses to

---

† This assumption will be further addressed in Sections 2.3.2 and 3.7. For a more detailed discussion, see References 26, 40, 30, 31 and 45.

this transmission-line network. The TLM routine operates on the traveling, scattering, and connecting of these pulses in the network, and the local impulse population provides the solution to the problem without the necessity of a separate time discretization step. Since the transmission-line model conserves the flow quantity and contains no energy producing elements, the method must be unconditionally stable. In conjunction with the TLM routine, a technique termed "propagation analysis" has been developed by Johns [26] in 1977 in his classic paper on TLM diffusion modeling. This technique was used to formally prove the unconditional stability [26], and to establish the consistency and accuracy of the TLM method for solving the diffusion equation [40].

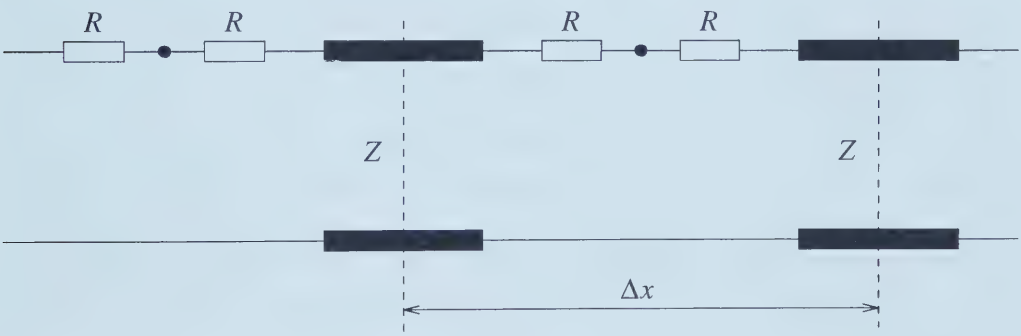

Figure 2.4 One-dimensional TLM node

According to fundamental transmission-line theory, the velocity of the impulse is given by

$$v = \frac{\Delta x}{\Delta t} = \frac{1}{\sqrt{L_d C_d}} \tag{2.18}$$

and the characteristic impedance of the lossless transmission line is

$$Z = \sqrt{\frac{L_d}{C_d}} \tag{2.19}$$

Therefore,

$$Z = \frac{\Delta t}{C_d \Delta x} = \frac{\Delta t}{C} \tag{2.20}$$

It can be seen that Equations (2.20) and (2.17) associate the simulation space and time, represented by the spatial resolution Δx and time step Δt, with the modeling parameters, resistance R and impedance Z, respectively. All other quantities in the TLM method for diffusion processes can be expressed using these four basic parameters.

2.3.2 Diffusion equation vs lossy wave equation

In the diffusion equation, there is only the first time-derivative term. The solution to the diffusion equation is, therefore, monotonic with respect to time. As we have seen, the TLM routine solves essentially the lossy wave equation [Equation (2.16)] so oscillatory behavior of the numerical solution may be obtained because of the second time-derivative term. However, the contribution of this term as a source of error for modeling the diffusion process can be reduced arbitrarily by decreasing the simulation time step and spatial resolution.†

---

† According to an early study by Taitel [46], the parabolic conventional diffusion equation and the hyperbolic lossy wave equation are, respectively, the first- and second-order differential approximations as a truncated Taylor series to a more exact random walk formulation. Therefore, the lossy wave equation is more accurate than the classical equation for describing the diffusion process provided that microscopic time step and node distance (on the order of time of free flight between collisions and mean free-path length, respectively) are employed. As this microscopically small mesh is not realistic for most practical numerical computations, the conventional diffusion equation is generally used.

It is important to appreciate that the solution of the lossy wave equation goes over into that of the diffusion equation as time progresses and that it is not unusual to consider a damped equation where the nature of the damping dominates the oscillatory effects. The detection of amplitude-modulated radio-frequency signals is a real example where the auditory sensors are totally unaware of the wave-like nature of the carrier signal. The TLM method as a means of modeling the diffusion process has proved to be extremely reliable and effective despite the approximations made in the formulation.

2.4 Basic TLM Algorithm for Diffusion

As stated above, the TLM numerical solution is found in terms of voltage impulses which propagate along the transmission lines. In the case of the node shown in Figure 2.4, propagating voltage pulses will be scattered at impedance discontinuities (the boundaries between the transmission line and resistor). The TLM algorithm is implemented by repeatedly scattering pulses at nodes and then directing the transmitted and reflected pulses to neighboring nodes to arrive after the instantaneous scattering event. Figure 2.5 [50] illustrates this process for the first several time steps. Pulses ${}_kV_L{}^i(n)$ and ${}_kV_R{}^i(n)$ are incident on node n from left- and right-hand sides at the kth time step, and the sum of these two incident voltage pulses gives the nodal potential ${}_k\Phi(n)$

$$ {}_k\Phi(n) = {}_kV_L{}^i(n) + {}_kV_R{}^i(n) \tag{2.21} $$

The first step in the next iteration is to calculate the magnitudes of the scattered pulses [${}_kV_L{}^s(n)$ and ${}_kV_R{}^s(n)$]. Conventional TLM uses an electrical network analysis, which in terms of line resistance and impedance gives

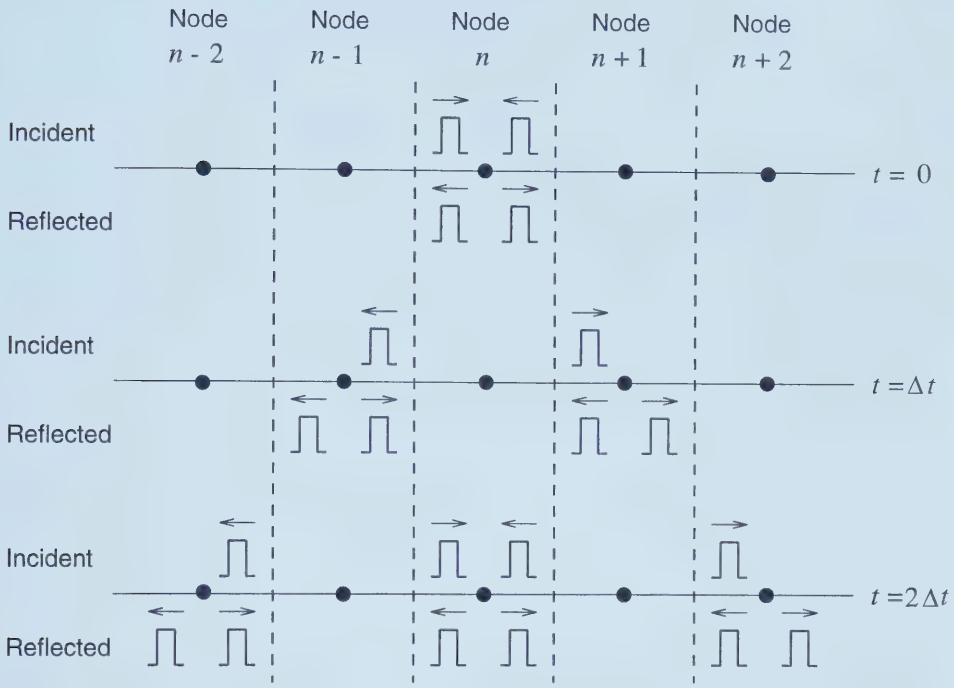

Figure 2.5 Incidence and reflection between adjacent nodes during successive time steps [47]

$$ {}_kV_L^s(n) = {}_k\Phi(n)\frac{Z}{R+Z} + {}_kV_L^i(n)\frac{R-Z}{R+Z} \tag{2.22a} $$

and

$$ {}_kV_R^s(n) = {}_k\Phi(n)\frac{Z}{R+Z} + {}_kV_R^i(n)\frac{R-Z}{R+Z} \tag{2.22b} $$

Equations (2.22a) and (2.22b) are called the *scattering algorithm*. These scattered pulses travel along a length Δx of transmission line to become incident pulses towards the adjacent nodes after a time Δt

$$_{k+1}V_L^i(n) = {}_kV_R^s(n\text{-}1) \tag{2.23a}$$

and

$$_{k+1}V_R^i(n) = {}_kV_L^s(n\text{+}1) \tag{2.23b}$$

Equations (2.23a) and (2.23b) are called the *connection algorithm*. Implementation of a TLM routine consists of repeated application of Equations (2.21)-(2.23), namely, calculation of nodal potentials, pulse scattering and connection.

Chapter 3

Numerical Aspects of TLM Diffusion Modeling

3.1 Introduction

In this chapter, several simple and representative diffusion problems are given with comparisons of the TLM solutions and the results of the analytical or FD numerical methods, demonstrating to which types of equations the TLM method can serve as an effective and heuristic tool. The examples are also used for showing some fundamental algorithms developed recently by the author of this thesis. In view of completeness, this chapter describes, comprehensively though briefly, the most important numerical treatments in dealing with practical TLM diffusion computations. These include boundary conditions, variable meshes, nonlinearities, multiple dimension considerations, time-step changes and control, and modeling drift and other effects simultaneously by using extended TLM diffusion nodes with added electronic components.

Some material in this chapter has been published as References [31], [32] and [48]-[52].

3.2 Simple Examples

It is often feasible to validate a novel numerical algorithm using a simple 1D problem where the analytical solution is available. However, the extension to a more realistic multidimensional situation would be straightforward for the TLM technique while the same extension is hardly possible with the analytical method. In some circumstances, FD or FE method may be needed to test and justify the algorithm on small problems so as to reconcile and solve larger problems subsequently. Also, a computer program written with the TLM method is often more condensed than that with traditional numerical techniques. Two representative example problems are given below in the analytical terms, followed by the comparision with the TLM results. The involved TLM treatments will be discussed in some detail together with other issues in the subsequent sections.

Example 1: Diffusion with constant source and general flux boundaries

Consider the diffusion equation

$$\frac{\partial C(x,t)}{\partial t} = D\frac{\partial^2 C(x,t)}{\partial x^2}, \quad 0 < x < l \tag{3.1}$$

along with the following initial and boundary conditions

$$C(x,0) = 0, \quad 0 \le x \le l \tag{3.2}$$

$$C(0,t) = 1, \quad t \ge 0 \tag{3.3}$$

and

$$D\frac{\partial C(l,t)}{\partial x} + \alpha C(l,t) = 0, \quad t \ge 0 \tag{3.4}$$

where C is the concentration of the diffusing species, t is the time, x is the position, D is the diffusion coefficient, and α is a parameter characterizing the out-diffusion mobility from the region of interest. Due to the inconsistency of (3.2) and (3.3), a "weak" analytical solution of this problem is given by [53]

$$C(x,t) = \frac{1 + L(1 - x/l)}{1 + L} - \sum_{n=1}^{\infty} \frac{2(\beta_n^2 + L^2)\sin(\beta_n x/l)}{\beta_n(L + L^2 + \beta_n^2)} \exp(-\beta_n^2 Dt/l^2) \qquad (3.5)$$

with $L = \alpha l/D$ and β_n satisfying the condition $\beta_n \cot \beta_n + L = 0$. When this problem is solved using a numerical approach, a surface node is attached upon the constant concentration source, but the mixed boundary node at the other end becomes active only after the diffusing species reaches there.

Example 2: Diffusion with drift

Consider the following transport equation containing both diffusion and drift terms

$$\frac{\partial \eta(\xi,\zeta)}{\partial \zeta} = \frac{\partial^2 \eta(\xi,\zeta)}{\partial \xi^2} + \gamma \frac{\partial \eta(\xi,\zeta)}{\partial \xi}, \quad 0 < \xi < 1 \qquad (3.6)$$

in conjunction with an initial uniform concentration

$$\eta(\xi,0) = 1, \quad 0 \le \xi \le 1 \qquad (3.7)$$

and the completely blocking (zero diffusion flux) boundary conditions at both sides

$$\frac{\partial \eta(0,\zeta)}{\partial \xi} + \gamma \eta(0,\zeta) = 0, \quad \zeta \ge 0 \qquad (3.8a)$$

$$\frac{\partial \eta(1,\zeta)}{\partial \xi} + \gamma \eta(1,\zeta) = 0, \quad \zeta \ge 0 \qquad (3.8b)$$

where η (= C/C_0, C_0 being the constant background concentration prior to normalization), ξ (= x/l), and ζ (= Dt/l^2) are the dimensionless concentration,

position, and time, respectively; and the parameter γ is used to characterize the strength of the drift effect. The analytical solution of this problem is given by [54]

$$\frac{C(x,t)}{C_0} = \frac{\gamma e^{-\gamma\xi}}{1 - e^{-\gamma}} + \sum_{n=1}^{\infty} \frac{16n\pi\gamma^2 [1 - (-1)^n e^{\gamma/2}]}{(\gamma^2 + 4n^2\pi^2)^2} (\sin n\pi\xi - \frac{2n\pi}{\gamma} \cos n\pi\xi)$$
$$\times \exp[-\frac{\gamma\xi}{2} - (n^2\pi^2 + \frac{\gamma^2}{4})\zeta] \qquad (3.9)$$

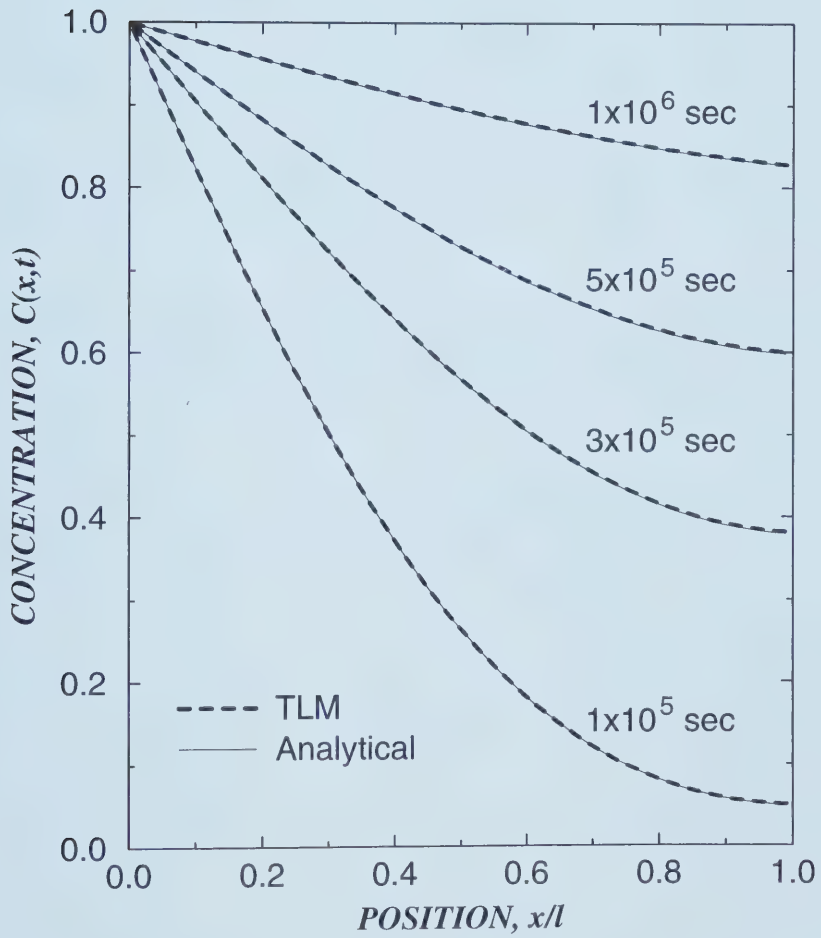

Figure 3.1 Example 1: comparison of the analytical and TLM solutions of the concentration vs position for several values of the elapsed diffusion time [48].

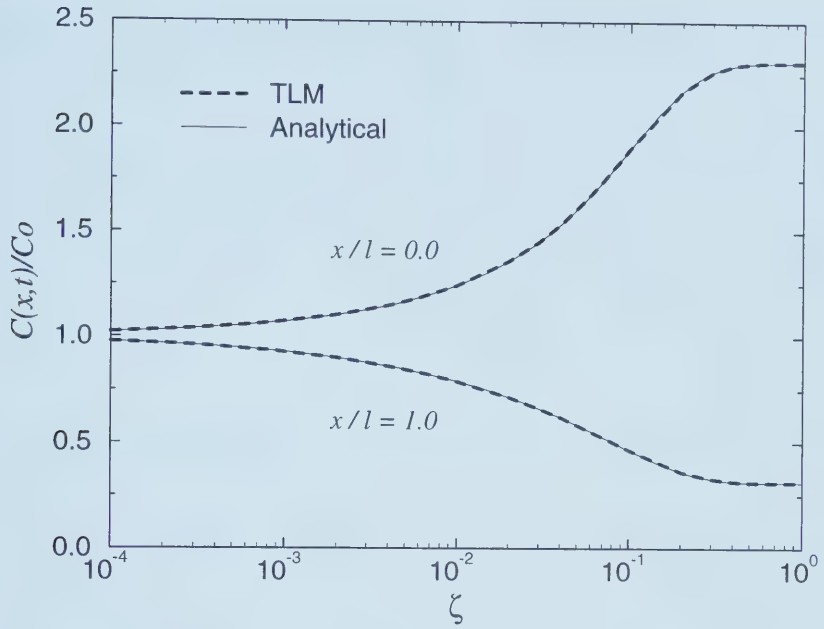

Figure 3.2 Example 2: comparison of the analytical and TLM solutions of the concentration vs diffusion time ($\gamma = 2$) [48].

I have calculated these example problems using the analytical solutions and the TLM numerical technique. In example 1, a set of values typical of grain-boundary diffusion in thin films are assumed to obtain the results: $l = 10^{-4}$ cm, $D = 10^{-14}$ cm^2/sec, and $\alpha = 10^{-11}$ cm/sec. The first fifty terms of the analytic infinite series in Equations (3.5) and (3.9) are computed to generate accurate answers. As for the TLM method, a spatial resolution of $\Delta x = 1\times10^{-6}$ cm and a time step of $\Delta t = 25$ seconds (from the FD stability criterion) are used in Example 1 and $\Delta\xi = 5\times10^{-3}$ and $\Delta\zeta = 1\times 10^{-5}$ in Example 2. The diffusion-drift equation (3.6) has been solved using the extended TLM diffusion node (see Section 3.8). The initial unity concentration is realized by launching two half-valued incident voltage pulses onto all the nodes before starting the computation. Figures 3.1 and 3.2 demonstrate the results of

Examples 1 and 2, respectively. In Figure 3.1, the concentration as a function of position is shown for several values of the elapsed diffusion time. Figure 3.2 shows the concentration variation with time until saturation at the two blocking boundaries under test. Because of the drift effect, there is a mass buildup at $x = 0$, and a mass depletion at $x = l$. Clearly, the agreements between the analytical and TLM methods are excellent, validating the TLM numerical solution.

3.3 Boundary Conditions

The treatment of boundary conditions is of paramount importance in solving a PDE either analytically or numerically. The ease of accommodation of various boundary conditions is a remarkable strength of the TLM method.

3.3.1 Boundaries defined by the voltage reflection coefficient

In general, it is convenient to place a boundary by terminating a transmission line half way apart from the node point. In TLM modeling, a delta pulse traveling along a transmission line sees only one impedance, denoted here as Z_1. Assume that a discontinuity of the transmission line occurs at the node boundary, and the impedance becomes Z_2 beyond the boundary. The voltage pulse will be reflected according to the reflection coefficient, which is defined as

$$\rho = \frac{Z_2 - Z_1}{Z_2 + Z_1} \tag{3.10}$$

Extensive use is made of this reflection coefficient for voltage pulses propagating to a boundary. Figure 3.3 [49] shows several important special cases, which are discussed next.

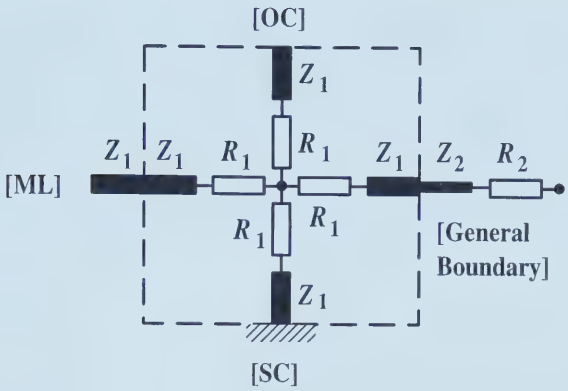

Figure 3.3 Several commonly-used TLM boundary conditions. (a) Short circuit (SC), (b) Open circuit (OC), (c) Matched-load (ML), and (d) General boundary between two adjacent nodes [49].

a) $Z_2 = 0$. This is an electrical *short circuit* (SC) boundary condition. In this case, $\rho = -1$, so that a pulse will be returned equal in magnitude but reversed in phase. This represents a *constant voltage sink* because the potential at the boundary can set to any fixed background value, which remains unchanging during the calculation (the Dirichlet condition in the continuity equation formulation).

b) $Z_2 \rightarrow \infty$. This is an electrical *open circuit* (OC) boundary condition. In this case, $\rho = 1$, so that a pulse will be returned equal in magnitude and in the same phase (also called a *reflective boundary* or *insulating boundary*). This is useful for modeling a perfect diffusion barrier or symmetrical faces where the voltage gradients are zero (the Neumann condition).

(c) $Z_2 = Z_1$. This is a *matched-load* (ML) boundary condition. In this case, $\rho = 0$, so that a pulse will keep traveling unaffected along the transmission line. In a general boundary between two adjacent nodes, this means that there is no internodal

scattering and a scattering event will take place when the pulse reaches the lumped resistor in the next node. The transmission line simply connects a node to its neighbor and acts as a time-delay line. However, if there is no further node and the space is terminated by a matched-load transmission line, the pulse will never be returned after reaching the boundary. Therefore, it is also termed as an *absorbing boundary*. In Section 3.3.3, we will show that the ML boundary is a special case of the mixed condition. This condition is useful, for instance, for describing material losses from the region of interest in a mass diffusion model.

3.3.2 Boundaries defined by voltage sources

In addition to the reflection of propagating pulses at boundaries in terms of the reflection coefficient, the source boundary can fall into another category where a *constant-voltage source boundary* is an important one [50]. The initial incident voltage pulse at the very beginning (k = 1) is assumed as half the constant voltage (V_C) at the surface (adjacent to the 1st node) in common with the FD method [55] for the same problem

$$ {}_1V_L^i(1) = \frac{V_C}{2} \tag{3.11} $$

At all the subsequent time steps ($k \geq 1$), incident voltage pulses from the surface are calculated by

$$ {}_{k+1}V_L^i(1) = V_c - {}_kV_L^s(1) \tag{3.12} $$

to ensure the voltage conservation (see Figure 3.4). Equations (3.11) and (3.12) are the formulae needed for the simulation of the surface with a constant voltage source.

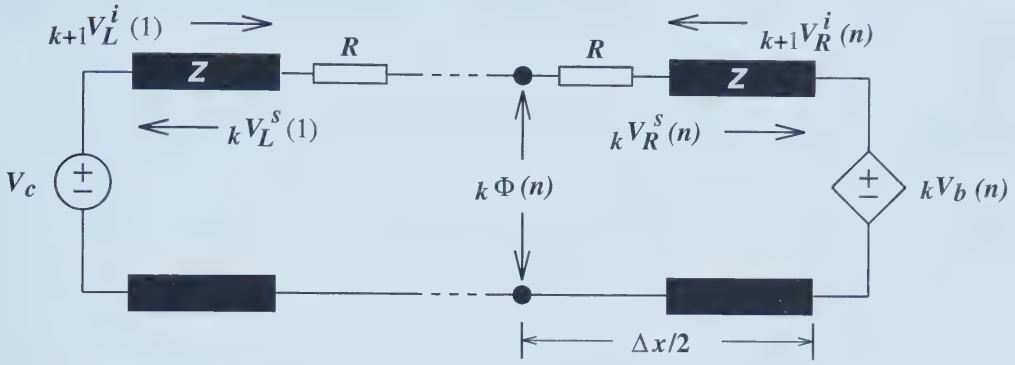

Figure 3.4 Constant and controlled voltage sources at boundaries

Now, I show that the mixed (Robin) boundary condition for a general diffusion flux, Equation (3.4), may be realized in the TLM method by introducing a controlled voltage source. The right-hand side of Figure 3.4 shows my treatment of such a boundary condition (adjacent to the nth node). Applying the Taylor series expression on the first term in Equation (3.4) with the use of the boundary concentration and the concentration at the adjacent node, one can obtain an average concentration gradient $\Delta x/4$ from the boundary. However, the value exactly at the boundary would be the same since a linearly varying concentration is assumed in that region. Consequently, the boundary condition (3.4) is approximated by a difference equation with the commonly-used TLM terminology

$$D\frac{{}_kV_b(n) - {}_k\Phi(n)}{\Delta x/2} + \alpha\, {}_kV_b(n) = 0 \tag{3.13}$$

where an analogy between voltage and concentration is employed; thus, ${}_kV_b(n)$ and ${}_k\Phi(n)$ represent, respectively, the voltage at the boundary and the potential of the node adjacent to the boundary at the kth time-step iteration, and Δx is the node length.

Equation (3.13) suggests that there is a voltage source connected to the boundary and controlled by the local current (analogous to diffusion flux). The magnitude of this voltage source varies at each time step, and is determined by rearranging Equation (3.13)

$$ {}_kV_b\,(n) = \frac{2D}{2D + \alpha\Delta x}\,{}_k\Phi(n) \tag{3.14}$$

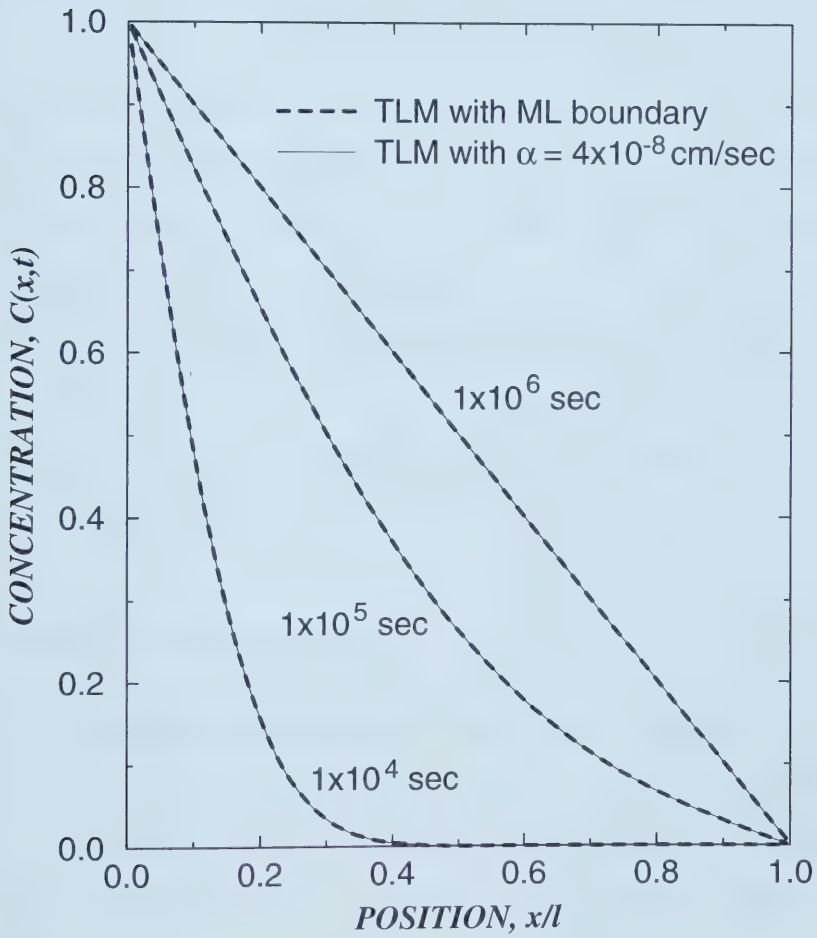

Figure 3.5 Comparison of the TLM solutions with an ML boundary and with a special α value of 4×10^{-8} cm/s in the general boundary condition (3.13) [48].

It should be remembered that incident voltage pulses establish a nodal potential. Therefore, the boundary condition must be given in terms of the voltage pulse incident towards the centre of the boundary node. Similar to Equation (3.12), the incident pulse at the succeeding time step $[{}_{k+1}V_R^i(n)]$ will be dictated by the above boundary source and by the arriving voltage pulse scattered from the boundary node at the current time step $[{}_kV_R^s(n)]$, namely,

$$ {}_{k+1}V_R^i(n) = {}_kV_b(n) - {}_kV_R^s(n) \tag{3.15} $$

It is possible to use the same expression [Equation (3.13)] to describe several other boundary conditions with special values of the α parameter: i) $\alpha \to 0$. This means a zero out-diffusion flux, equivalent to the OC boundary. ii) $\alpha \to \infty$. This requires the concentration at the boundary to approach zero, *i.e.*, $C(0,t) \to 0$, so that the diffusion flux becomes a finite value which depends solely upon the concentration gradient for a given material. This complete sink condition is equivalent to the SC boundary. iii) In the next section, I will show numerically that the ML boundary is also a special case of Equation (3.13).

3.3.3 Matched-load boundaries †

In Figure 3.5, an interesting agreement between the matched-load (ML) boundary at $x = l$ and Equation (3.13) with a particular value of α (see Section 3.2, Example 1: $\alpha = 4 \times 10^{-8}$ cm/s) is displayed. The ML boundary is defined according to $\rho = 0$, or equivalently, the incident voltage pulse from the boundary is ${}_kV_R^i(n) = 0$. This

† An explicit expression of matched-load boundaries can be found in Appendix.

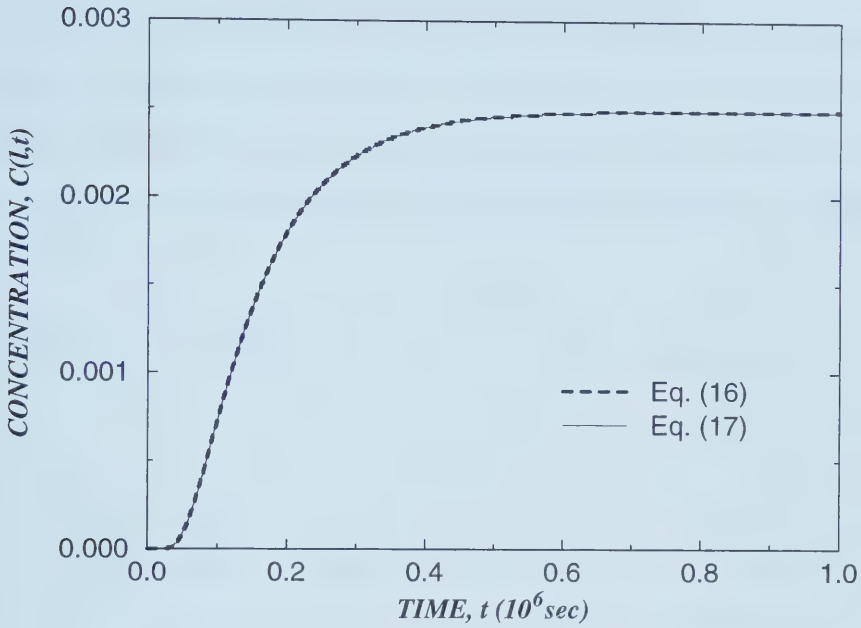

Figure 3.6 Comparison of the boundary concentration vs time as calculated by Equations (3.16) and (3.17) [48].

condition has previously been used to terminate a problem space which would extend to a larger or even infinite domain [28]. However, erroneous results will be produced if the ML boundary is not located sufficiently far away from the diffusion source region, because the natural backscatter of the diffusing species is ignored. Based on this consideration, the use of discrete Green's functions has been suggested to include the effects of the diffusion tail [56]. The present observation on the ML boundary may suggest an alternative physical interpretation — it is a special case of the out-diffusion flux from the boundary. The corresponding α value is unique for a given material system and can be known from calculation.

The equivalence of the ML boundary and a special case of the mixed condition can be further illustrated by the boundary concentration $C(l,t)$ as a function of time through calculations by the two different approaches. For $\rho = 0$, there is no incident pulse traveling from the boundary upon the adjacent node; therefore, at any time

$$ {}_kV_b(n) = {}_kV_R^s(n) \tag{3.16}$$

From Equation (3.13) combined with the specific value of α, we have

$$ {}_kV_b(n) = {}_k\Phi(n)/3 \tag{3.17}$$

A comparison between expressions (3.16) and (3.17) are shown in Figure 3.6 [48]. Again, the model results are almost indistinguishable. It is worthwhile to appreciate, by looking at Figure 3.6 along with Figure 3.5, that both methods give virtually the same results over space and time. Note that the diffusing species have not yet reached the boundary at time $t = 1\times10^4$ seconds, so boundary conditions do not come to play at that time. The concentration distributions at $t = 1\times10^5$ seconds represent a typical transient case of concentration growth. Finally, the steady state is established at $t = 1\times 10^6$ seconds, when the diffusion process is in equilibrium in accordance with the boundary condition (3.4).

3.4 Variable Meshes

For practical geometries, it is frequently more computationally-efficient and convenient to employ a simple orthogonal irregular mesh, so that a fine mesh can be used where the rate of change of potential or the voltage gradients are anticipated to be large and a coarse mesh is used when the fine mesh is unnecessary.

In the calculation of the TLM method, all voltage pulses should take one time step (Δt) to travel the transmission lines between nodes, or take $\Delta t/2$ from the nodes to the boundaries. If the spacing of the node is varied, then the velocities of pulses must be varied as well so as to force the pulses to arrive at all node points simultaneously. This is the key point for constructing a variable mesh.

There are two approaches to change node size: the use of stubs [57], [58], and the use of unmatched transmission lines [28], [29]. Now I describe the second approach as suggested in Reference 50. For constructing the network components, Equation (2.17) actually permits a totally *arbitrary* distribution of R and C, but a *better choice* would be

$$R = \frac{\Delta x}{2D} \tag{3.18a}$$

and

$$C = \Delta x \tag{3.18b}$$

for the 1D problem. This choice enables a variable mesh to be realized automatically simply by specifying each node size. According to Equation (2.20), an impulse traveling for a distance $\Delta x/2$ takes the time

$$\Delta t = ZC_d \, \Delta x/2 \tag{3.19}$$

If a node has the dimension $\Delta x' = \lambda \Delta x$ (see Figure 3.7, where λ is the node stretch factor), then the following impedance transformation

$$Z' = Z/\lambda \tag{3.20}$$

must be performed with the node to guarantee the *synchronization*, *i.e.*

$$\Delta t' = Z'C_d \, \Delta x'/2 = \Delta t \tag{3.21}$$

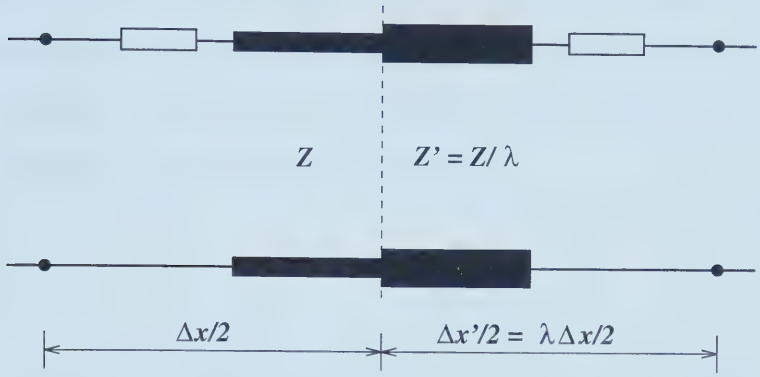

Figure 3.7 Construction of a variable mesh through the impedance transformation

It can be found that exactly the same stretch factor has been used in changing node size and the corresponding impedance. This coherent way of creating a variable mesh is more convenient to implement than the stub transmission-line approach. Of course, the reflection and transmission at inter-nodal impedance discontinuities must be considered when calculating the pulse propagation.

Figure 3.8 illustrates a general layout of the variable mesh for a TLM thermal simulator. Nodes at different positions may represent the same or different materials. Heat sources could be situated at the surface or embedded within the structure, depending on specific problems of interest. It is often possible to consider only a portion of the entire region because of the symmetry in geometry. In such cases, the OC boundaries are employed. A heat sink of constant temperature can be realized by the SC boundary condition. Although not implemented in this thesis yet it is possible to include discontinuous mesh lines [59]-[61], which offers further potential for

reducing the computer execution time. A text input file may be used to specify the geometry, physical parameters and program procedure, while an output array can be suitably designed for drawing 2D or 3D pictures with a post-processing graphics package to make the results immediately sensible.

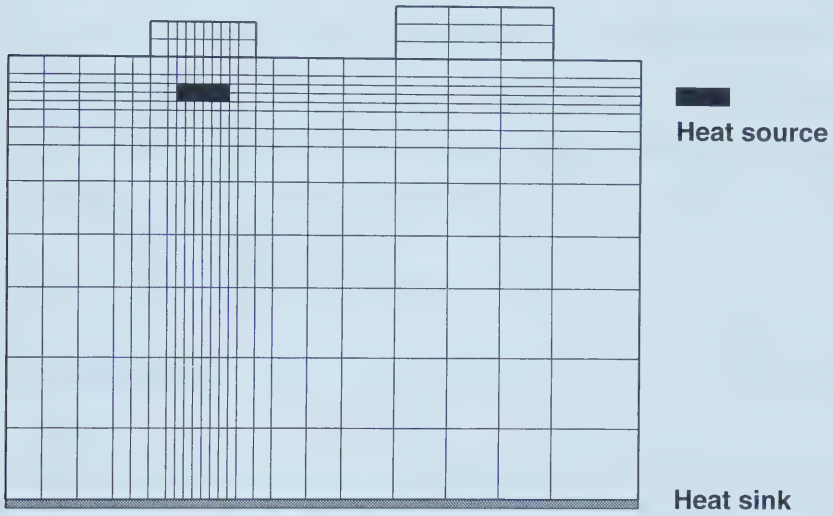

Figure 3.8 Mesh layout for a TLM thermal simulator

3.5 Nonlinearities

The explicit nature of the TLM method implies that all calculations for a particular node point involve only variables local to that position. Therefore, nonlinearities in parameters can conveniently be incorporated by using an updated value from the most recent time-step iteration to replace the old one for the current calculation. This is a

very good approximation for most practical applications. There is no need to perform a numerically intensive matrix manipulation, which characterizes an implicit technique.

Changes in parameters which are modeled by resistors (*e.g.*, thermal conductivity in thermal diffusion problems) can be accommodated simply by altering the values of resistors before calculating the new incident pulses. However, changes in parameters modeled by capacitance necessitate an impedance transformation due to Equation (2.20) and the requirement of synchronization. Again, the discontinuous and stub-loaded transmission-line methods can be used and these two methods are equivalent in dealing with the nonlinear properties [27].

3.6 Multiple Dimensions

For a realistic simulation, 2D or 3D analysis is usually required. The TLM method is advantageous in this respect as it is straightforward to extend the 1D treatment to n dimensions (n = 1, 2, or 3), and it is convenient to construct a corresponding transmission-line network for solving the lossy wave equation

$$\nabla^2\Phi = n\,L_d\,C_d\,\frac{\partial^2\Phi}{\partial t^2} + 2\,n\,R_d\,C_d\,\frac{\partial\Phi}{\partial t} \tag{3.22}$$

or the equivalent linear or nonlinear diffusion equation

$$\nabla\cdot(D\,\nabla\Phi) = \frac{\partial\Phi}{\partial t} \tag{3.23}$$

Details of single 2D and 3D TLM diffusion nodes are shown in Figures 3.9(a) and 3.9(b), respectively. One pair of resistors surrounds the node in each orthogonal

direction. R_x, R_y and R_z are resistances in the x, y, and z directions respectively, and Z is the characteristic impedance of the transmission line within the node. The link transmission lines in $2n$ branches connect a node to its neighboring scattering zones. The capacitance appropriate to the element is now shared by n complete transmission lines; thus Equation (2.20) becomes

$$Z = \frac{\Delta t}{C/n} \tag{3.24}$$

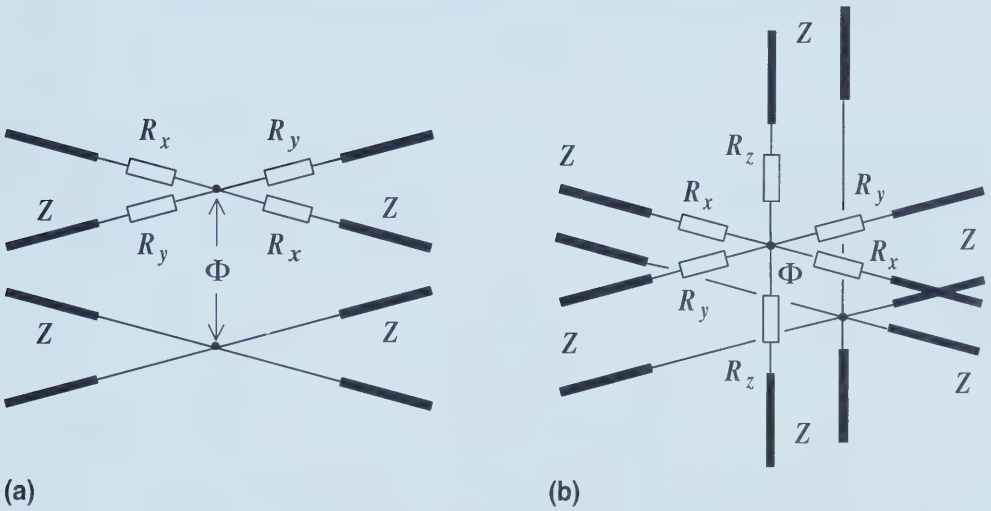

Figure 3.9 Single 2D **(a)** and 3D **(b)** TLM nodes. The values of R_x, R_y, R_z and Z may be different from node to node in a variable mesh or inhomogenous materials.

A numbering convention is shown in Figure 3.10 to denote the directions of the voltage pulse or alternatively the branches of the node in the Cartesian coordinate system. Let ${}_kV^i_j$ be the voltage pulse incident on a node from direction j at the kth iteration, the nodal potential due to the incident pulses from all the directions can be found by applying the Thevenin and Norton theorems of circuit analysis to the node.

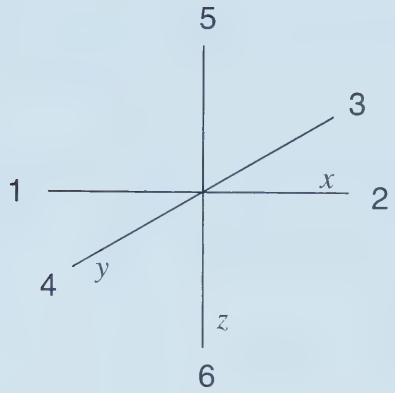

Figure 3.10 A 3D Cartesian coordinate with the numbers denoting the six orthogonal directions.

If the node is symmetrical ($R_x = R_y = R_z$), its potential can be given by the simple average magnitude of the incident pulses

$$ {}_k\Phi = \frac{1}{n} \sum_{j=1}^{2n} {}_kV_j^i \tag{3.25} $$

In a general 3D situation, the nodal potential is given by [29]

$$ {}_k\Phi = \left[\frac{2\left({}_kV_1^i + {}_kV_2^i\right)}{R_x + Z} + \frac{2\left({}_kV_3^i + {}_kV_4^i\right)}{R_y + Z} + \frac{2\left({}_kV_5^i + {}_kV_6^i\right)}{R_z + Z} \right] \frac{1}{Y} \tag{3.26} $$

where

$$ Y = \frac{2}{R_x + Z} + \frac{2}{R_y + Z} + \frac{2}{R_z + Z} \tag{3.27} $$

Similar to Equation (2.23), the scattered pulses at a node can be calculated from

$$ {}_kV_{1,2}^s = \frac{1}{R_x + Z}\left[Z\ {}_k\Phi + (R_x - Z)\ {}_kV_{1,2}^i \right] \tag{3.28a} $$

$$ {}_kV_{3,4}^s = \frac{1}{R_y + Z}\left[Z\ {}_k\Phi + (R_y - Z)\ {}_kV_{3,4}^i \right] \tag{3.28b} $$

$$ {}_kV^s_{5,6} = \frac{1}{R_z + Z}\left[Z\ {}_k\Phi + (R_z - Z)\ {}_kV^i_{5,6}\right] \tag{3.28c} $$

TABLE 3.1 The Values of j, j', u, v, and w Used for Equations (3.29) and (3.30)

j	j'	u	v	w
1	2	x - 1	y	z
2	1	x + 1	y	z
3	4	x	y - 1	z
4	3	x	y + 1	z
5	6	x	y	z - 1
6	5	x	y	z + 1

As indicated in the last section, the value of Z in adjacent nodes may be different for a variable mesh. The incident pulse from a node boundary with an impedance discontinuity at the next time step is then composed of two scattered pulses at the current time step: that reflected from the same node and that transmitted from the adjacent node. Taking into account these internodal pulse-scattering events, the equation (2.24) for the incident pulses are modified as

$$ {}_{k+1}V^i_j(x, y, z) = \rho_j(x, y, z)\ {}_kV^s_j(x, y, z) + \tau_{j'}(u, v, w)\ {}_kV^s_{j'}(u, v, w) \tag{3.29} $$

where the voltage reflection coefficient in direction j is given by

$$ \rho_j(x, y, z) = \frac{Z(u,v,w) - Z(x,y,z)}{Z(u,v,w) + Z(x,y,z)} \tag{3.30a} $$

and the voltage transmission coefficient in the opposite j' direction can be calculated according to

$$\tau_{j'}(u, v, w) = 1 + \rho_{j'}(u, v, w) = 1 - \rho_j(x, y, z) \tag{3.30b}$$

The corresponding values of j', u, v, w for $j = 1, 2, ..., 6$ in Equations (3.29) and (3.30) are listed in Table 3.1. A 3D diffusion equation can be solved by repeated applications of Equations (3.26)-(3.30) along with the initial and boundary conditions defined by a particular problem.

3.7 Time Step Changes and Control

The TLM method is an unconditionally stable method. This means that the time step can be increased without loss of stability and the size of the time-step increase is restrained only by the accuracy with which calculated results are required. As a limiting case, the maximum time step which can be used initially in TLM diffusion modeling has been found to be the same as that determined by the stability criterion for an explicit FD scheme [51]. It is important to note that possible oscillations resulting from the second-order time-derivative term in Equation (3.22) are quickly damped out with elapsed time. Consequently, there is no danger of overshooting or undershooting behavior if the time step is increased gradually during the simulation. This brings about a very substantial gain in computational efficiency while retaining a reasonable accuracy, which is one of the principal advantages of the TLM method.

The time step changing process involves simply changing the inter-nodal reflection and transmission coefficients (see Figure 3.11). As pulses reach the boundary of two neighboring nodes with the impedances of Z_j and Z_{j+1} respectively, the transformed reflection coefficient (ρ') and transmission coefficient (τ') become [32]

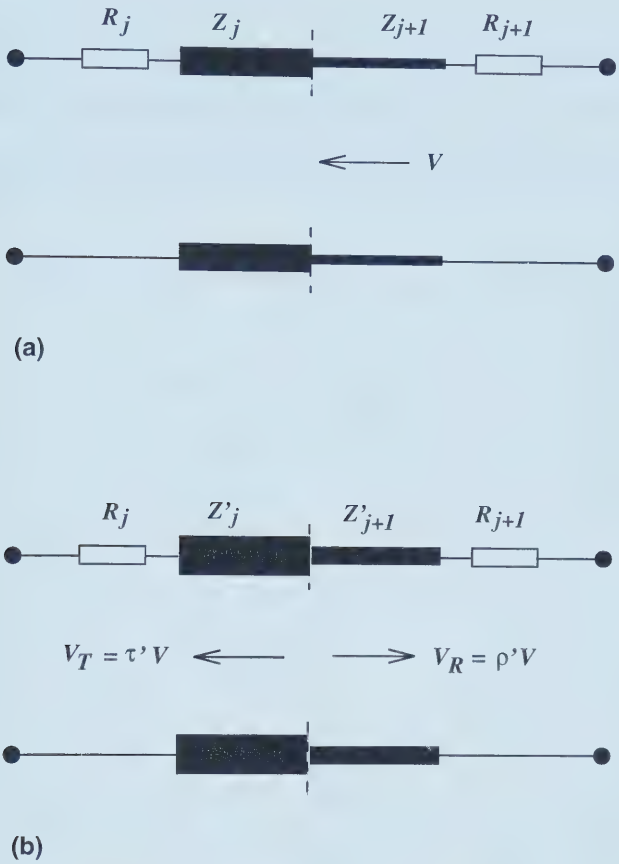

Figure 3.11 Change of impedance and time step when a voltage pulse V reaches the boundary of two adjacent nodes. V_T and V_R represent, respectively, the transmitted and reflected pulses [50]

$$\rho' = \frac{Z_j - \beta Z_{j+1}}{Z_j + Z_{j+1}} \tag{3.31a}$$

and

$$\tau' = \frac{(1+\beta) Z_j}{Z_j + Z_{j+1}} \tag{3.31b}$$

where β is the ratio of the new and old time steps ($\beta = \Delta t'/\Delta t$), and is also the ratio of the new and old impedances (Z'/Z) owing to Equation (3.20). If there is no

transformation ($\beta = 1$), Equations (3.31a) and (3.31b) will be reduced to the standard formulae. By virtue of this time-step change feature, the TLM method could be orders of magnitude faster than explicit FD routines for a long transient simulation.

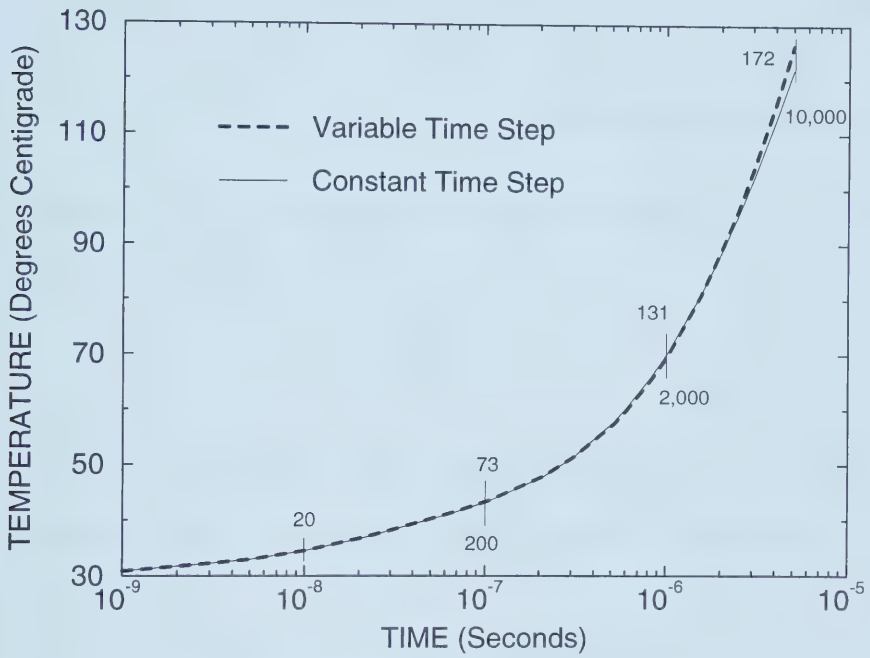

Figure 3.12 Transients for constant and variable time steps [32]

Figure 3.12 illustrates a simulation example of the maximum temperature within a power semiconductor device [32]. The solid line in Figure 3.12 represents an accurate simulation within the constraints of the mesh size employed, using a constant time step in the same order as that required by an FD scheme. The dashed line was obtained using a variable time step, which remained constant during the first 20 iterations, and was then increased by 4% at each iteration after a time equal to 10^{-8} seconds. Figure 3.12 shows the transient temperature up to 5×10^{-6} seconds. Notice

that the number of iterations for the constant time step is as large as 10,000, while for the variable time step it is only 172.

In this demonstration, the time step eventually becomes too long to accurately solve the diffusion equation. Normally, it would be automatically controlled by monitoring an error parameter to keep the solution accuracy within reasonable tolerances. Three different parameters have been proposed for this purpose:

- The ratio between the second- and the first-order derivative terms with respect to time in the lossy-wave equation (3.22) [30], [31]

$$m = (L_d C_d \frac{\partial^2 \Phi}{\partial t^2}) / (2 R_d C_d \frac{\partial \Phi}{\partial t}) \tag{3.32}$$

- Making the second time-derivative term absolutely small by controlling the consecutive potential changes ($\Delta\Phi_1$ and $\Delta\Phi_2$) and the corresponding time steps (Δt_1 and Δt_2) [62]

$$\varepsilon = L_d C_d \frac{\Delta\Phi_1/\Delta t_1 - \Delta\Phi_2/\Delta t_2}{(\Delta t_1 + \Delta t_2)/2} \tag{3.33}$$

- Taking into account all the three terms in equation (3.22) [45]

$$\Lambda = \frac{\nabla^2\Phi - 2 R_d C_d \partial\Phi/\partial t}{L_d C_d \partial^2\Phi/\partial t^2} \tag{3.34}$$

Although the last parameter appears to be more rigorous theoretically due to the inclusion of the spatial derivative term, it is difficult to implement in a practical computer program for the same reason. A pre-determined value of the m or ε

parameter on the order of 10^{-3} to 10^{-2} is currently being used during the calculation to ensure the time step changes in a way consistent with solving the diffusion equation within well-defined limits.

3.8 Extended TLM Diffusion Node

It is well known that the continuity transport equation is one of the most important relations which have been the backbone of many electronic and photonic device models. The equation has the following form [63]

$$\frac{\partial n}{\partial t} = D\,\nabla^2 n + \mu \mathcal{E}\,\nabla n - \frac{n}{\tau} + g \tag{3.35}$$

where n is the electron concentration, D is the diffusivity, μ is the mobility, τ is the lifetime, g is the generation rate, and $\mathcal{E}$ is the electric field. The circuit representation

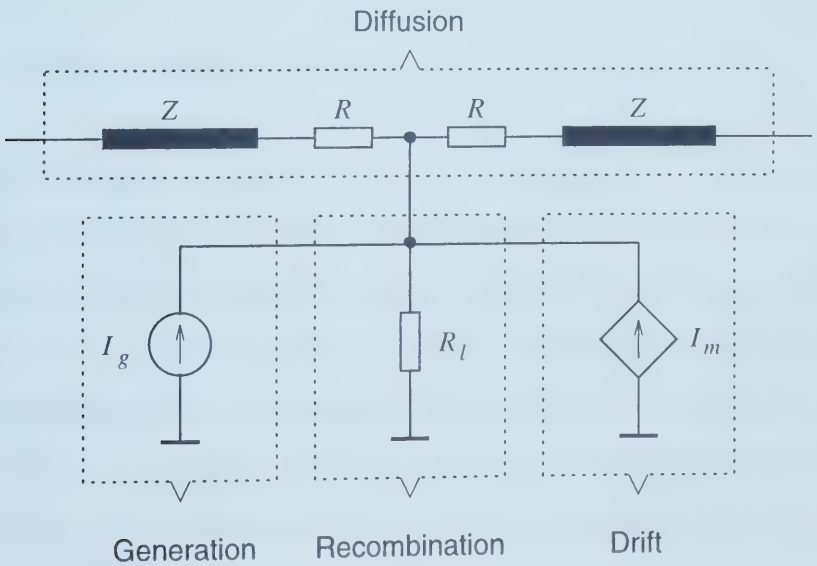

Figure 3.13 An extended TLM diffusion node for modeling the continuity equation.

associated with a 1D single node is shown in Figure 3.13. Besides the lumped resistors R and the lossless transmission lines with a characteristic impedance Z within the framework of the general TLM diffusion modeling, a constant current generator I_g, a voltage-controlled current generator I_m, and a leakage resistor R_l are added to model the generation, drift, and recombination effects, respectively [43], [52]. The magnitudes of these circuit components may be chosen to be different from one node to another to represent possible spatial variations.

The inclusion of the drift term was originally developed in the absence of any physical boundaries and calculated from the average potential difference at adjacent nodes [43]. This can be modified to calculating the average potential difference across the same node. Accordingly, terminations of a problem space, *e.g.*, by a general diffusion-flux boundary condition, can be treated with ease [48].

3.9 Dynamic matrix expansion

There is a significant difference between the situations of electromagnetic and diffusion problems when the TLM method is applied. In the former case, the impulses are quickly scattered through the complete space under consideration, and a solution for all nodes is generally required. In the latter case, however, there is frequently a small localized diffusion source surrounded by a large volume of material (*e.g.*, heat-flow problems of microwave semiconductor power devices [29], [64]). As a result, the majority of the nodes may have zero potential values for a remarkable period of computational time.

The TLM simulation of diffusion problems can be accelerated by computing only the "active" nodes [29], [65]. The number of these nodes can be expanded dynamically ahead of the diffusion flux, until filling the entire mesh designed. Calculations are then continued using the appropriate "real" physical boundaries. This technique is especially useful for long-term transient simulations.

3.10 Concluding Comments

The TLM method is a relatively new numerical technique for modeling wave propagation and other equalization processes which are usually described by PDE's. Unlike its more traditional numerical counterparts, such as FD or FE methods, the TLM approach is rendered discrete intrinsically both in space and in time. This feature makes the TLM method much more physically realistic and enables the method to offer an insight into the phenomena being modeled.

The TLM method has been applied successfully to a number of multi-dimensional diffusion problems in Cartesian [27]-[29], [49], [50], [58], [62], [64], cylindrical [44] or spherical [66], [57] co-ordinates. Excellent agreements were found between the TLM solution and analytical or other numerical results in the regimes where they can be applied. Variable TLM orthogonal meshes have also been employed for modeling bodies of complex geometry. Furthermore, the concept of controlling the time step allows this unconditionally-stable modeling technique to be very computationally efficient. The TLM method should have considerable potential in practical applications as well as in theoretical analyses for a variety of diffusion problems.

Chapter 4

Thermal Diffusion: Steady-State Analysis

4.1 Introduction

With the continuing miniaturization of microelectronic devices, the feature sizes of VLSI circuits are being rapidly reduced into the deep sub-micron range. In order to decrease propagation delays due to parasitic capacitances from interconnects and maximize chip area utilization, high density multilevel metallization systems are required [1], [2]. While promising significant improvements in device performance, this trend increases the current density and associated Joule heating, which could accelerate many degradation processes in fine metal lines, such as mass transport induced by electromigration [6], [19] and thermal stress voiding [68]. As direct measurements at these dimensions are very difficult to perform accurately, computer simulation plays a significant role for the development of highly reliable VLSI devices.

The material in this chapter has been published as Reference [67].

There have been a number of thermal studies in this respect, and most of the investigations have focused attention on vias connecting two metallization levels. These include the FE solutions of the electrical potential and thermal diffusion equations in two [69]-[71] and three [72], [73] dimensions, and the incorporation of 2D microstructure simulations into the analysis of current and heat flow [74]. In addition to the via contacts, crossovers are also basic topographical elements in multilevel interconnection schemes. A crossover is a higher-level interconnection line that crosses a line situated below, with separation by an insulating layer. The use of such a metallization configuration enables the layout of VLSI circuits to be more flexible and makes further increase of the device density per unit area possible. In this chapter, I will perform a 3D thermal analysis for triple-level parallel and crossing interconnection-line structures, and compare the results with those of single-level parallel lines. Furthermore, the significant impacts of interlevel and passivation dielectric materials on the thermal behavior of VLSI multilevel interconnection structures will be demonstrated.

4.2 Statements of the Problem and Models

The starting point for this investigation is a number of single-level parallel Al lines as shown in Figure 4.1(a), each of which are 0.75 μm thick by 0.8 μm wide. It may represent a metallization structure in a digital VLSI circuit where, for instance, 32 such running lines are possible for a data bus. In this case, they are assumed to be equally-spaced by 4.0 μm. These lines are deposited onto a flat 1.0 μm thick layer of SiO_2 on a 300 μm thick Si wafer. The lines are buried under 1.5 μm of planarized passivation layer. The current flows through the Al lines along its longitudinal

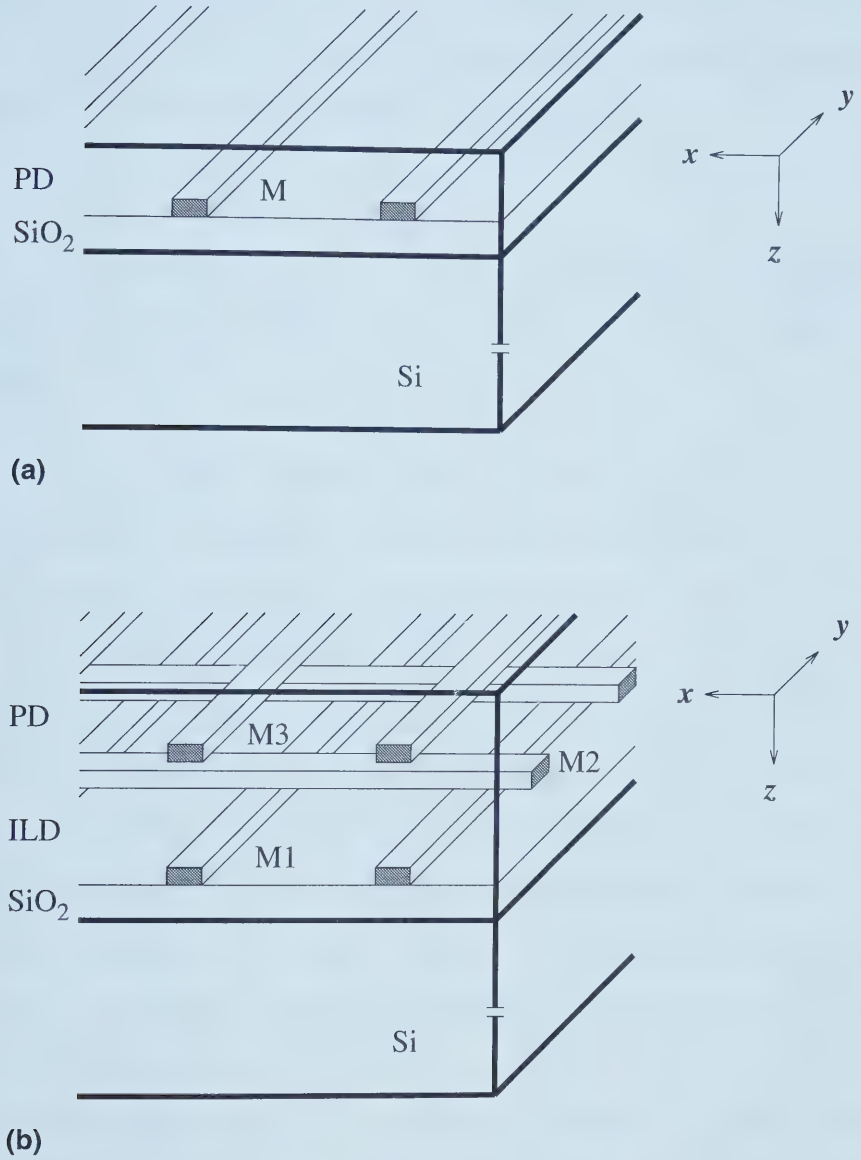

Figure 4.1 **(a)** Single-level parallel metallization lines (M) deposited on an oxidized Si substrate and buried under a passivation dielectric (PD) layer. **(b)** A general geometry of triple-level parallel and crossing interconnection lines (M1, M2 and M3) that are separated by interlevel dielectrics (ILD) [67].

direction and the Joule heating created in the metal is $J^2\rho$, where J is the current density and ρ is the electrical resistivity. In the present calculation, the temperature dependence of ρ is taken into consideration according to

$$\rho_{Al}(T) = aT \tag{4.1}$$

where a is a constant equal to 1.10×10^{-6} Ω·cm/K for Al [74]. Due to the large number of the fairly long Al lines, a 2D analysis of a repetitive area in the x-z dimensions can be justified.

Figure 4.1(b) shows a generic multilevel interconnection-line configuration. Process engineers may utilize such a scheme on a high-speed bipolar I^2L or a CMOS VLSI device. Here, the dimensions of the Al lines in each level and other geometrical parameters are identical to those stated above, while a typical thickness of 1.0 μm is assumed for the interlevel dielectric layers. Although an elemental periodic structure can again be employed, this analysis must be undertaken in three dimensions. The same sort of simplified 3D thermal analysis has extensively been used for active power transistors [29], [75], [76], and the relative error was found to be less than 5% [76]. The top surface of the structure is assumed to be adiabatic. This gives a safe estimation of temperature rise and is reasonable for many commonly-used device mounting technologies (*e.g.*, the flip-chip packaging scheme). All other sides represent the symmetry faces with zero gradient in temperature across the boundary. For convenience, the origin of the Cartesian coordinates is located at the center point of the top surface of the elemental volume in question. The z-axis points downwards because heat generated diffuses predominantly to the back contact of the chip, which

is held at an ambient heat-sink temperature of 50 °C. The thermal conductivities, specific heats, and densities for the materials used are listed in Table 4.1.

TABLE 4.1 Some Physical Properties of Materials Used in the Simulations

Parameter	Al	SiO_2	Si_3N_4	Si
Thermal Conductivity (W/cm·°C)	2.37	0.014	0.28	1.5
Specific Heat (J/g·°C)	0.896	1.00	0.73	0.70
Density (g/cm^3)	2.707	2.27	3.10	2.33

Given the conditions specified above, the 2D and 3D TLM techniques with a variable mesh and automatic time-stepping capability are used for the thermal analysis. The mesh defining the structures under consideration may be varied in each orthogonal direction so that appropriate node densities may be allocated to different regions in accordance with the thermal gradients expected, *e.g.*, the mesh is relatively fine around the metal lines and coarse for the Si substrate. Although the TLM method is especially useful for transient simulations, the eventual temperature distributions of interest here can be found by allowing the continuation and speeding up of the thermal diffusion processes to reach steady states. The method has been employed successfully and proved to be computationally efficient for solving a number of non-linear heat flow problems of microelectronic devices with complex geometries and fabricated with a variety of different materials [29], [32], [64].

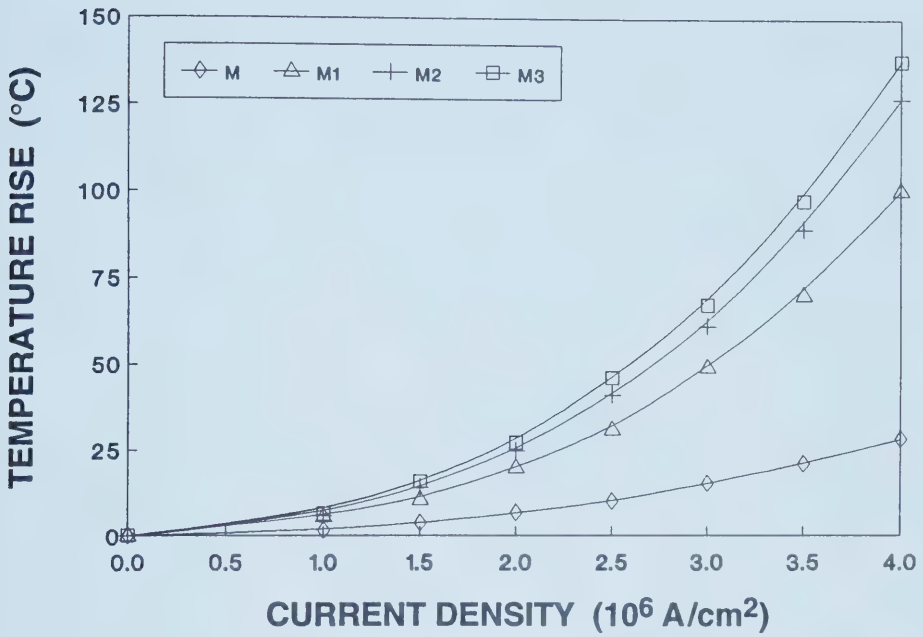

Figure 4.2 Temperature rise versus current density in single-level (M) and triple-level (M1, M2 and M3) interconnection lines, where SiO_2 is used as the interlevel and passivation dielectrics [67].

4.3 Results and Discussion

Figure 4.2 shows the calculated line temperatures above the ambient as a function of current density. The temperature increase of the triple-level metallization is found to be much higher than that of the single-level lines if the same magnitude of current density is maintained. This is due to the obvious difference in density of metal lines or heat sources within which power is dissipated. In spite of the fact that M1 is configured at the same position as M [see Figures 4.1(a) and 4.1(b)], the higher temperature of M1 can be understood by its interactions with M2 and M3. The temperature in the top-level metallization line (M3) is the highest since it is the most

isolated from the heat sink at the bottom of the substrate. For a current density of 2×10^6 A/cm^2, the values of temperature rise in M1, M2 and M3 are, respectively, 3.0, 3.75 and 4.1 times of that of M. These ratios will become 3.55, 4.5 and 4.9, respectively, when the current density is doubled. The increase of the ratio with increasing the current density is an indication of the strong temperature dependence of the Al electrical resistivity.

Figures 4.3 and 4.4 illustrate the isometric views of the vertical temperature distributions containing the maximum value of temperature at a current density of 4×10^6 A/cm^2 for single- and multi-level interconnections, respectively. Because of the large magnitude of the metal thermal conductivity, the temperatures within the interconnection lines are uniform. On the other hand, the temperature gradient within the SiO_2 insulator between M1 and M2 at this particular high current density is as large as 26 °C/μm.

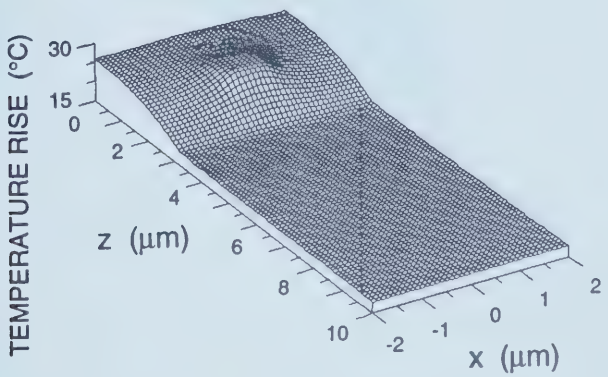

Figure 4.3 Isometric projection of the temperature distribution for the single-level interconnection structure with SiO_2 passivation. Current density is 4×10^6 A/cm^2 [67].

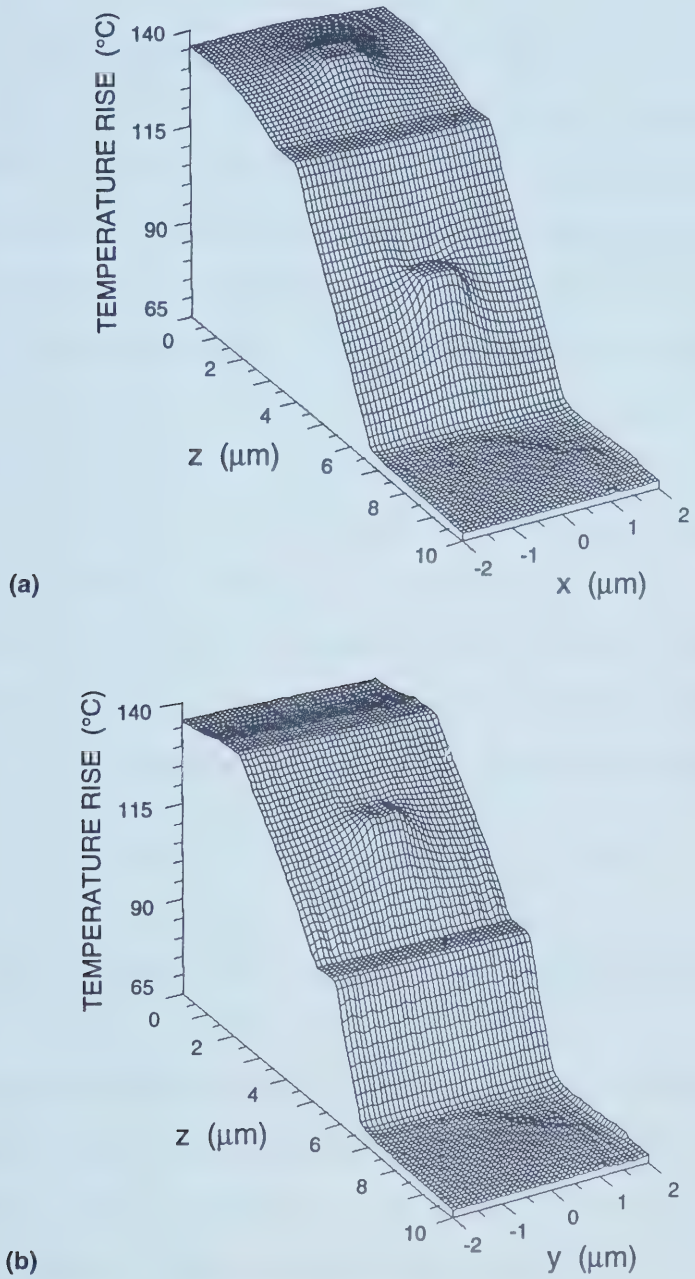

Figure 4.4 Isometric projection of the temperature distribution over the x-z **(a)** and y-z **(b)** planes through the center of the triple-level interconnection structure. Interlevel and passivation dielectrics are SiO_2. Current density is 4×10^6 A/cm^2 [67].

There might be some alternative materials which can be used as the interlevel and passivation dielectrics. If employing Si_3N_4 [77], a material whose thermal conductivity is on the order of 20 times greater than SiO_2, in the multilevel scheme, one can almost completely eliminate the aforesaid large thermal gradient and reduce the temperature rise substantially at the same time. This effect is shown clearly in Figure 4.5 using the isometric view as well. However, the higher dielectric constant of Si_3N_4 and the presence of hydrogen which introduces interface states pose other technological problems. In practice, silicon oxynitride films with properties intermediate between Si_3N_4 and SiO_2 have been shown to be a promising material for final device passivation applications [78]. Although SiO_2 will continue to remain the dominant primary interlevel dielectric, a process for depositing novel materials with good thermal properties would be advantageous. This will be further illustrated by using Si_3N_4 as a representative material of high thermal conductivity.

Figure 4.6 compares the temperature rise along the center of the vertical direction for the structures with SiO_2 and Si_3N_4 as the interlevel and passivation dielectrics at several values of current density. The solid lines for the case of SiO_2 in Figure 4.6 are evidently step-shaped near the surface, and the positions of Al interconnection lines can be identified easily. In contrast, the dashed lines for the case of Si_3N_4 in the same regions are quite uniform, exhibiting 14% and 37% decreases in the maximum temperature rise for the current density of 2×10^6 and 4×10^6 A/cm^2, respectively. In these calculations, I have used the bulk material properties as shown in Table 4.1. Recent measurements [79] of thin SiO_2 films showed a lower thermal conductivity than bulk material, which is also dependent on the film thickness as well as the processing conditions. The observations presented here should be still valid if using

the comparatively smaller values of thermal conductivity of both the SiO_2 and the Si_3N_4 films. In Figure 4.6, the temperature profiles along the initial 50 μm from the top surface in the z-direction are shown. The temperature decreases gradually within the 300-μm thick Si substrate, ultimately reaching the heat-sink value at the bottom. It can be found that there is about 50% temperature rise occurring in the Si substrate for the case of SiO_2 as the interlevel and passivation dielectric materials. The percentage becomes even larger when Si_3N_4 is used. This means that the Si substrate is by no means a perfect heat sink, although the assumption has been used frequently in many previous reports on thermal analysis of metallization structures.

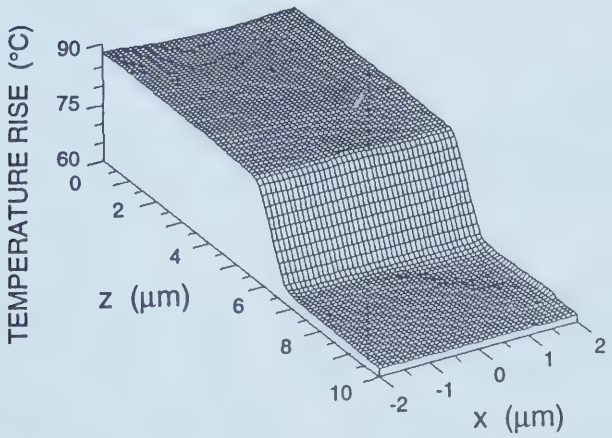

Figure 4.5 The same isometric projection over the x-z plane as that in Figure 4.4, but with the interlevel and passivation dielectrics being Si_3N_4 [67].

According to the Arrhenius-like relationship of electromigration originally formulated by Black [80], [81], the median time to failure (MTF) can be given by

$$\text{MTF} = AJ^{-n} \exp\left(\frac{\Delta E}{kT}\right) \tag{4.2}$$

where ΔE is the activation energy, k is Boltzmann's constant, and A and n are empirical constants. Therefore, the consequence of changing temperature from T_1 to T_2 on MTF can be expressed as a factor in the following form

$$\frac{\text{MTF}(T_2)}{\text{MTF}(T_1)} = \exp\left[\frac{\Delta E}{k}\left(\frac{1}{T_2} - \frac{1}{T_1}\right)\right] \tag{4.3}$$

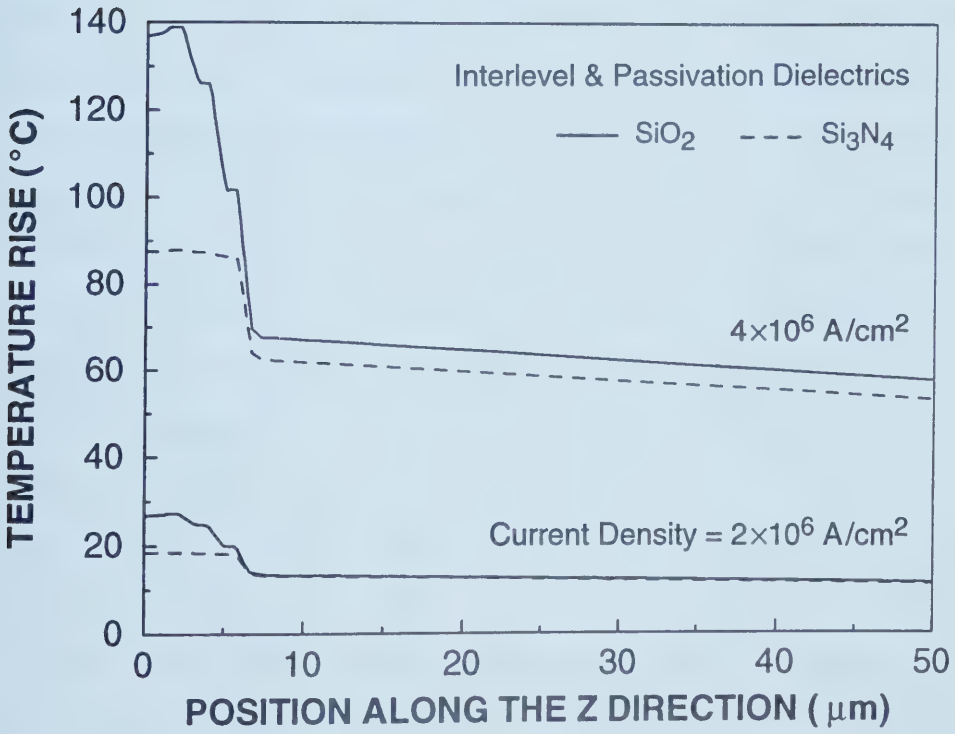

Figure 4.6 Temperature rise along the center of the z-direction for the triple-level metallization structures [67].

Based on the data presented in Figure 4.6 and with assuming a 0.6 eV for ΔE, the thermal effects of replacing SiO_2 by Si_3N_4 as the interlevel and passivation dielectrics

will result in 1.7 and 6.5 times improvements in electromigration lifetime for the top-level conductor (M3) at a current density of 2×10^6 and 4×10^6 A/cm^2, respectively.

4.4 Conclusions

In summary, the thermal behavior of high density multilevel interconnection systems in VLSI circuits has been quantitatively analyzed. This study is a full 3D TLM simulation with the appropriate boundary conditions and without neglecting the heat flow anywhere in the domain of a periodic structure (including inside the Si substrate). The temperature increase due to Joule heating of a general triple-level metallization is found to be several times higher than that of a single-level metallization when the same magnitude of current density is maintained. More than 50% of the temperature rise occurs across the Si substrate; the treatment of which as a perfect heat sink in many previous thermal analyses of metallization structures is, therefore, inadequate. The temperature rise can be significantly reduced if one replaces the SiO_2 interlevel and passivation layers by a material with high thermal conductivity, such as Si_3N_4. This effect is beneficial for improving electromigration lifetime and reducing stress voiding. It is important to emphasize that the dielectric materials used in multilevel interconnection systems serve not only as insulation and passivation layers but also as paths for heat removal.

Chapter 5

Thermal Diffusion: Transient Analysis

5.1 Introduction

Reliability issues with respect to thin-film interconnects in VLSI circuits are an important current concern. These include not only the well-known electromigration phenomena [6], [19] for interconnects under continuous or intermittent current stresses [84]-[86] over a relatively large time scale, but also the extreme case of instantaneous failure caused by an energetic current transient. Thin metal films with small feature sizes are susceptible to electrical overstress (EOS), especially for field-programmable gate array (FPGA) devices that use voltage programmable links (VPL's) [87]. When a VPL-based FPGA device is programmed, permanent links are formed by breaking down the dielectric between two adjacent conducting layers using a high current pulse. The charge dump comes from either a large drive transistor [87] or the capacitance of the metal line [88], and the peak value may greatly exceed the 2-5 mA operation current provided by the external circuits. Although this programming

---

The material in this chapter has been published as References [82] and [83].

pulse is very short-lived (on the order of 1 ns to 1 μs), the amount of heat generated along the metal lines away from the link must be kept below an appropriate limit. Otherwise, differential thermal expension with substrate materials causes local stresses which may break the metallization.

A recent investigation [89] reported a simple treatment and rough estimation for the temperature rise due to the Joule heating created by high current pulses in metal line of the FPGA devices. In this chapter, I perform a more detailed thermal analysis with minimal assumptions. The time-dependent nature of the problem will be demonstrated together with the limiting cases of adiabatic and steady-state conditions. Specifically, the significant effects of dielectric passivation on the transient temperature distribution in metallization structures and the comparison of single-level and multilevel systems will be emphasized.

5.2 Models of Single-Level Metallization Systems

In a digital VLSI circuit, a number of fairly long lines in parallel are usually employed. Here, these lines are assumed to be 4.0 μm apart between centres, and are deposited onto a field SiO_2 layer grown over a 300-μm thick Si wafer. From the point of view of thermal assessment, a 2D analysis of a repetitive area with reflective boundary conditions at the two sides can be justified. Figure 5.1 illustrates the geometries under consideration. Both unpassivated lines and lines buried under a 1.5-μm planarized passivation layer are considered. The temperature dependence of the Al electrical resistivity is also taken into account according to Equation (4.1). The

thermal conductivities, specific heats and densities for the materials used are listed in Table 4.1. The TLM thermal simulator [29] is employed for the analysis.

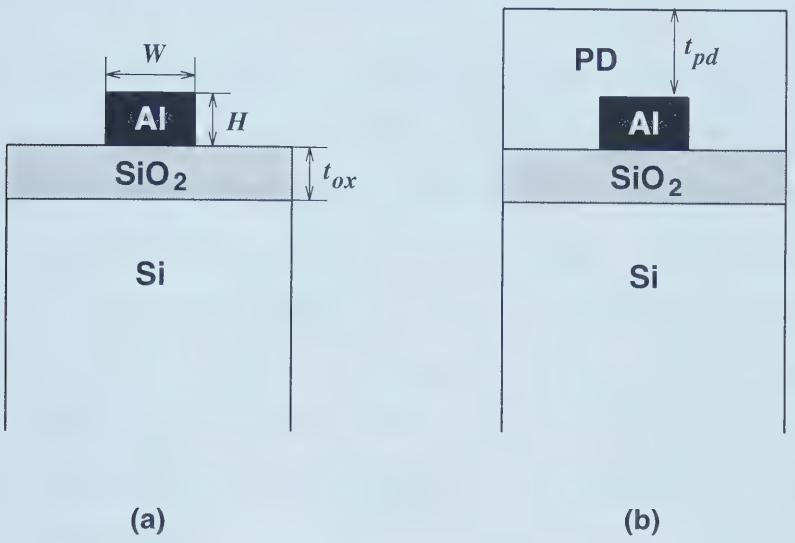

Figure 5.1 Elemental cross-sections of metallization structures without **(a)** and with passivation **(b)**. In the simulation, the Al line width $W = 0.8$ μm, height $H = 0.6$ μm, the thickness of the SiO_2 layer $t_{ox} = 1.0$ or 0.5 μm, and the passivation dielectric (PD) thickness $t_{pd} = 1.5$ μm [82].

5.3 Results and Discussion

In this section, I describe some results of thermal transient simulations started with the whole structure at a uniform background temperature of 50 °C, which is also the heat-sink temperature held at the back contact of the Si chip. According to Kim and Sachse [90], mismatch of thermal expansions of the film and substrate materials can result in a characteristic failure temperature of metal lines much lower than the

melting point. This fracture temperature (θ_f) was determined to be 300 °C for Al on SiO_2. I will use this value as the failure criterion for Al interconnects subjected to a high current pulse although θ_f may also be influenced by interface conditions, processing procedures and other possible factors.

Figure 5.2 shows the calculated relationships between time and maximum allowed current density for various oxide thicknesses and passivation conditions. Besides that pulses with higher current densities can be supported by the Si substrates with thinner oxides, there are several distinguishing features of the data. If the heating time of a metal line is short enough compared with the thermal diffusion time, then the maximum allowed current density will not depend on the presence and property of other materials around the metal line. Figure 5.2(a) also includes a curve of the simplified expression for the completely adiabatic case, which was derived from energy conservation [89]

$$J^2 t = 10^8 \ (A^2 \cdot sec/cm^4) \tag{5.1}$$

where J is the current density and t is the pulse duration time. As expected, it is situated below the curves based on my numerical simulation. It can be found that the adiabatic approximation is only valid for an extremely short pulse duration—smaller than 10^{-8} seconds for unpassivated as well as SiO_2 passivated films and even smaller ($\sim 2\times10^{-9}$ seconds) for Si_3N_4 passivated films. On the other hand, the current densities at which θ_f is reached are not so remarkably different for the above samples at steady state (in the proximity of $J = 10^7$ A/cm^2) when compared with transient situations. Heat generated in the metal will diffuse ultimately into the Si substrate through the SiO_2 layer which is a poor thermal conductor, hence dielectric overcoating would have less effects comparatively on heat removal after the thermal equilibrium is

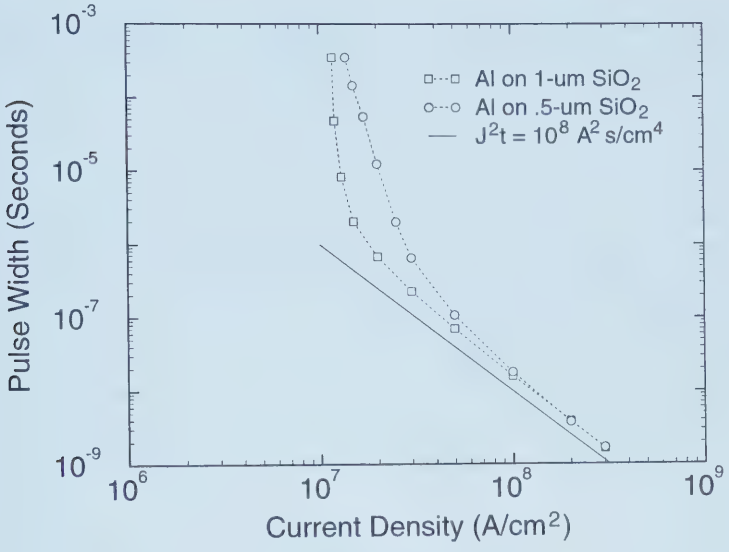

(a)

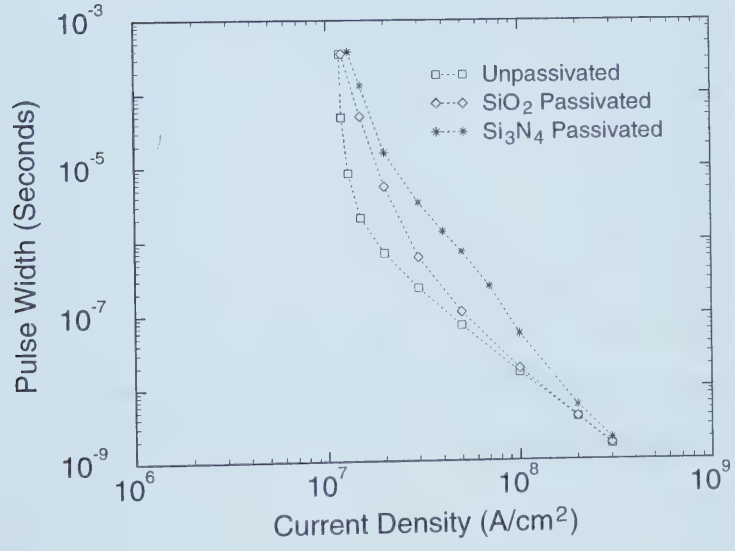

(b)

Figure 5.2 Simulation results of pulse width vs maximum current density which can be applied to Al lines as shown in Figure 5.1. **(a)** Unpassivated Al films sitting on top of 1.0- or 0.5-μm thick oxides. A curve of the simple adiabatic expression $J^2t = 10^8$ A^2·sec/cm^4 is also included. **(b)** Effects of dielectric passivation (the thickness of the underlying SiO_2 is $t_{ox} = 1.0$ μm) [82].

established. Under transient conditions, however, the thermal capacity of passivation materials inhibits the rate of temperature rise of the metal lines in a much more effective way. As a result, the maximum current density is significantly increased. For instance, the values for SiO_2 and Si_3N_4 passivated films are, respectively, 1.50 and 2.35 times of that for unpassivated films for a 1-μs pulse duration. It is interesting to note that the shape of the curve for Si_3N_4 passivated films demonstrates additional structure. This can be understood by the fact that two thermal time constants (*i.e.*, for Si_3N_4 and SiO_2) associated with the heat diffusion are involved for the Si_3N_4/Al/SiO_2 material system.

In Figure 5.3, the passivation effects discussed above are further visualized by isometric projection of the transient temperature distributions. As a thermal load, the passivation layer absorbs some of the energy of a current surge and spreads out the temperature rise. Si_3N_4 has a much higher thermal conductivity (20 times greater than SiO_2), so the effects are very obvious for the Si_3N_4 passivated films. Additional simulations have revealed that the dielectric passivation effects are relatively independent of the metal film geometry. This means that the percentage improvements on the temperature rise remain approximately unchanged by varying the size of either SiO_2 or Si_3N_4 passivated metal lines with respect to those without passivation, as long as the current density is kept the same. Therefore, it would be appropriate to use a metal line geometry with representative thickness and width values for showing the effects. Meanwhile, one should bear in mind that insulating materials with a higher thermal conductivity also have, in general, a higher dielectric constant. As a consequence, cooling chips with such a dielectric may add line capacitance and reduce device speed. Nevertheless, passivation is an indispensable

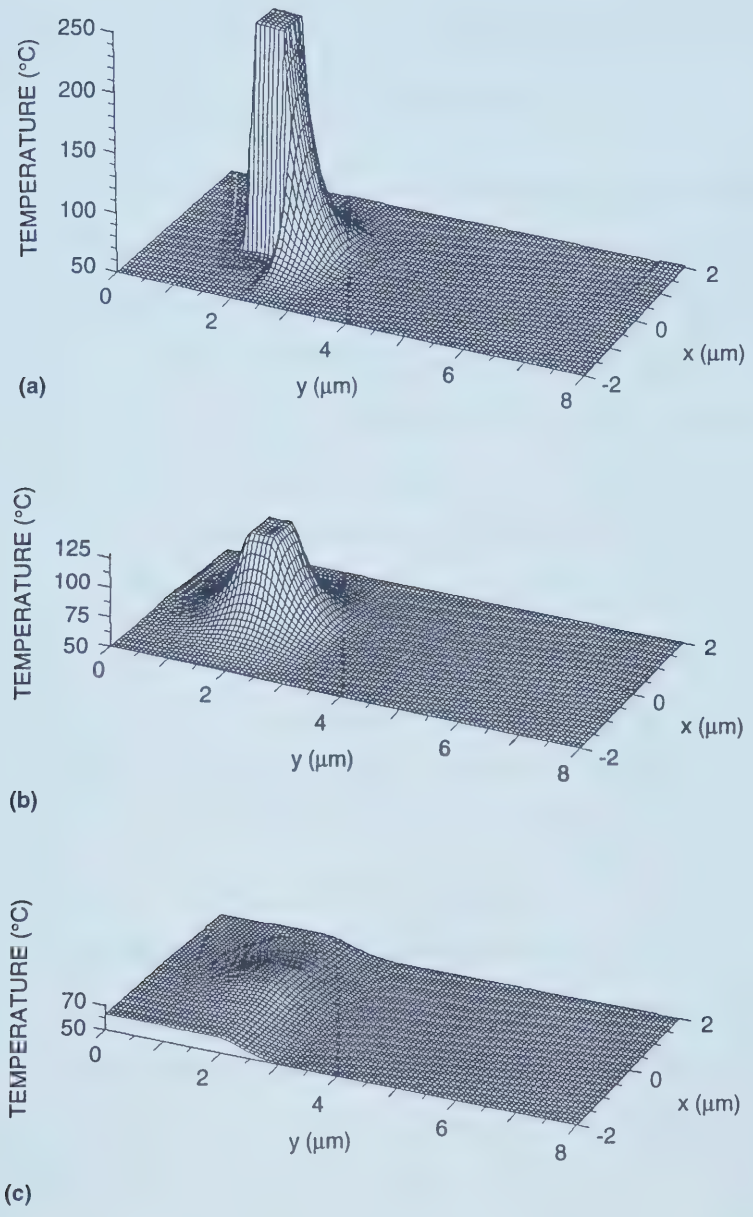

Figure 5.3 Isometric views of temperature distributions over the cross-sections of the metallization structures. For convenience of the comparison, the same coordinate scale is used. Current density is 2×10^7 A/cm^2, pulse duration is 0.5 μs. **(a)** Unpassivated. **(b)** SiO_2 passivated. **(c)** Si_3N_4 passivated [82].

process for today's VLSI devices, and the advantage of depositing dielectric materials with good thermal properties has clearly been demonstrated.

Some of the previous experimental data of line temperature measurements [89], [74] differ significantly from each other. The accuracy attainable experimentally is a problem as transient temperature response to a short current pulse is very difficult to measure in practice. Moreover, the influence of electrical resistivity (ρ) could be a further reason responsible for the discrepancy between the present calculation on Al films and the data reported in Reference 89, where a stack of Al-Si and Ti films were employed. Al alloy films generally have larger values of ρ, *e.g.*, about 1.3-1.8 times of pure Al for Al-1%Si-1%Ti or Al-1%Ti films [91], and the temperature dependance of ρ is also different. Although the alloy addition is beneficial to improving the electromigration resistance [6], the increase of ρ would enhance the Joule heat generation and reduce the maximum current density if the same θ_f is assumed. Finally, it is worthwhile to note that the curves shown in Figure 5.2 represent the limits of the simulation. A fairly high current pulse even in the admissible region might result in a degradation long before a catastrophic failure of the metal line, and the damage position would most likely become a weak site prone to electromigration failure. Considering this possible relationship between instantaneous pulse damage and long-term electromigration failure, appropriate care must be exercised when driving a high current pulse through a microcircuit.

5.4 Energetic Transients in Multilevel Metallization Systems

It should be noted that single-level metallization structures are used in the above analysis. A multilevel metallization system is necessary for FPGA and many other integrated circuits, where metal lines may be placed several micrometres above the Si surface. The influence of the resultant large time constants on the behaviour of thermal transients remains unclear. This section intends to clarify the problem through a comparison of the temperature response to high current pulses in single-level and multilevel metallization systems.

In Chapter 4, I have performed a steady-state thermal analysis for generic single-level and triple-level interconnect structures, which are also used here with SiO_2 as the interlevel and passivation materials. As discussed in Chapter 4, a 2D analysis of a periodically repetitive element in the x-z dimensions can be justified for the single-level structure, while the analysis for its multilevel counterpart has to be undertaken in three dimensions.

Figure 5.4 illustrates the maximum temperature in the multilevel structures as a function of pulse duration for two extreme cases:

- Case A: Only one metallisation level is stressed with a high current density.
- Case B: The high current pulse is driven through all three levels simultaneously.

The temperature response of the single-level scheme is also shown for comparison. Due to the presence of a thicker equivalent passivation layer leading to a longer time constant, the temperature of the line at the first level (M1) in Case A is lower than that

of the single-level line (M). Case B represents a worst case scenario, which exhibits obviously higher temperatures because all the metal lines are heated at the same time. In this case, it is interesting to note that the line situated in the middle (M2) is even hotter than the third level line (M3) within a short range of pulse width; but with the establishment of the thermal equilibrium, M3 eventually becomes hotter as it is further away from the heat sink on the bottom of the substrate.

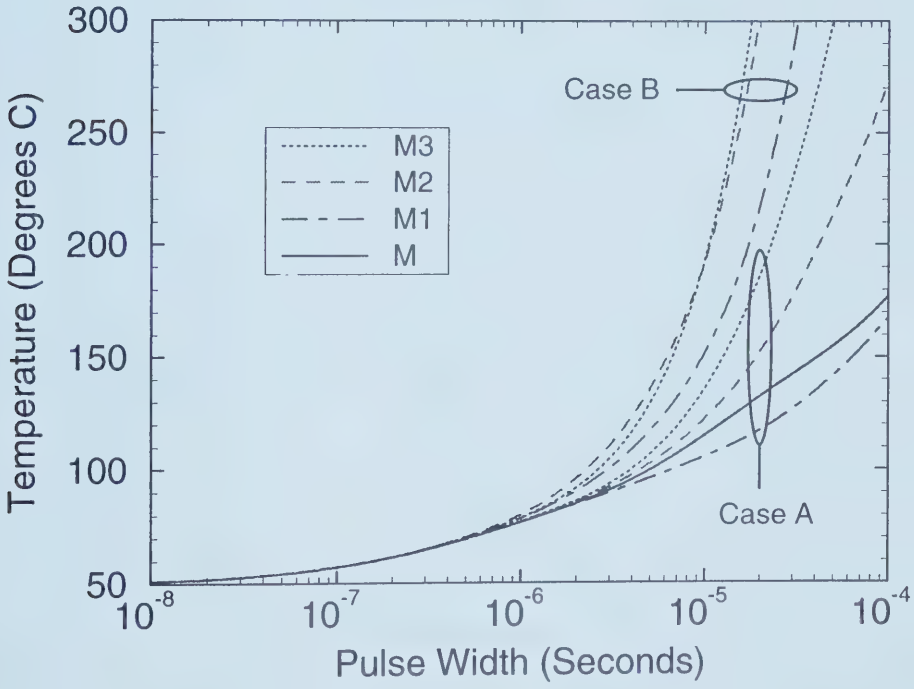

Figure 5.4 Temperature of Al lines vs pulse width for metallisation structures shown in Figure 5.1 at a current density of 1×10^7 A/cm^2. Besides the solid line for the single-level metallisation structure, two cases for the triple-level scheme are displayed. Case A: only one level is stressed with a high current density. Case B: All levels are subjected to the transient current at the same time [83]

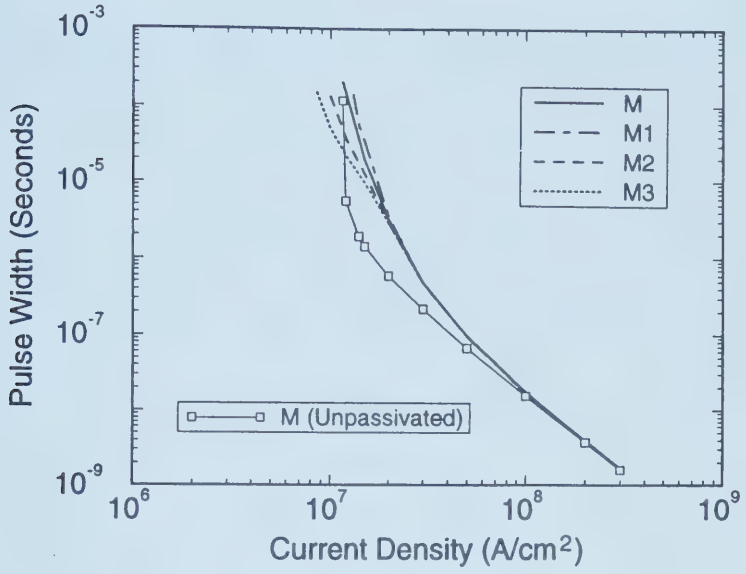

(a)

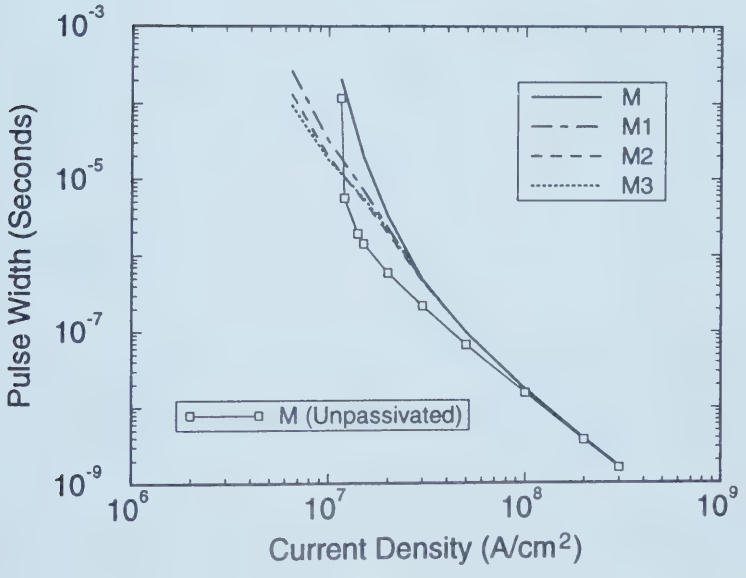

(b)

Figure 5.5 Pulse width vs maximum allowed current density, corresponding to an Al-film fracture temperature of 300 °C. **(a)** Case A. **(b)** Case B (see text or the caption of Figure 5.4 for the definition) [83].

Figure 5.5 shows the relationships between the pulse duration and the maximum allowed current density for both cases. It can be seen that the calculation with respect to the single-level structure represents a good estimation for multilevel lines when the pulse duration is below a certain value (approximately 1.0 μs for Case A and 0.5 μs for Case B). This means that if the heating time of a metal line is short enough compared with the thermal diffusion time, the maximum current density will not depend on the location of the metal line. For a longer heating time, the deviation becomes apparent, and such an approximation is invalid. When approaching the ultimate steady state, the line temperature at different levels for a multilevel structure will be different from each other. The curve for unpassivated single-level structure is also drawn in Figure 5.4. As indicated in Section 5.3, the thermal capacity of passivation materials significantly slows the rate of temperature rise of the metal lines by increasing the time constant. Therefore, this effect should be considered under transient conditions.

5.5 Conclusions

In this chapter, I have outlined some important features of transient temperature distributions in VLSI metallization structures, with the emphasis on the significant effects of dielectric passivation. The graphs of pulse width versus maximum current density through Al interconnects presented may assist in design guideline for VPL-based FPGA and other VLSI devices.

Chapter 6

TLM Modeling of Grain-Boundary Diffusion in Thin Films

6.1 Introduction

Investigation of grain-boundary and interfacial diffusion in thin films is of great significance for the design, fabrication and reliability of microelectronic devices because most thin films employed in today's VLSI devices are polycrystalline materials, and diffusion along grain boundaries is much more rapid than bulk lattice diffusion [22]. Practical concerns associated with grain-boundary diffusion have included electromigration [6], impurity diffusion in polycrystalline silicon [92]-[95] and silicides [96], and the effectiveness of diffusion-barrier layers inserted between the conducting films and the semiconductor substrate [23].

The interest in studying grain-boundary diffusion is now continuing not only for its technological importance but also due to the need for an improved understanding of the fundamental physical metallurgy and characteristics. A number of mathematical

---

Some of the material in this chapter has been published as Reference [50].

models of grain-boundary diffusion have been developed since the early 1950's. The Fisher model [97], and the Whipple [98] and Suzuoka [99] solutions represent pioneering and classic studies for semi-infinite samples. In 1976, Gilmer and Farrell [100], [101] published an exact solution for thin film systems. In addition, grain-boundary diffusion at lower temperatures was investigated by Hwang, Pan and Balluffi [102], [103]. These studies have been used for obtaining the concentration profiles and determining the grain-boundary diffusion coefficients.

It is important to emphasize that analytical solutions of grain-boundary diffusion are only possible with highly idealized assumptions. On the other hand, numerical solutions have fewer restrictions and are flexible with regard to complex geometry and boundary conditions. Several such studies can be found in the literature using the conventional FD approach [104], [105]. The TLM method is a relatively new and powerful alternative tool for analyzing diffusion processes. In contrast to thermal diffusion problems [27]-[29], [57], [58], [62], [64]-[67], [82], [83], few applications of the method to mass diffusion have been reported.

This chapter will demonstrate the use of the TLM method in the simulation of mass diffusion for a system consisting of regions with different diffusion coefficients. Such an application is typified by grain-boundary diffusion in thin films. Specifically, I will take into account the concentration flux along the interface between the film and the substrate as well as into the substrate, so that the solution becomes more comprehensive. These effects have largely been ignored in previous analyses with more simplified assumptions. After a brief description of grain-boundary diffusion kinetics in the next section, a preliminary modeling structure for the combined

diffusion in grains, grain boundaries, interfaces and the substrate will be introduced. Several representative calculated results together with the discussion are subsequently presented.

6.2 Grain-Boundary Diffusion Kinetics

A grain boundary is essentially a 2D transition region between two crystals having different orientations but the same periodicity [106]. Figure 6.1 shows a high-resolution transmission electron microscopic (TEM) image of a (100) tilt-type grain boundary in Au thin films [107]. Due to the complexity of the grain boundary structure, a clear atomistic picture for grain-boundary diffusion has yet to be formed and only macroscopic analysis is possible at the present time.

Consider a number of impurity atoms whose concentration C varies with position. The random walk of these atoms constitutes an effective diffusion flux J in a direction of maximum gradient (Fick's law) [108]

$$J = - D \nabla C \tag{6.1}$$

where D is the diffusion coefficient, which varies with temperature T as (Arrhenius relationship):

$$D = D_0 \exp (-\Delta E/kT) \tag{6.2}$$

where D_0 is the temperature-independent "frequency factor", ΔE is the activation energy. In general, the diffusions within the grains and along grain boundaries occur simultaneously. Table 6.1 gives several representative values of grain-boundary and intra-grain diffusion coefficients in thin films. It can be found that the activation energy of lattice diffusion is normally greater than that of grain-boundary diffusion.

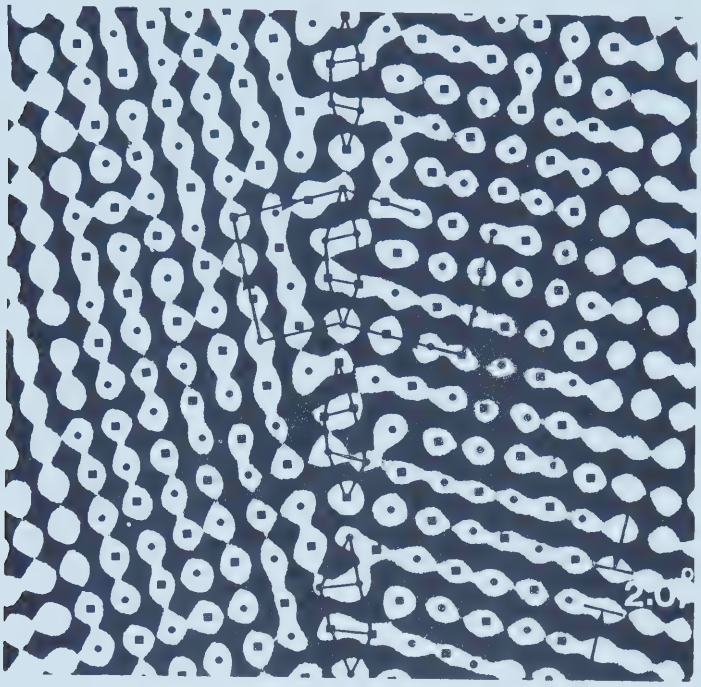

Figure 6.1 High-resolution TEM image of a large-angle grain boundary in Au thin films. Atomic positions in the two alternating stacking layers are indicated by the dots and squares [107] (Courtesy of W. Krakow)

TABLE 6.1 Grain Boundary and Intra-Grain Diffusivities in Thin Films

Diffusant	Matrix	D_{b0} (cm^2s^{-1})	ΔE_b (eV)	D_{g0} (cm^2s^{-1})	ΔE_g (eV)	Ref.
Pt	Ag	10^{-11}	0.55	10^{-11}	0.8	109
Pt	Au	4×10^{-2}	1.5	3×10^{-6}	1.55	110
Cu	Au	10^{-4}	0.91	10^{-5}	0.95	110
Pd	Au	5×10^{-6}	0.65	5×10^{-10}	0.70	110
Ni	Au	4×10^{-5}	0.75	7×10^{-6}	1.36	110

As a result, intra-grain (lattice) diffusivity D_g increases much more rapidly with temperature than grain-boundary diffusivity D_b.

According to Harrison [111], three types of kinetics regimes designated as A, B and C can be determined by the extent of coupling or the ratio of the two processes. This is illustrated in Figure 6.2, where grain boundaries are shown as parallel slabs with spacing $2L$, δ is the effective grain-boundary width of the order of 0.5 to 1.0 nm [112], d is the penetration distance of the diffusing species. Using the subscripts g and b to denote the intra-grain and grain-boundary parameters, respectively, we have

$$d_g = (D_g t)^{1/2} \tag{6.3a}$$

and

$$d_b = (D_b t)^{1/2} \tag{6.3b}$$

- *Kinetics A*: $d_g \geq L$, lattice diffusion is dominant, corresponding to the situation of high temperatures.
- *Kinetics B*: $10d_g \leq L$, each boundary is assumed to be isolated and neither of the grain-boundary and lattice diffusion is negligible. This occurs at intermediate temperatures.
- *Kinetics C*: $10d_g \leq \delta/2$, the distinguishing feature is the domination role of grain-boundary diffusion (practically no grain penetration), which should be of significance for the mass transport in thin films at low temperatures.

Historically, quantitative analysis of grain boundary diffusion began with bulk materials. B-kinetics are a regime which considers both grain-boundary and lattice diffusion. It was first treated and has been studied most extensively. I will discuss

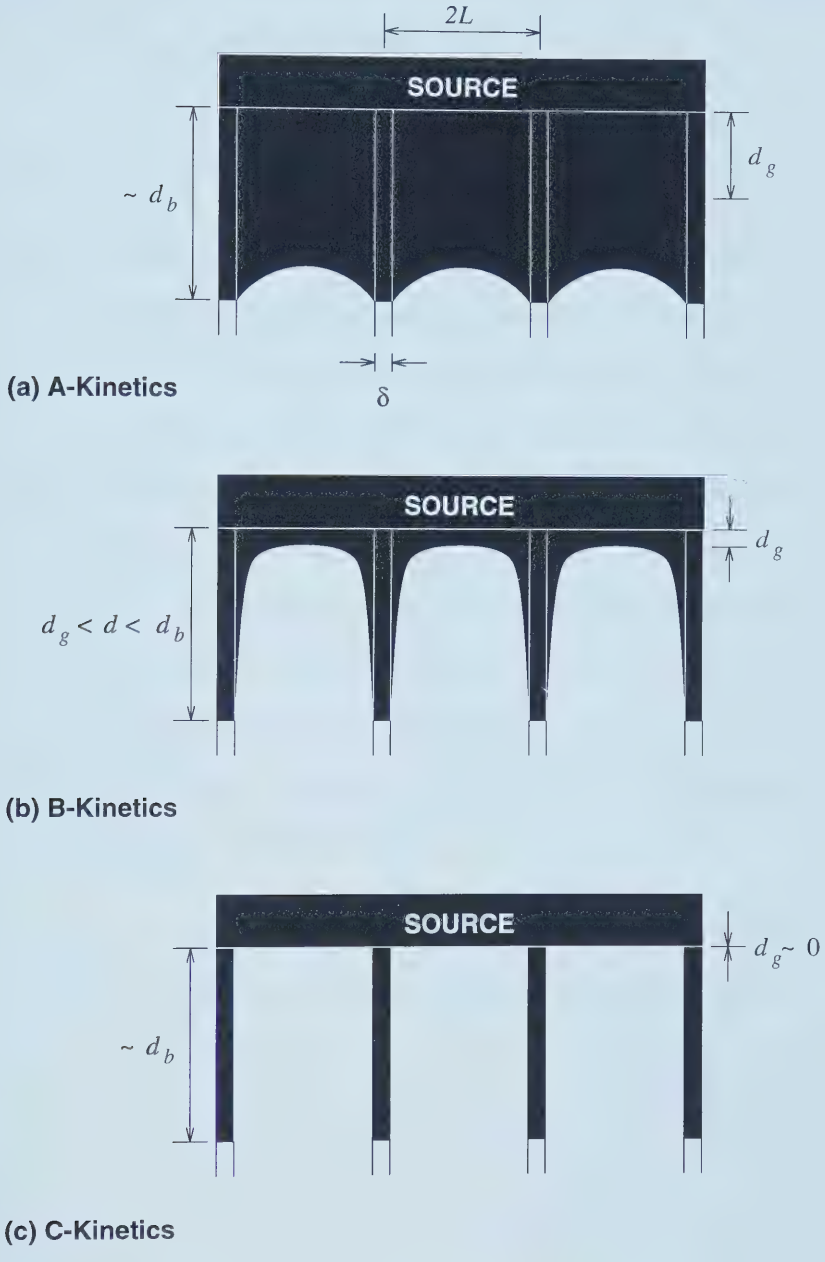

Figure 6.2 Schematic representation of A-, B- and C-kinetics. Vertical lines indicate grain boundaries and curved lines are isoconcentration contours.

grain-boundary diffusion in thin films of B-kinetics in some detail in Chapters 6 - 8, while C-kinetics will be addressed in Chapter 9.

6.3 Numerical Model for Grain-Boundary Diffusion

Figure 6.3(a) represents the structure of a film deposited on the substrate, consisting of an array of parallel grain boundaries characterized by thin slabs of a uniform width δ. These grain boundaries lie perpendicular to the surface at an average spacing of $2L$. Due to symmetry of the structure, the solution can be restricted to the region $0 \leq x \leq L$, as illustrated in Figure 6.3(b). The film thickness is l and the dimension of the interface is assumed to be half a boundary width (δ/2). The present model takes account of separate diffusion coefficients in the grains, grain boundaries, substrate and film/substrate interface, designated by D_g, D_b, D_s, and D_i, respectively. To include all this is straightforward through inter-nodal scattering in the TLM method, with a number of simultaneous equations (four coupled 2D time-dependent diffusion problems for the present case) being solved.

The OC boundary conditions in the TLM method can be used for modeling the diffusion barrier or symmetrical surfaces where the concentration gradients are zero ($\partial C/\partial x = 0$). The ML boundary condition is used at the bottom of the simulated substrate, which is helpful for extending the simulated thickness of the single crystal substrate. However, it should be remembered that the diffusion process has a natural back-scattering characteristic and that some component of a diffusing species at any location will eventually find its way back to the origin. To account for this effect in a sensible way, a relatively large dimension of the substrate is considered when using

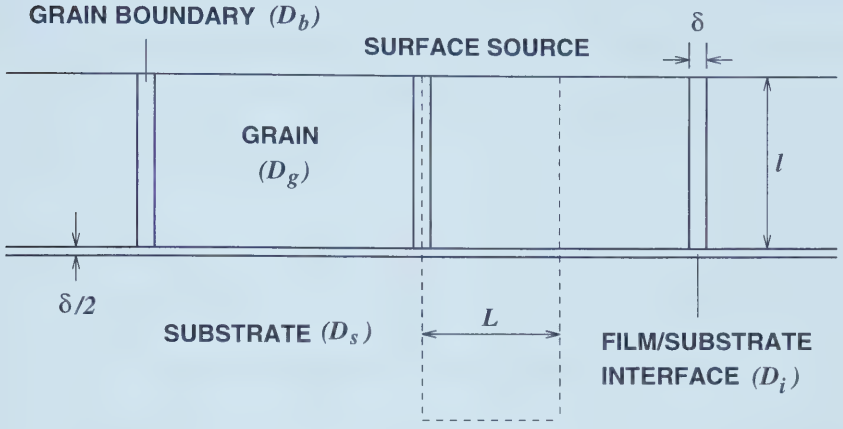

(a)

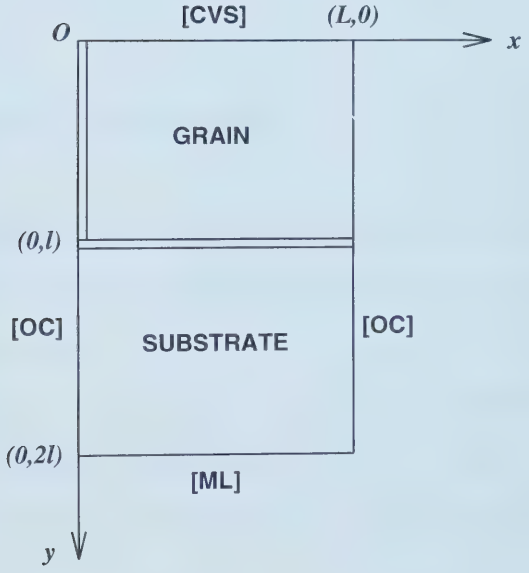

(b)

Figure 6.3 **(a)** Geometric model for the grain boundary and lattice diffusion including the effects of the substrate and film/substrate interface. **(b)** The TLM model used for the present study, corresponding to the region enclosed by the dashed line in (a) [50].

the ML condition for this purpose. On the top surface that is in contact with a reservoir of the diffusing species, the constant voltage source (CVS) with a value of unity is assumed since all material parameters may be appropriately normalized in the study of grain-boundary diffusion.

A variable TLM grid was employed to define the structure. The mesh was fine near the grain boundary, surface and interface where large concentration gradients can be expected, and it became progressively more coarse towards other areas. A single node for modeling either the grain boundary or the interface, which are physically very small, was found to give an acceptable accuracy. The results were displayed as 2D or 3D graphs for evaluating the concentration distributions as a function of position and time.

6.4 Calculated Results and Discussion

To facilitate comparison with other researchers' solutions, all the results presented in the following are obtained under the assumptions that the film has a thickness equal to one half the distance between grain boundaries ($l = L$) and that the ratio of the boundary width to the film thickness is $\delta / l = 5\times10^{-3}$. Also, plausible relationships between the different diffusion coefficients, $D_b / D_g = 10^4$ and $D_s / D_g = 10$, are employed. In addition, a dimensionless diffusion time may be defined as

$$T = \frac{D_g t}{l^2} \tag{6.4}$$

Figures 6.4 - 6.6 display three calculated examples as isometric projections and contour plots at $T = 10^{-2}$. In Figure 6.4, the concentration and its flux at the

film/substrate interface are assumed to be perfectly continuous ($D_i = D_s$). Due to the substantial differences between D_b and D_g, and between D_b and D_s, the grain for the boundary region has been saturated with the atoms coming from the surface source. A distinctive feature exhibited here is that the concentration gradients are very large near the surface and in the proximity of the grain boundary. Although some atoms have diffused into the substrate to a relatively far distance due to the fact that the diffusion coefficient assumed for the substrate is greater than that for the grains of the film, all the boundaries are still effectively isolated. As a consequence, the concentration profile for the system containing multiple grain boundaries is essentially the same as that containing only one single grain boundary. This is similar to the situation discussed in Reference 101, where there was no substrate present. In many cases, these results may be applied to other systems with different geometries as long as i) the substrate effect does not become appreciable, and ii) the reduced time is much smaller than the square of the aspect ratio, *i.e.*, $T << (L/l)^2$. Physically, the second condition means that the diffusion penetration length into the grains is small compared with the distance from the grain boundary to the centers of the gains on both sides ($d_g << L$).

In Figure 6.5, the film/substrate interface as a fast diffusion path is simulated, and the ratio between the diffusion coefficients of the interface and grains is assumed to be $D_i / D_g = 10^3$. The effects of both interface and substrate can be seen very clearly from the isometric projection and contour graph. Even though the dimension of the interface in the y direction is very small ($\delta/2$), the concentration at a position along the interface can be found to have the same value as that within the substrate but closer to the grain boundary. For this case, the grain boundary region is not saturated

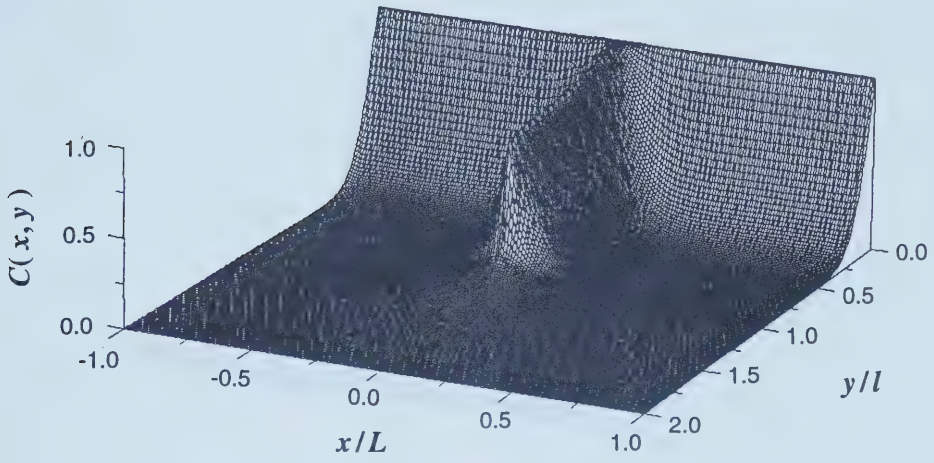

(a)

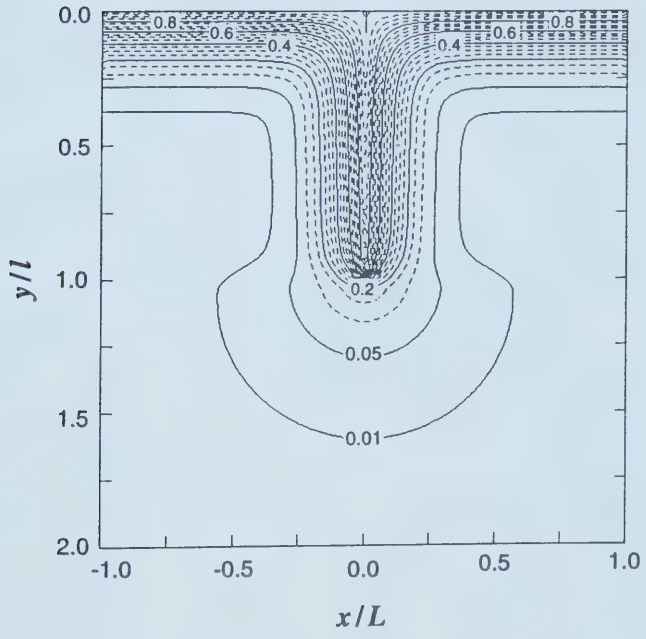

(b)

Figure 6.4 Simulated concentration distributions under the geometrical conditions $L/l = 1$ and $\delta/l = 5\times10^{-3}$ and at the reduced time $T = 10^{-2}$. Here $D_b/D_g = 10^4$, $D_s/D_g = 10$ and $D_i/D_s = 1$. **(a)** Isometric view. **(b)** Contour plot [50].

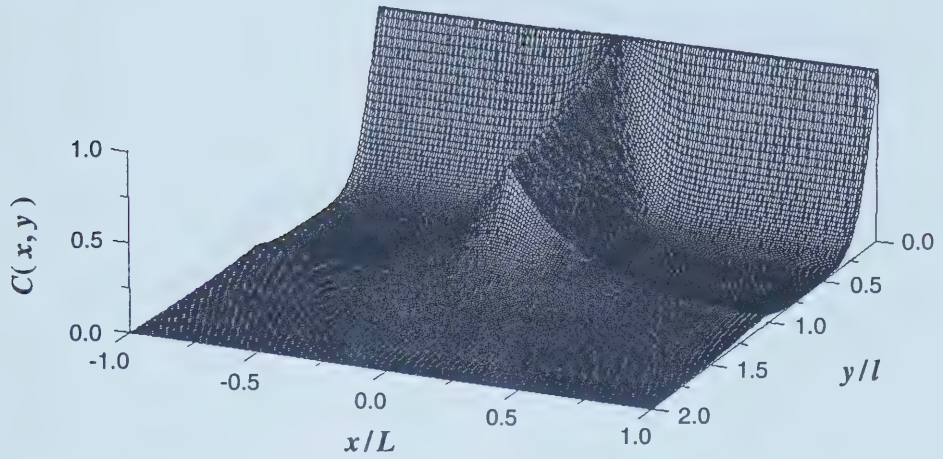

(a)

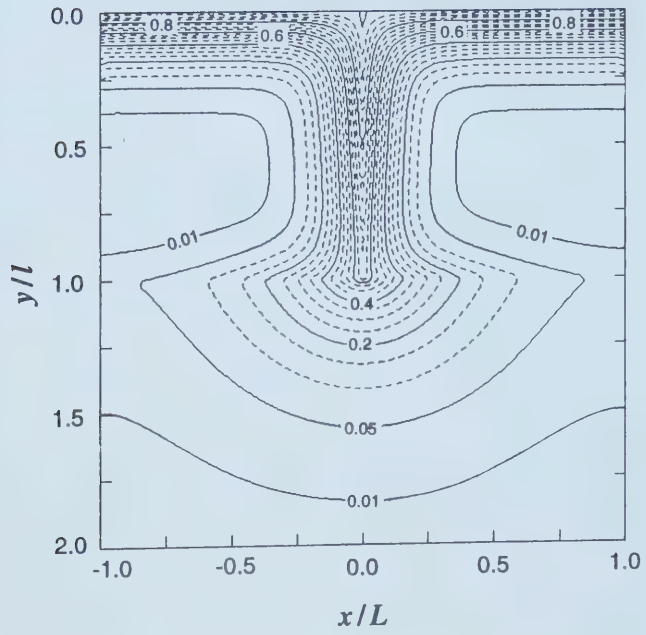

(b)

Figure 6.5 Simulated concentration distributions under the geometrical conditions $L/l = 1$ and $\delta/l = 5\times10^{-3}$ and at the reduced time $T = 10^{-2}$. Here $D_b/D_g = 10^4$, $D_i/D_g = 10^3$ and $D_s/D_g = 10$. **(a)** Isometric view. **(b)** Contour plot [50].

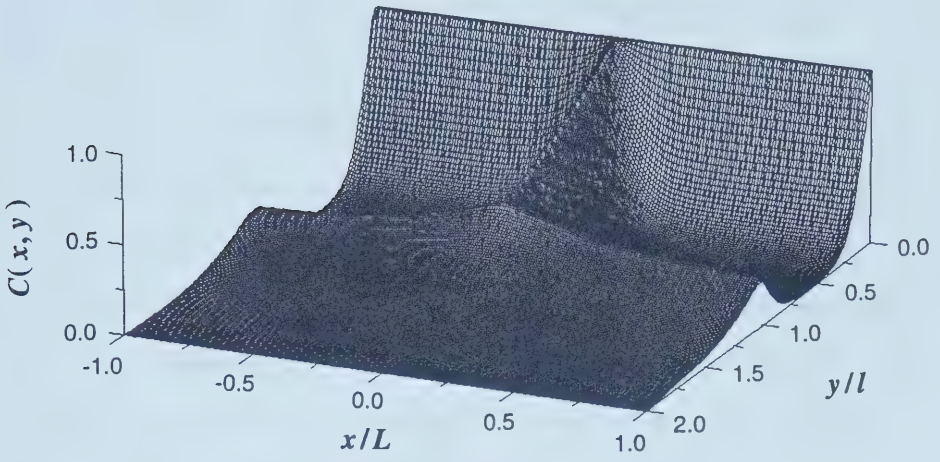

(a)

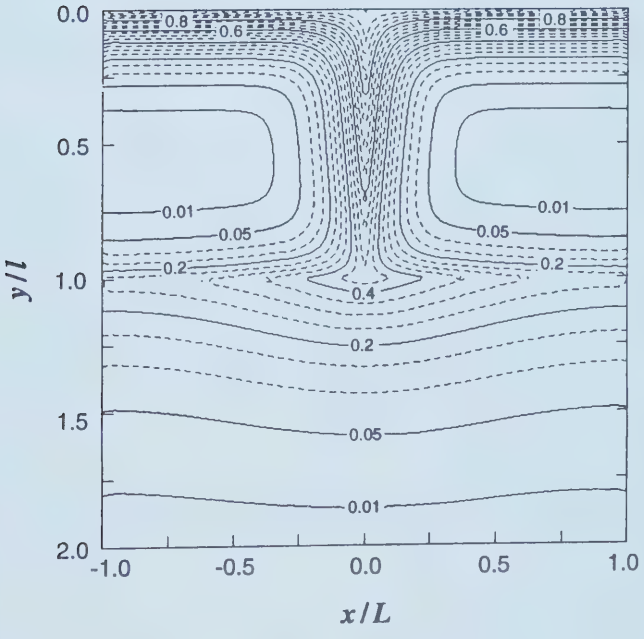

(b)

Figure 6.6 Simulated concentration distributions under the geometrical conditions $L/l=1$ and $\delta/l = 5\times10^{-3}$ and at the reduced time $T=10^{-2}$. Here $D_b/D_g=10^4$, $D_i/D_g=10^4$ and $D_s/D_g=10$. **(a)** Isometric view. **(b)** Contour plot [50].

and the atoms keep moving through the fast transport trails of the boundaries and interface. The boundaries are no longer isolated and the concentration distributions become geometry-dependent. Moreover, the interface may serve as a second source for the diffusion back into interiors of the grains. Additional simulations indicate that a larger dimension and/or diffusion coefficient of the interface will result in a larger concentration gradient along the grain boundary (in the y direction) and form the new diffusion source at the interface (in the x direction) more effectively. Figure 6.6 illustrates such a situation, where the diffusion coefficient of the interface is assumed the same as that of the grain boundaries. Because of the higher concentration at the interface, the isometric view of the concentration in the substrate looks more like an inclined plane, whereas that in Figure 6.5 is in the shape of an elliptic cone.

If the substrate and interface are completely impenetrable to the atomic diffusion, then the backside of the film becomes a diffusion barrier, *i.e.*, $\partial C(x, l, t)/\partial y = 0$. The analytical solutions to this idealized problem have been derived by Gilmer and Farrell [100], [101]. In the present TLM model, these conditions can be simulated simply by removing the substrate and interface, and using an OC termination instead. Calculated results are presented in Figures 6.7 and 6.8 (solid lines "a"), in terms of the concentration averaged over the x dimension $\bar{C}(y,t)$ versus the normalized distance in the y dimension y/l. This averaged concentration as a function of position and time is the most frequently measured parameter in depth-profiling experiments. It is defined as

$$\bar{C}(y,t) = \frac{1}{L}\int_0^L C(x,y,t)\,\mathrm{d}x \tag{6.5}$$

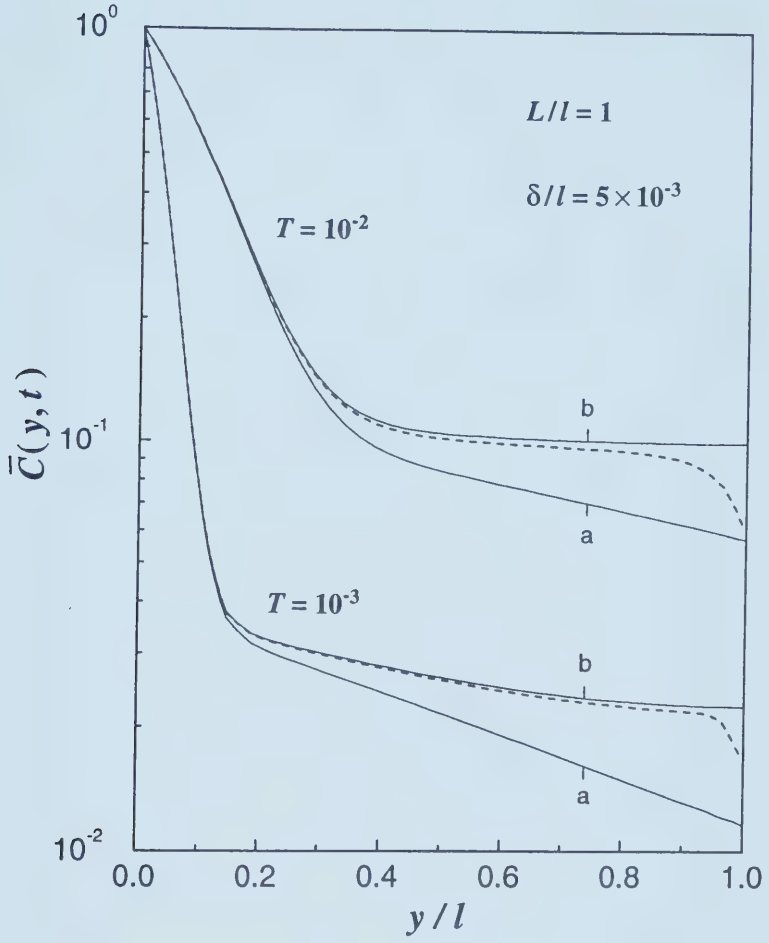

Figure 6.7 The average concentration $\ln \bar{C}(y, t)$ versus the normalized distance into the film y/l for two values of the reduced time T. All the curves shown here and in Figure 6.8 are obtained by the TLM method. The solid lines symbolized by "a" are based on the Whipple model and "b" the Gilmer-Farrell model. Substrate effects are shown by the dashed lines, corresponding to the case of Figure 6.4 [50].

To the other extremity, if the film becomes a semi-infinite sample, then the problem reduces to the Whipple solution [98]. This can be realized in the TLM model by

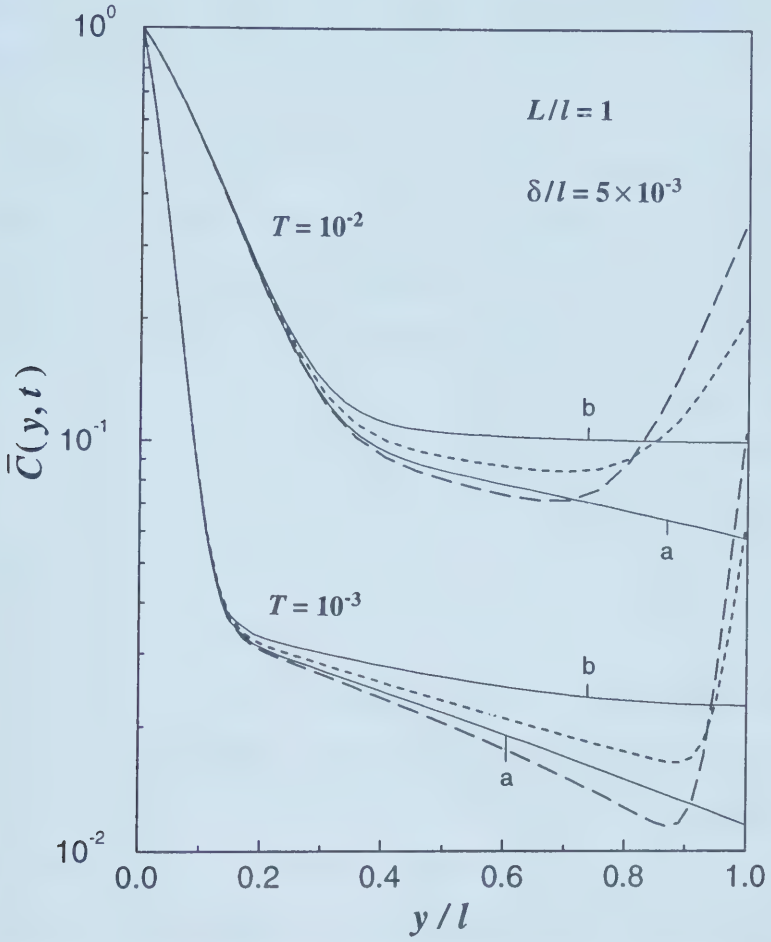

Figure 6.8 The average concentration $\ln\bar{C}(y, t)$ versus the normalized distance into the film y/l for two values of the reduced time T. The solid lines symbolized by "a" are based on the Whipple model and "b" the Gilmer-Farrell model. Substrate and film/substrate interfacial diffusion effects are shown by the short and long dashed lines, corresponding to the cases shown in Figure 6.5 and 6.6, respectively [50].

changing the boundary condition to the ML transmission line, and the results are also shown in Figures 6.7 and 6.8 (solid lines "b"). These results are in very good

agreement with those obtained by analytical solutions (see Figure 2 of Reference 101), suggesting the verification of the TLM approach.

For the purpose of comparison, the $\bar{C}(y,t)$ versus y/l curves for the case displayed in Figure 6.4 are plotted in Figure 6.7 with the dashed lines, and those in Figures 6.5 and 6.6 are plotted in Figure 6.8 with the short and long dashed lines, respectively. It is interesting to note that all the curves almost exactly coincide at small values of y/l ($y/l \leq 0.15$ for $T = 10^{-3}$ and $y/l \leq 0.25$ for $T = 10^{-2}$) where lattice diffusion in the grains is prevailing, and diverge at large values of y/l owing to the different diffusion paths. In Figure 6.7, $\partial\bar{C}(l, t)/\partial y$ of the dashed lines at the interface is negative, implying a certain amount of material being lost from the film as a result of the diffusion into the substrate. On the other hand, the positive values of $\partial\bar{C}(l,t)/\partial y$ for the dashed lines in Figure 6.8 represent a material build-up in the film from the second source at the interface in spite of the simultaneous substrate diffusion effect. The long dashed lines are situated above the short ones near the interface, because the higher interfacial diffusion coefficient brings about a higher average concentration in those regions. At intermediate y/l values, the results of considering the substrate effect only are similar to the Gilmer-Farrell solutions, while the curves for both interfacial and substrate effects (with the interfacial diffusion playing the dominant role) are found to be located from below the Gilmer-Farrell solutions to below the Whipple solutions, depending on the magnitude of the interfacial diffusion coefficient. Because the surface concentration is fixed and the concentration gradient (hence its flux) along the grain boundary is larger for the system with a higher interfacial diffusion coefficient, the long dashed lines appear at positions below the short ones in Figure 6.8 at intermediate values of y/l. These effects can be better and

intuitively understood by comparing with the previous clearly visible pictures for the concentration profiles (Figures 6.4 - 6.6).

6.4 Summary

Most of the grain-boundary diffusion models and analyses were created between 1950's and 1980's, with the early effort for bulk samples and the later one mainly for thin films. The technological requirements for microelectronic devices have been the prime instigator for these studies over recent years. Although considerable progress has been made for simple idealized problems, understanding of diffusion processes in realistic thin films is far from satisfactory. This is evidenced by the fact that the grain-boundary and interfacial diffusion data are so sparse and less precise even for very important microelectronic materials.

Analytical solutions are normally utilized for the grain-boundary diffusion analyses. These solutions have to assume highly idealized boundary conditions, and questions may arise in determining the validity of the simplifications for real problems. As an effective technique for grain-boundary diffusion modeling, the use of the TLM method is demonstrated for the first time. Concentration distributions are presented as isometric projections and contour plots, taking the substrate and film/substrate interface effects into consideration. All the analyses, including those based on Whipple's model for semi-infinite samples and Gilmer-Farrell's model for idealized thin films, and models for more realistic thin-film systems considering flux into the substrate and film/substrate interface effects, give similar results for the concentration in spatial average at a small distance close to the film surface ($y / l <$ 0.2). In the region near the film backside, the roles of different diffusion mechanisms

are significant. In the central region of the film, the substrate and interface effects result in an average concentration value around the Whipple solutions. It is important to realize, at this stage, that the variation of all the material and geometrical parameters for the composite structure would be very easy to simulate in our TLM model, should the relevant information become available.

Chapter 7

Three-Dimensional Simulation of Impurity Diffusion in Thin-Film Diffusion Barriers

7.1 Introduction

In a solid-state VLSI device, metal-semiconductor and metal-metal interfaces are widespread. Undesired interdiffusion and reactions between these interfaces are often significant sources of device failures. At increased power densities or elevated temperatures, the degradation happens more rapidly. In order to avoid or retard the interdiffusion at metal-semiconductor interfaces and thus enhance device reliability, a diffusion-barrier layer is often interposed [10]-[12]. In device processing, metallic film barriers are normally polycrystalline due to the practical difficulties of realizing single crystalline films. As a result, atomic diffusion along grain boundaries, which normally provide much faster diffusion paths than the lattice diffusion, is an important limiting factor for determining the effectiveness of the thin-film diffusion barriers.

The material in this chapter has been published as Reference [113].

Owing to complexity, the combined lattice and grain-boundary diffusion problems for thin-film systems (B-kinetics) have generally been solved in two spatial dimensions [100], [101], [53], [94], [114]. In addition, the film is often treated as one-grain thick, with a vertical grain boundary or an array of vertical grain boundaries separating different grains laterally. Deposited metal films in reality are composed of a matrix of columnar microstructures that extend through the films [17], but are 3D in nature. The consideration of using a simplified 3D geometrical structure to model the diffusion process is, therefore, worthwhile for gaining some more relevant and meaningful information. A numerical approach is then necessitated, which should be versatile in dealing with the 3D geometry and boundary conditions.

The next section of this chapter describes the 2D and 3D physical models used to simulate impurity diffusion in thin-film diffusion barriers. This is followed by a number of calculated results, illustrating the influence of film geometry and grain-boundary diffusion coefficient with a comparison between the 2D and 3D analyses. Possible implications involved in the diffusion effects are discussed accordingly. Specific examples of Al penetration in TiN, a refractory metallic compound presently employed as a diffusion-barrier material of great interest in microcircuits [13], [115], [116], are given subsequently. The final section contains some concluding comments.

7.2 Physical Models

In Figure 1.2 (see Section 1.2.2 in Chapter 1), a polycrystalline diffusion-barrier layer, U, inserted between materials A and B is shown schematically. This barrier layer can be modeled in two and three dimensions, as shown in Figures 7.1(a) and 7.1(b),

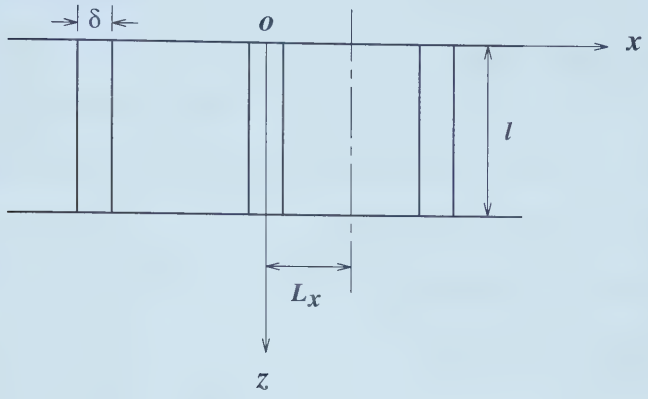

(a)

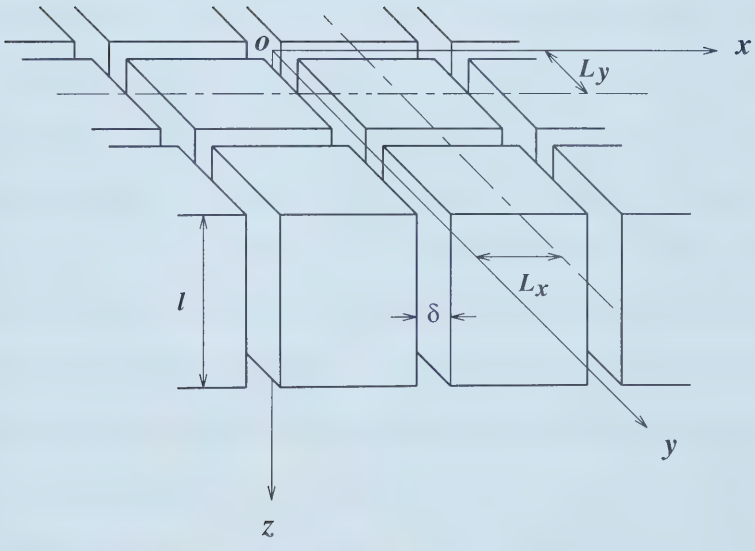

(b)

Figure 7.1 Geometric models for the grain-boundary and lattice diffusion in the thin-film diffusion barrier illustrated by layer U in Figure 1.2.
(a) 2D model, **(b)** 3D model [110].

respectively. The thickness of the barrier layer is assumed to be l in both cases. The grain boundaries are characterized by thin slabs of a uniform width δ. In the 2D case, there is an array of parallel grain boundaries, lying orthogonal to the surface at an average spacing of $2L_x$. In the 3D case, parallelopiped grains of the average spacings in the x and y directions, $2L_x$ and $2L_y$, are separated by an array of square columnar boundaries. Although the structures described are idealized, the major effects can be simulated and the results used as a basis for metallization design and reliability prediction in practical VLSI devices.

Because of the symmetry, only a geometrically periodic structure needs to be considered. This involves an elemental volume with reflective boundaries on its sides where concentration flux is zero. The top surface of the diffusion-barrier layer is attached to a reservoir of the diffusing species. Some of these species (atoms of material A) can diffuse all the way through the barrier layer U, and the subsequent chemical interactions make their back diffusion unlikely. As shown in Chapter 3 (see Sections 3.2 and 3.3), the ML boundary or a "natural" absorbing for the diffusing species in the TLM method provides an interesting termination to the problem space, where the reflection coefficient is set to be zero so that the arriving species at the boundary will not diffuse back. Such a boundary condition is different from a particle sink with a zero or other constant concentration, and varies as a function of position and elapsed diffusion time. It brings about a slightly smaller value at the same position and time when compared with solving the diffusion equations with the bottom of the problem space extended to infinity. The difference in the results is due to the elimination of particle back-diffusion from region B (More detailed discussion about this treatment as a special case of the general mixed boundary condition can be

found in Chapters 3 and 9). The average concentration over the backside surface of the diffusion barrier can then be used as a measure for its efficiency.

7.3 Results and Discussion

For the solutions to be generally valid, it is more convenient to use the following dimensionless variables. The positions along the x, y, and z directions are, respectively, normalized as

$$X = \frac{x}{L_x} \tag{7.1}$$

$$Y = \frac{y}{L_y} \tag{7.2}$$

and

$$Z = \frac{z}{l} \tag{7.3}$$

Similar to Equation (6.3), the reduced diffusion time is defined as

$$T = \frac{D_g t}{l^2} \tag{7.4}$$

where, D_g is the diffusion coefficient of species A in the grains of the diffusion-barrier layer (U), and t is the time. The grain-boundary diffusion coefficient of A in U is denoted as D_b. A normalized value of unity is employed for the constant concentration on the top surface of the diffusion barrier. Unless otherwise indicated for discussing variability of geometrical and/or physical effects, all of the calculated results presented in this chapter are obtained by assuming the plausible representative parameter relationships [100], [50] as follows:

- The ratio between the boundary width and the barrier thickness is $\delta/l = 5\times10^{-3}$;

- The aspect ratio regarding the grain dimensions is $l/L = 4$, where $L = L_x = L_y$; and
- The diffusion coefficient at grain boundaries is four orders of magnitude higher than that within the grains, namely, $D_b/D_g = 10^4$.

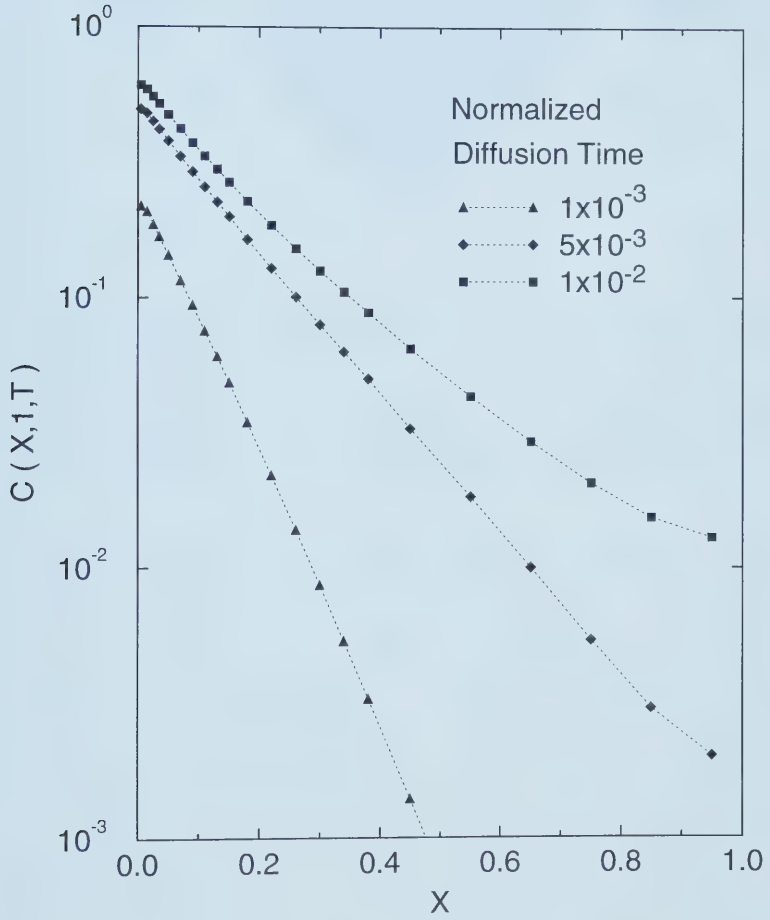

Figure 7.2 2D simulations of the concentration $C(X,1,T)$ vs the normalized distance, X, from the grain boundary into the grain at the backside of the thin-film diffusion barrier ($Z = 1$) and for several values of the normalized diffusion time (T) [113].

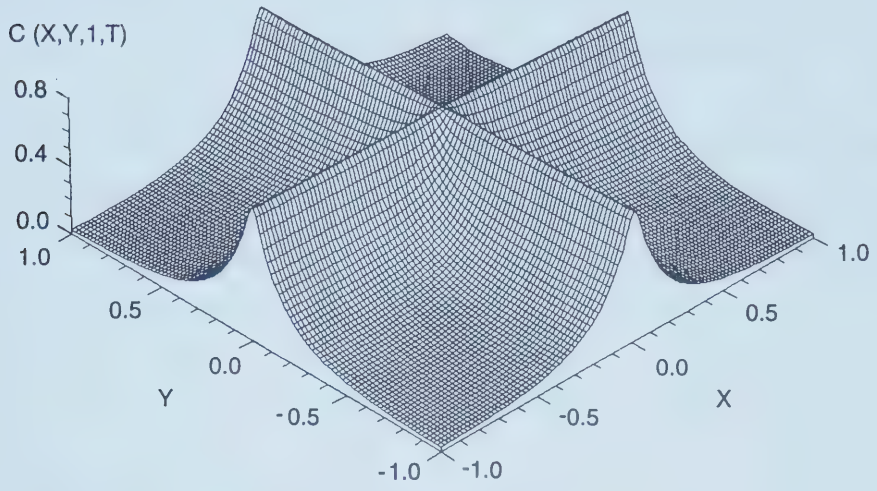

Figure 7.3 3D simulation of the concentration $C(X,Y,1,T)$ vs the normalized distance, X and Y, at the backside of the thin-film diffusion barrier ($Z=1$) and for the normalized diffusion time $T = 1\times10^{-2}$. The center of the plot ($X=Y=0$) corresponds to the intersection of perpendicular grain boundaries [113].

Figure 7.2 displays concentration profiles at the backside of the barrier layer (Z = 1) for several reduced diffusion times using the 2D simulations. For most of the diffusion region, an exponential decay of concentration against the distance away from the grain boundary is clearly seen. However, the 2D calculation is commensurate with an infinite grain length along the y direction. Real grains should have approximately equal size while looking from different angles in the x-y plane. This means that the 2D simulations could underestimate the lateral diffusion effects to a large degree. In order to obtain an adequate estimate, a 3D calculation is performed and a representative result is shown in Figure 7.3 as an isometric projection. Acting as fast diffusion paths, the grain boundaries effectively spread out the concentration with

an identical maximum value (~0.8), for a normalized diffusion time of 1×10^{-2}. This concentration is found to be 25% greater than the corresponding 2D result.

The comparison of the 2D and 3D simulations can be further illustrated in terms of an average impurity concentration $\bar{C}(Z,T)$ versus the normalized diffusion distance along the vertical direction Z. For the 2D case, this average concentration for a section parallel to the surface can be defined as

$$\bar{C}_{2D}(Z,T) = \int_0^1 C(X,Z,T)\,dX \tag{7.5}$$

and for the 3D case, it becomes

$$\bar{C}_{3D}(Z,T) = \int_0^1 \int_0^1 C(X,Y,Z,T)\,dY\,dX \tag{7.6}$$

Shown in Figure 7.4 are the calculated results. First, the discrepancy between the 2D and 3D predictions is significant. Second, one may notice that the barrier layer manifests itself like a semi-infinite sample during the initial period of diffusion time, and that the absorbing effects for particles at the backside of the barrier layer come into play gradually as the time elapses. All this can be identified based on the shapes of the $\bar{C}(Z,T)$ vs Z curves, as similarly discussed in Chapter 6 [50] (also, see Reference 100). Additional simulations indicate that the 3D curves shown in Figure 7.4 may also be duplicated by the 2D analyses with an appropriately enlarged grain-boundary diffusion coefficient — more evidence of underestimation by the 2D approach. However, it is important to emphasize that this has to be restricted to averaged concentrations with some "equivalent" quantities for fitting in the real ones. Other useful results such as that shown in Figure 7.3 can only be achieved using the

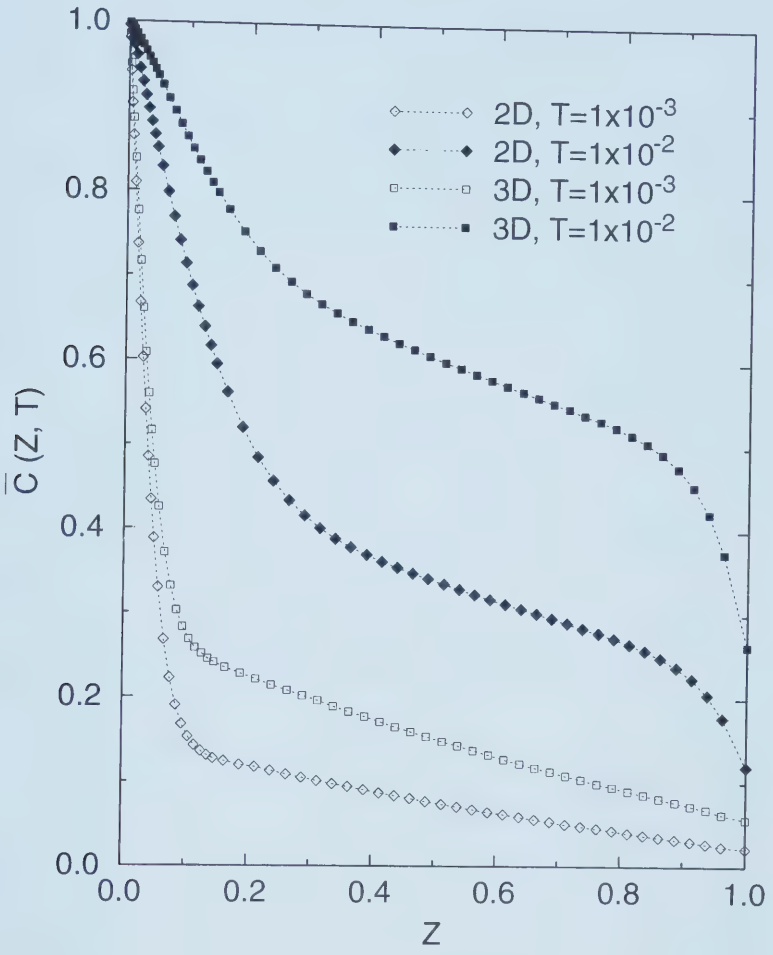

Figure 7.4 Comparison of the 2D and 3D simulations of the average concentration $\bar{C}(Z,T)$ vs the normalized vertical distance Z for two values of the reduced diffusion time (T) [113].

3D calculation.

Since 2D process simulations are the major approach nowadays, a direct 3D/2D comparison is shown in Figure 7.5(a) to quantify the underestimation by 2D solutions and generate a scaling factor for the average concentration as defined above. In order

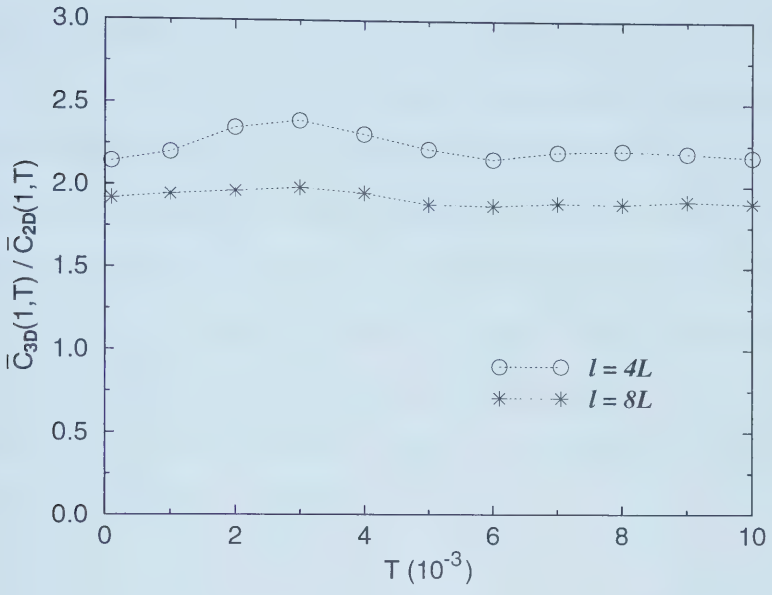

(a)

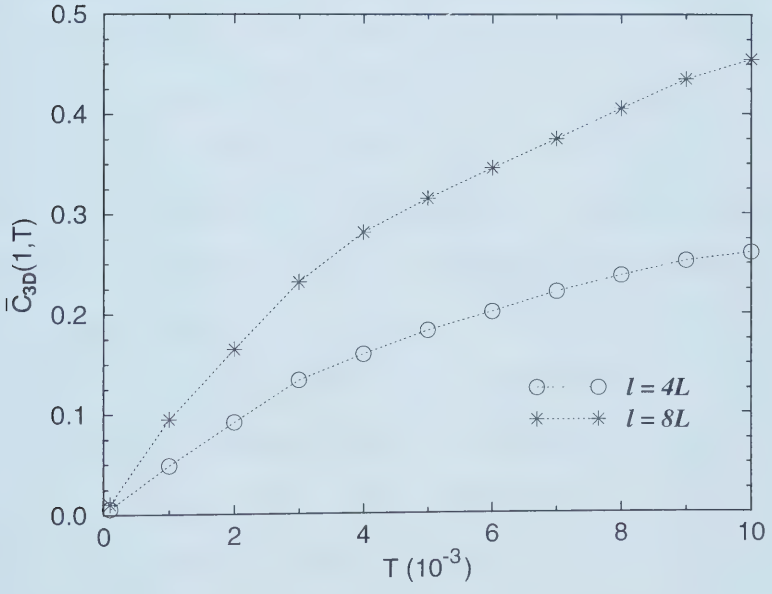

(b)

Figure 7.5 The average concentration at the backside of the diffusion barrier $\bar{C}(1,T)$ as a function of the normalized diffusion time, T, for two values of the relationship between l and L. **(a)** 3D/2D scaling factor, **(b)** 3D simulation results [113].

to facilitate the evaluation of the effectiveness of thin-film diffusion barriers, the results are presented by plotting the average concentrations at the backside of the barriers ($Z = 1$) as a function of the normalized diffusion time, *i.e.*, $\bar{C}_{3D}(1,T)/\bar{C}_{2D}(1,T)$ vs T, for several different geometrical structures. The 2D results consistently underestimate the average concentration by factors of approximately 2.2 and 1.9 for the ratio l/L of 4 and 8, respectively. Shown in Figure 7.5(b) are the 3D simulation results over the same range of times and grain size structures. A constant scaling factor with diffusion time is expected due to the difference in grain-boundary densities between the 2D and 3D models.

As an example of an application of the present model, I use the 3D curves shown in Figure 7.5(b) to obtain a qualitative idea about the efficiency of a particular barrier material of general interest, TiN, for preventing Al penetration in metallization systems of Si devices. Without this barrier layer, intermixing of Al and Si would spike shallow junctions and degrade circuit performance. It should be noted that TiN layers fabricated by different processing technology may have distinct physical structures and phase content, and exhibit a certain varied permeability to Si or Al atoms. Recent measurements [117], [118] indicated that the grain-boundary coefficients of Si and Al diffusion in reactively evaporated TiN films with columnar microstructures are almost identical. The average grain size of these films is approximately 20 nm, corresponding to the magnitude of $2L$ in our model. Grain-boundary diffusion of Al in the TiN films was characterized as [118]

$$D_b\,(\text{Al in TiN}) = 3\times10^{-18}\exp\left(-\frac{30\ \text{kJ mol}^{-1}}{RT}\right)\ \text{m}^2\text{s}^{-1} \tag{7.7}$$

where, R is the universal gas constant (8.31 $JK^{-1}mol^{-1}$), and T is the temperature in kelvins. If grain-boundary diffusion is regarded as the prime limiting factor of the diffusion barrier and Equation (7.7) can be extrapolated to a normal device operating temperature of 350K, then according to Figure 7.5(a) for thin TiN layers with a thickness of 40 nm ($l=4L$), the normalized diffusion times at which the average Al concentration at the backside of the TiN layer reaches 5% and 10% of the concentration at the top surface are, respectively, 1×10^{-3} and 2×10^{-3}. The corresponding real-life times are then determined by Equation (7.4) and the ratio D_b/D_g (= 10^4) to be roughly five and ten years. If the thickness of TiN layers were increased to 80 nm and the grain-boundary width remained unchanging so that $l=8L$ and $\delta / l = 2.5\times10^{-3}$, then the curves shown in Figure 7.5(b) would yield doubled values for the time. These results confirm that TiN films can serve as effective diffusion barriers and that a thickness on the order of tens of nanometers is sufficient for the purpose.

Figure 7.6 illustrates the average concentration at the backside of the diffusion barrier $\bar{C}(1,T)$ as a function of the boundary to matrix diffusivity D_b/D_g. In general, the value of D_b is very much greater than that of D_g. However, one must consider the pronounced effects of "stuffed" barriers [12]. In this case, some species of either host excess or foreign impurity atoms decorating the grain boundaries may result in a much reduced boundary diffusivity. It can be seen from Figure 7.6 that there is a decrease of more than two orders of magnitude in $\bar{C}(1,T)$ when D_b is varied to change the ratio D_b/D_g from 10^4 to 10^2.

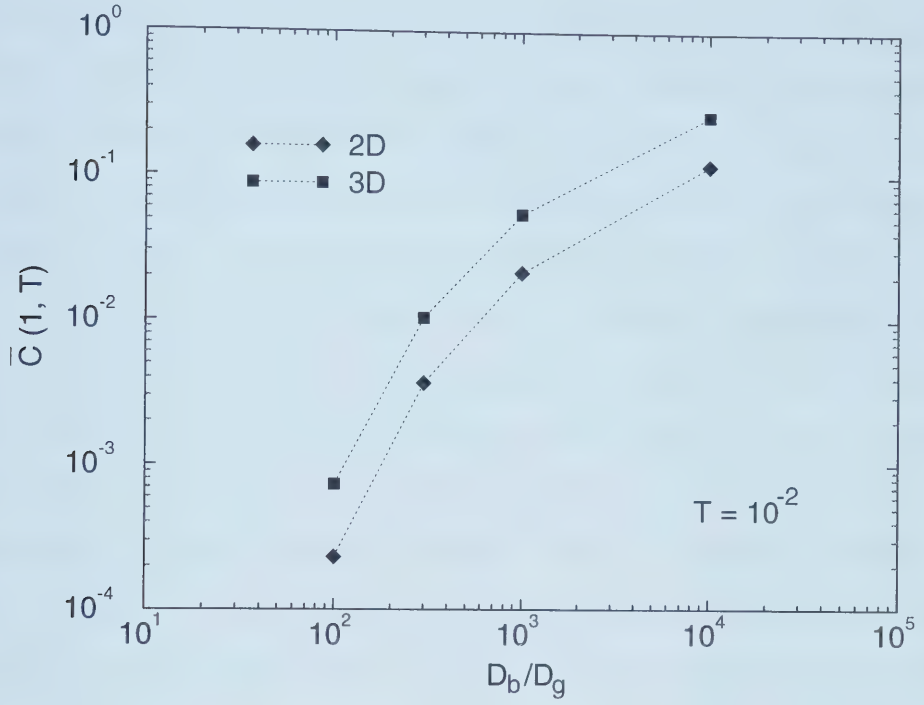

Figure 7.6 The average concentration at the backside of the diffusion barrier $\bar{C}(1,T)$ vs the ratio between grain-boundary and grain coefficients, D_b/D_g. This demonstrates the effectiveness of "stuffing" the grain boundary with excess or other atoms to lower D_b [113].

In this section, I have compared calculated results based on the 2D and 3D simulations. The 3D geometric structure employed is a logical and straightforward extension from the idealized 2D model in common use. Nevertheless, the full 3D computation performed here is not complicated too much by virtue of the use of TLM numerical approach. As final remarks, I give further examination of the validity of the simplified 3D modeling assumption. Fairly general and very computer-intensive Monte Carlo solutions for grain-boundary diffusion in semi-infinite samples have been reported by Hodge [119]. He compared three different geometries of grain

boundary with the same characteristic dimension, *i.e.*, parallel planar, square columnar, and randomly occurring boundaries. After a relatively long period of diffusion time, the 3D columnar and random boundaries were found to exhibit essentially very similar concentration profiles which deviated from the profile for the 2D slabs. Of course, the complexity of the microstructure increases for the random-boundary situation, but it brings about primarily an increase in rapid diffusion paths (grain boundaries) not normal to the surface source as a result of the same average grain diameter used. In other words, diffusing species cannot find downward paths much more readily, and thus this change in the microstructure does not influence substantially the overall vertical concentration profiles. Consequently, simple 3D square columnar boundaries might be considered as an acceptable approximation especially for polycrystalline thin films that are characterized by the columnar microstructure.

7.4 Conclusions

In summary, the 3D phenomenological solutions have been presented for impurity penetration in thin-film diffusion barrier layers with coupled grain-boundary and lattice diffusion. A parallel comparison with the 2D analysis demonstrates clearly the 3D nature of the problem. To simplify the matter, a square columnar microstructure is suggested and used in the present investigation for thin-film diffusion barriers to simulate the major effects. Impurity concentrations are illustrated as a function of position and time, and the influence of the ratio of boundary to lattice diffusion coefficients is also qualitatively studied. As for the average concentration at the backside of diffusion barriers, approximately a factor of two difference between the

2D and 3D simulation results is found over an interesting range of times and grain size structures. From the point of view of grain-boundary diffusion, TiN films with a thickness in the range of tens of nanometers are shown to be effective barriers to prevent Al-Si intermixing in Si microelectronic devices for several years of operation.

Chapter 8

Simulation of Electromigration in Thin-Film Diffusion Barriers

8.1 Introduction

Electromigration is one of the major reliability concerns regarding metallic film interconnections used in VLSI circuits. It is a mass transport process induced by current flow through the conductive polycrystalline films, and grain-boundary diffusion is generally considered the predominant mechanism responsible for the atom movement [6]. Extensive experimental and theoretical research effort [121]-[125] has been put into the lateral electromigration phenomenon, in which the associated electric field is along the direction of the interconnection track. On the other hand, "vertical" electromigration can also occur when the current passage is perpendicular to the deposited metal films. This is especially of importance for multilevel interconnection structures, where there are numerous topographic features such as vias connecting metal lines of adjacent levels as well as contacts to the semiconductor material. It has been shown that the electromigration induced depletion

---

The material in this chapter has been published as Reference [120].

of Cu in thin Al-Cu films along one particular vertical direction could be a source of via failures [126].

In VLSI interconnections, thin-film diffusion-barrier layers are routinely employed to prevent the direct contact and intermixing of two reactive materials, *e.g.*, Al and Si [12]. However, the insertion of the diffusion barrier in between does not eliminate the driving forces for diffusion—the concentration gradient and current flow. These two factors may sometimes strengthen each other and result in a decrease in the efficiency of the diffusion barrier. Such an effect would be further exacerbated under the condition of a large current density and a high operating temperature.

In this chapter, I will develop a physical model of electromigration in thin-film diffusion barriers and show the scenario quantitatively by using the TLM approach. Specifically, a parallel comparison of the 2D and 3D calculations with respect to impurity concentrations as a function of position and time will be illustrated.

8.2 Model Formulation

Diffusion barriers in practical device metallizations are polycrystalline thin films, and a simplified 2D model with parallel planar grain boundaries is generally utilized to simulate the primary effects of diffusion processes. In Chapter 7, I have demonstrated the use of a 3D rectangular columnar microstructure for the same purpose. The 2D and 3D models and the relevant geometrical parameters have been shown, respectively, in Figures 7.1(a) and 7.1(b). Owing to the symmetry of these periodically repetitive structures, the volume of material that has to be considered in

the simulation is reduced to $0 \le x \le L_x$ and $0 \le z \le l$ for the 2D model and $0 \le x \le L_x$, $0 \le y \le L_y$ and $0 \le z \le l$ for the 3D model.

The governing equations for the present investigation can be written as [127] - [129]

$$\frac{\partial C_b}{\partial t} = D_b \nabla^2 C_b + v_b \frac{\partial C_b}{\partial z} \tag{8.1}$$

and

$$\frac{\partial C_g}{\partial t} = D_g \nabla^2 C_g + v_g \frac{\partial C_g}{\partial z} \tag{8.2}$$

where C is the concentration of source atoms, t the time, D the diffusivity, v the ion drift velocity, and ∇^2 the 2D or 3D Laplace operator. The subscripts b and g denote parameters associated with the boundary and the interior of the grain, respectively. Notice that the electromigration drift terms appear only in the direction of current flow, or along the vertical z-axis. v_b is given by [127]

$$v_b = \frac{D_b}{kT} | Z^* | e \rho j \tag{8.3}$$

where Z^* is the effective valence, e the electric charge, ρ the film resistivity, j the current density, and kT has its usual meaning of thermal energy. If Z^* and ρ are comparable in grain boundary and bulk, then the ratio of the ion velocity at the boundary and within the grain is equal to that of the corresponding diffusivities, viz.

$$\frac{v_b}{v_g} = \frac{D_b}{D_g} \tag{8.4}$$

As in Chapter 7, the concentration and its flux are assumed to be continuous at the grain boundary/bulk interfaces. Also, the boundary conditions include a constant

source of atoms at $z = 0$, symmetrical sides of zero concentration flux and absorbing bottom surface at $z = l$. As a result, the concentration at the backside will vary with the elapsed diffusion time, and the value averaged over the entire bottom surface can be used as a figure of merit for evaluating the diffusion barrier efficiency.

As mentioned in Section 3.8, a voltage-controlled current generator (I_m) can be attached to the fundamental TLM diffusion node to model the drift effect [43], [52] according to

$$ {}_k I_m = g_m \cdot {}_{k-1}\Delta V_z \tag{8.5}$$

where the potential (concentration) difference across the node in the z-direction at the (k-1)th time-stepping iteration (${}_{k-1}\Delta V_z$) is used to generate the current at the kth iteration (${}_k I_m$). This simple explicit calculation can be considered appropriate for a linear or a weakly non-linear system. The transconductance g_m is given by

$$ g_m = 3vC/\Delta l \tag{8.6}$$

where the capacitance of the transmission line (C) is determined based on an advantageous way of constructing the TLM network components [50]

$$ C = \Delta x \, \Delta y \, \Delta z / 3 \tag{8.7}$$

and the elemental length Δl can be treated as an average value for a 3D irregular mesh

$$ \Delta l = (\Delta x + \Delta y + \Delta z) / 3 \tag{8.8}$$

Therefore, the magnitude of g_m may be varied for different nodes, and is given by

$$ g_m = 3v \frac{\Delta x \, \Delta y \, \Delta z}{\Delta x + \Delta y + \Delta z} \tag{8.9}$$

The inclusion of these new equations in the standard TLM scattering and connection algorithm will give the solution to Equations (8.1) and (8.2), and other properties of

the TLM method being used, *e.g.*, the automatic time-stepping capability [31], [32], will not be affected.

8.3 Results and Discussion

For the convenience of calculation and discussion, the dimensionless quantities defined by Equations (7.1) - (7.4) are used. A particular parameter for characterizing the electromigration effect is given by

$$\theta = \frac{\delta v_b}{(D_b D_g)^{1/2}} \tag{8.12}$$

The parameter θ is essentially a ratio of the normalized grain-boundary electromigration $v_b t / d_b$ to the normalized distance of bulk leakage d_g / δ [note that $d = (Dt)^{1/2}$ is the diffusion length]; thus, θ can be interpreted as the normalized extent of electromigration. Calculated concentration is also normalized with respect to the reservoir constant of the diffusing species on the top surface, where the value after normalization is unity. For the purpose of demonstrating and analyzing the grain-boundary diffusion and electromigration effects, the same plausible parameter relationships as in Chapter 7 are assumed: i) $\delta/l = 5\times10^{-3}$, ii) $L_x = L_y = L$ and $l/L = 4$, and iii) $D_b/D_g = 10^4$. Additionally, a value of $\theta = 1.0$ would correspond to a current density in the range of 10^6 A/cm^2 for some typical thin-film materials [127].

In Figure 8.1(a), representative concentration profiles at the backside of the barrier layer ($Z = 1$) by using the 2D model are drawn with $\theta = 0$, 0.5 and 1.0 at a reduced diffusion time of 1×10^{-3}. The concentrations decay in an exponential-like manner against the distance away from the grain boundary for both situations without ($\theta = 0$)

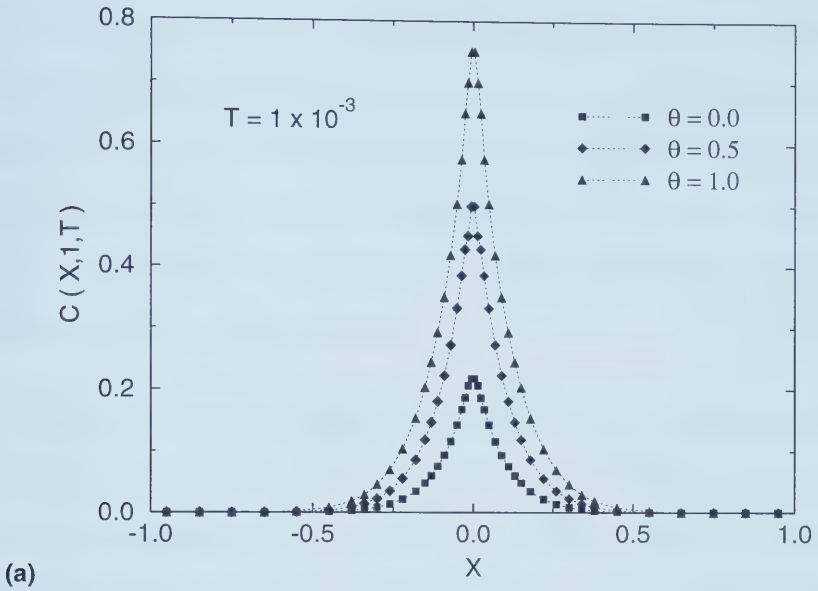

(a)

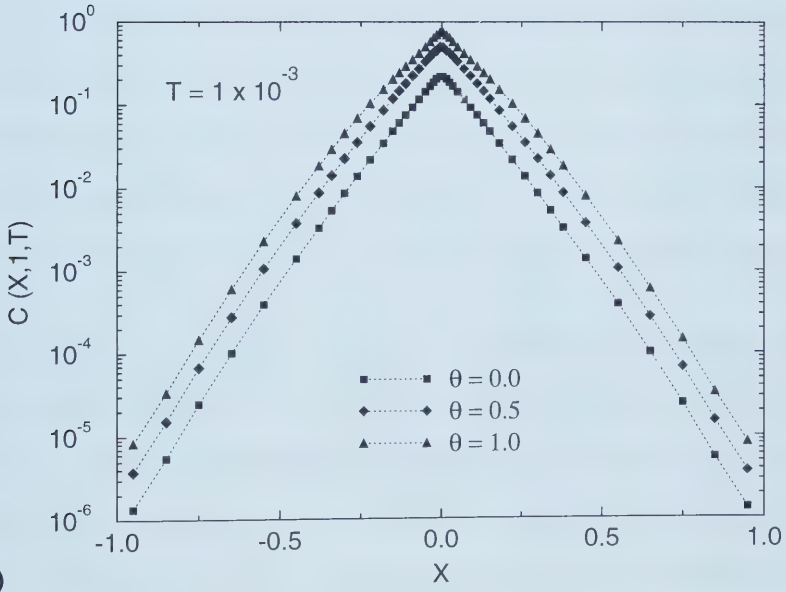

(b)

Figure 8.1 2D simulations of the concentration $C\,(X,1,T)$ vs the normalized distance, X, from the grain boundary into the grain at the backside of the thin-film diffusion barrier ($Z = 1$) and for several values of θ. **(a)** Linear scale; **(b)** semi-logarithmic scale [120].

and with ($\theta \neq 0$) the electromigration driving force. Atom leakage into the bulk from the grain boundary orthogonally is not influenced by the driving force parallel to the boundary. However, the driving force effectively enhances the diffusivity and shifts the overall concentration profiles to larger values [129] in the vertical direction, which can be seen more clearly in Figure 8.1(b) when the same concentration profiles are plotted in a semi-logarithmic scale.

In order to remove the unrealistic 2D assumption of an infinite grain length along the *y*-direction, 3D calculations are performed and visualized in Figure 8.2. Similar qualitative behaviors as described above are also exhibited. However, in terms of the maximum concentration at the boundary, the 2D simulations are underestimated by 23% for the case of $\theta = 0$ and 48% for $\theta = 0.5$ due to the neglect of more rapid paths for grain-boundary diffusion and electromigration. These isometric projections have been plotted using a graphics package which assumes regularly spaced data points. Therefore, the grid displayed in the diagram does not necessarily correspond to that used for the numerical solution. Also, the serrated ridges are plotting artifact.

The evaluation of the barrier efficiency and further comparison of the 2D and 3D simulations can be done according to an average concentration $\bar{C}(Z,T)$, defined by Equations (7.5) and (7.6). Illustrated in Figures 8.3 and 8.4 are, respectively, the calculated results of $\bar{C}_{2D}(Z,T)$ and $\bar{C}_{3D}(Z,T)$ along the main material transport direction *Z*. Once again, there is a pronounced discrepancy between the 2D and 3D predictions. Notice also the curves for different θ values coincide within the position $Z \leq 0.1$ in both the 2D and 3D simulations, and separate more and more apparently afterwards. This suggests that the atomic diffusion is predominant near the top surface

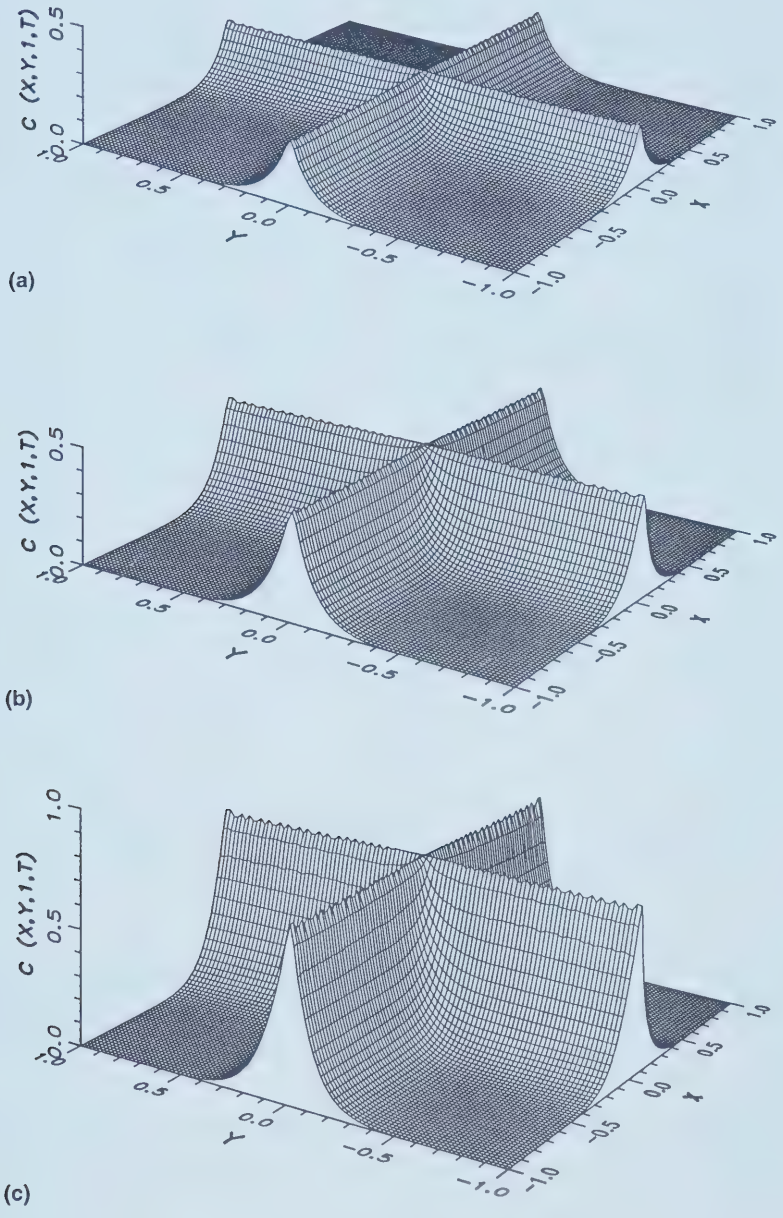

Figure 8.2 3D simulation of the concentration $C(X,Y,1,T)$ vs the normalized distance, X and Y, at the backside of the thin-film diffusion barrier ($Z = 1$) and for the normalized diffusion time $T = 1\times10^{-3}$. The center of the plot ($X = Y = 0$) corresponds to the intersection of perpendicular grain boundaries.

(a) $\theta = 0$, **(b)** $\theta = 0.25$, **(c)** $\theta = 0.5$ [120].

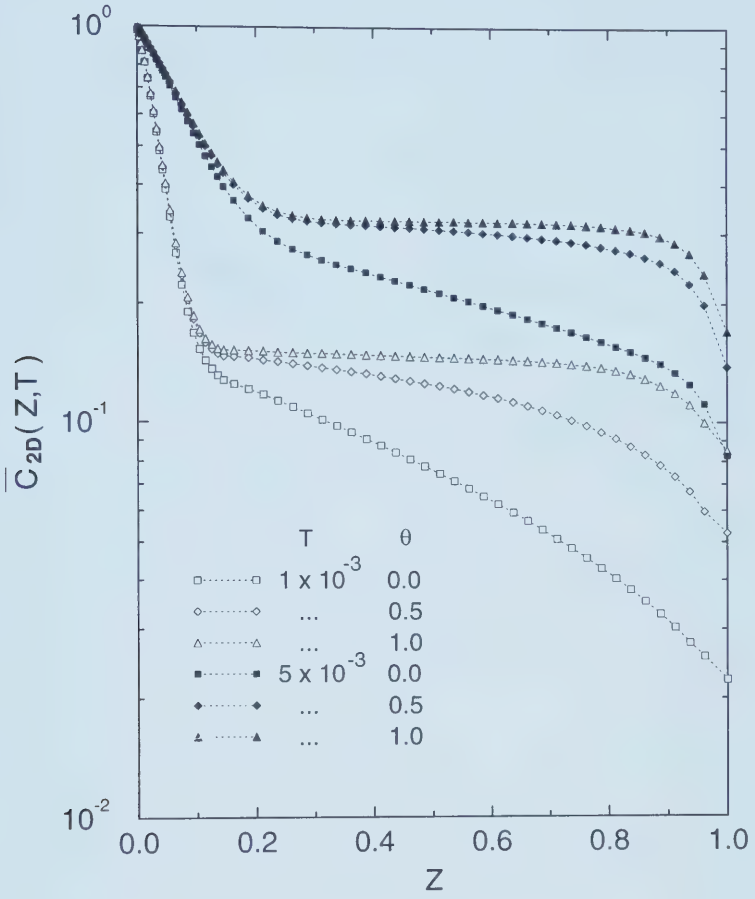

Figure 8.3 2D simulation of the average concentration $\overline{C}(Z,T)$ vs the normalized vertical distance Z for several values of θ and reduced diffusion time T [120].

due to the steep local concentration gradients, and that the electromigration drift then becomes more significant deeper in the barrier. Finally, the concentrations evidently decrease approaching the second surface as a consequence of the backside absorbing condition.

Figure 8.5(a) displays the 3D simulation results of the average concentration at the backside of the diffusion barrier ($Z = 1$) over an interesting range of diffusion times

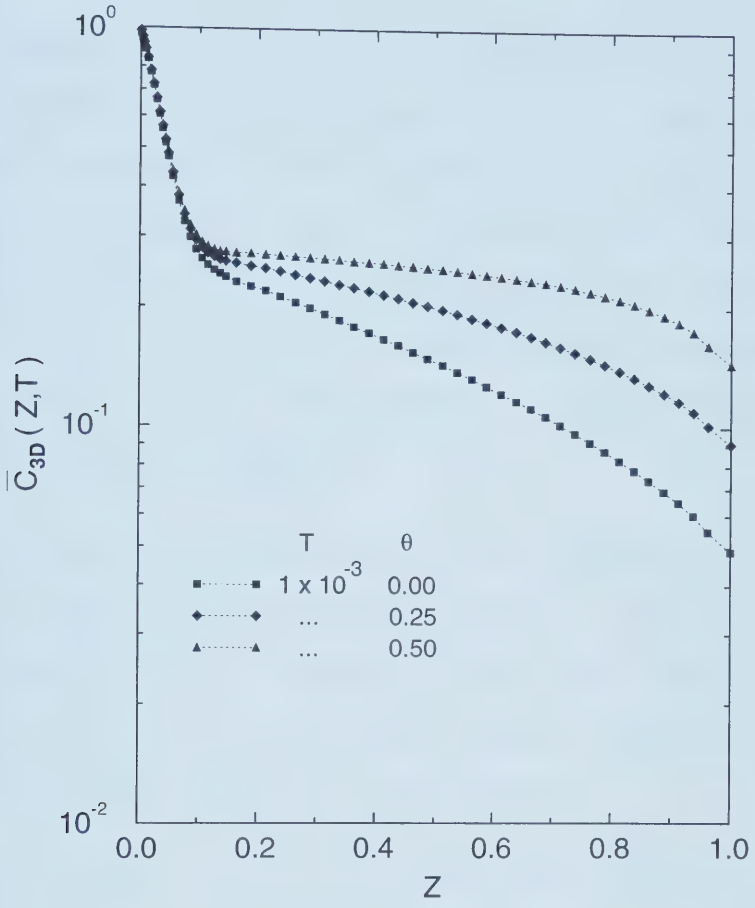

Figure 8.4 3D simulation of the average concentration $\bar{C}(Z,T)$ vs the normalized vertical distance Z for several values of θ and reduced diffusion time T [120].

for a number of θ values. The normalized diffusion times at which the average impurity penetration to the backside plane reaches 5% and 10% of the upper surface value are found to be 1×10^{-3} and 2×10^{-3}, respectively, in the absence of the electromigration driving force ($\theta = 0$). These values are decreased to 4×10^{-4} and 7×10^{-4}, respectively, for the case of $\theta = 0.5$. The corresponding experimental life-times will be material dependent. To obtain a rough idea of the intuitive meaning of the

numbers, I use TiN as an example for the diffusion barriers. Assume that Equation (7.7) for thin TiN layers with an average grain size of 20 nm ($2L$) can be extrapolated to a normal device operating temperature of 350K. According to Figure 8.5(a), the real-life times for $\theta = 0$ after reaching the 5% and 10% average penetration can be determined by Equation (7.4) and the ratio D_b/D_g ($= 10^4$) as approximately five and ten years. However, the times for $\theta = 0.5$ (corresponding to a grain-boundary ion migrating velocity $v_b \cong 2.5\times10^{-13}$ cm/sec in the present example) will be decreased to two and three and half years, respectively.

Since 2D process simulations remain today's major approach, a direct 3D/2D comparison is shown in Figure 8.5(b) in order to generate a scaling factor for the simulation with the same grain dimensions. This figure shows that the 2D results consistently underestimate the average backside concentration by factors of about 2.1 and 2.6 for $\theta = 0$ and 0.5, respectively, for a large timescale.

A final comment on reversing the electromigration driving force is now in order. It is also possible that electric current flows through a metallization topography in the direction opposite to the concentration gradient of the diffusing species, which will alleviate the combination effect and presumably result in an improved efficiency for retarding the diffusion of the species. Additional 3D simulations have confirmed this effect. The average impurity penetration to the backside of the barrier layer was reduced by about 40% at a normalized diffusion time of 1×10^{-3} when $\theta = -0.25$. Nevertheless, more attention should be paid to the reinforcement of the two factors responsible for the rapid atomic grain-boundary displacement, as it represents a worse situation for functioning diffusion barriers.

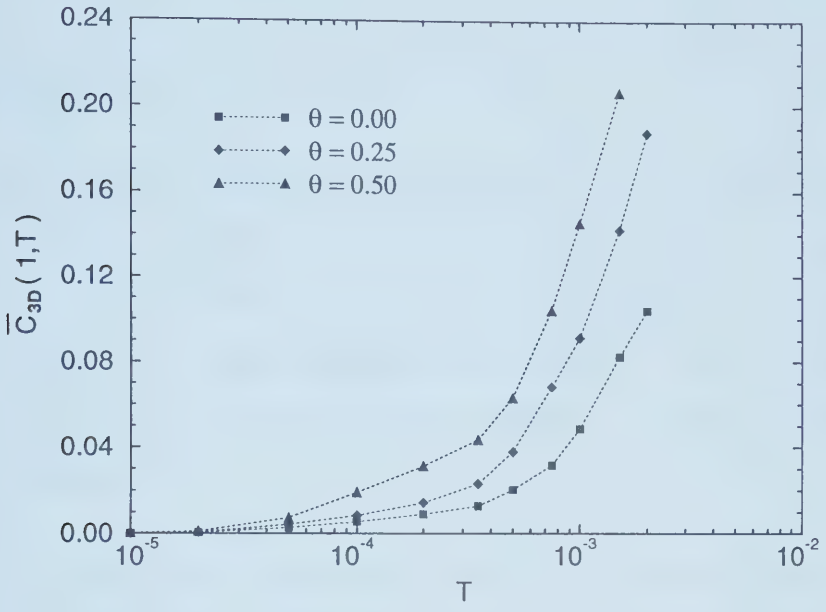

(a)

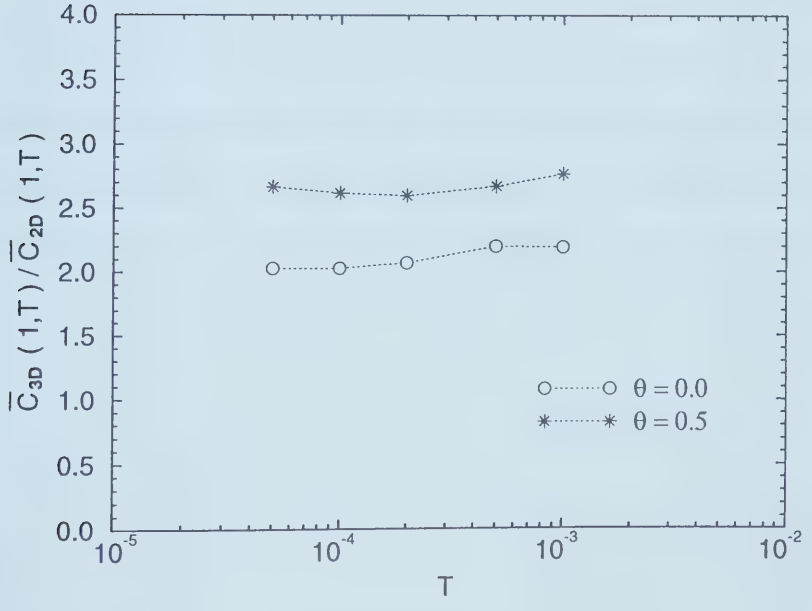

(b)

Figure 8.5 The average concentration at the backside of the diffusion barrier $\bar{C}(1,T)$ as a function of the normalized diffusion time, T, for several values of θ.
(a) 3D simulation results, **(b)** 3D/2D scaling factor [120].

8.4 Summary

I have calculated the simultaneous grain-boundary diffusion and electromigration in thin-film diffusion barriers for microelectronic devices. Besides the concentration gradient, a further diffusion driving force originating from the current flow perpendicular to the deposited barrier films was shown, in several representative computer simulations, to enhance the impurity diffusion and decrease the efficiency of the diffusion barrier.

A multidimensional TLM approach for modeling diffusion and drift effects with a variable mesh structure was used and validated in the simulation. The 3D calculation was based on the consideration of finite lateral and vertical barrier configurations, and the underestimation of the 2D model was then assessed quantitatively by examining material transport through the diffusion paths present in the barrier layer. Normalized parameters were used to generalize the solution, and a specific example of TiN material was given in accordance with the available data on grain-boundary diffusion.

Chapter 9

Efficiency Evaluation of Diffusion Barriers with Microstructural Details

9.1 Introduction

To date, the need for an improved understanding of impurity diffusion in polycrystalline thin-film materials has been increasingly important. This is especially true for the design, manufacturing and operation of VLSI circuits, where conductive films deposited over a variety of different topographical features are required to form appropriate interconnections and contacts to electrically-active semiconductor regions.

Due to the complexity of the actual situation, highly idealized models [97]-[103], [53] have been utilized for analytically characterizing the grain-boundary diffusion phenomena. In such models, all grain boundaries were assumed perpendicular to a flat surface and extend either to infinity or all the way through the film. In addition, all the grains were assumed to have the same regular dimension. Subsequently developed Monte Carlo calculations [131], [132] for diffusion barrier evaluation assumed, still

---

The material in this chapter has been published as References [49] and [130].

artificially, alternative brick-wall and more disordered patterns with multiple vertical grains. Although major effects involved in the diffusion process can be investigated based on these models, an advanced prediction more pertinent to thin-film growth technology for microelectronic materials of interest is undoubtedly necessary with the trend of further miniaturization of VLSI devices.

In this chapter, I will develop a new TLM grain-boundary diffusion model capable of using realistic microstructures obtained from a Monte Carlo thin-film growth simulator. As a result, all the above-mentioned idealized assumptions can be removed. The TLM numerical method will be developed with an emphasis on the various boundary conditions and the approach for evaluating the barrier efficiency. Following the description of the modeling method, I will present some fundamental simulation results and discuss the possible related implications. Particular application examples of TiN as a useful diffusion barrier material will also be demonstrated.

9.2 Modeling Method

As a starting point of the simulation, a Monte Carlo film-growth simulator called GROFILMS (GRain Oriented FILm Microstructure Simulator [133], see 9.3) is used to generate a process dependent grain structure. This microstructural information provides a sound basis for the investigation of impurity atom diffusion through grain boundaries and the evaluation of thin-film diffusion-barrier efficiency.

At typical device operating temperatures, grain-boundary diffusion dominates the transport processes. It is generally acceptable and convenient to assume that the lattice diffusion is completely frozen out. This corresponds to type C of the normally

designated three regimes of diffusion kinetics for polycrystalline materials [111] (see 6.2). Type C kinetics are in conformity with the term grain-boundary diffusion in the most literal sense, although the term is often used less restrictively. From the point of view of numerical modeling, computational resources could largely be reduced for these kinetics even with a refined mesh as only the space confined to grain boundaries needs to be considered, along with appropriate boundary/bulk and other interface terminations. Such irregularly shaped grain-boundary geometries dictate the use of a numerical approach accounting for the associated diffusion processes. This involves, in my TLM model, a 2D square-grid structure with a spatial resolution in the order of an average grain-boundary width of approximately 10 Å [112]. A series of integer-number pairs, (x_1,y_1), (x_2,y_2), ···, (x_n,y_n), are used for indicating each individual grain-boundary location. The simulated film microstructure given as a series of line segments in GROFILMS can be readily converted into such a representation of grain boundaries.

Clearly, we must pay special attention to the treatment of various boundary conditions that play an essential role in our grain-boundary diffusion modeling. For a 2D orthogonal TLM mesh, a normal elemental cell can share one common side with four nearest neighbors. In order to identify the grain-boundary geometrical relationships between adjacent elements and the corresponding physical boundary conditions, different values are assigned to a shape-factor array for each (x, y) position. Table 9.1 [130] gives an example of this factor for the cells with two nearest grain-boundary neighbors. A numbering convention used in Table 9.1 is shown in Figure 9.1. As the constant source is located at the top of the diffusion barrier, the diffusion process will proceed downwards primarily. Thus, the negative x and y

orthogonal directions are denoted as 1 and 3, while the positive directions as 2 and 4. In this way, all the possible cases, including the triple and quadruple points, can be taken into account. For the cells attached to the top surface, the constant-source boundary is employed. On the other hand, the general mixed condition is applied to the backside. The OC insulating condition prohibits a voltage pulse from moving into the bulk. The connecting direction is made to be consistent with the scattering direction of a voltage pulse, so that the diffusion process can proceed from the surface source to the backside of the barrier layer. Given the considerations specified above, the approach should be able to tackle the complex impurity diffusion through a grain-boundary network with arbitrary thin-film microstructures.

TABLE 9.1 Elemental Cells with Two Nearest Grain-Boundary Neighbors

Shape factor	2.1	2.2	2.3	2.4	2.5	2.6
Cell Shape						
Connecting Direction	1, 2	1, 3	1, 4	2, 3	2, 4	3, 4
Insulating Direction	3, 4	2, 4	2, 3	1, 4	1, 3	1, 2

9.3 Results and Discussion

To justify the validity of this grain-boundary diffusion model on the basis of physical interpretation and computational feasibility before examining realistic and complicated structures, I have employed a simplified test microstructure of thin-

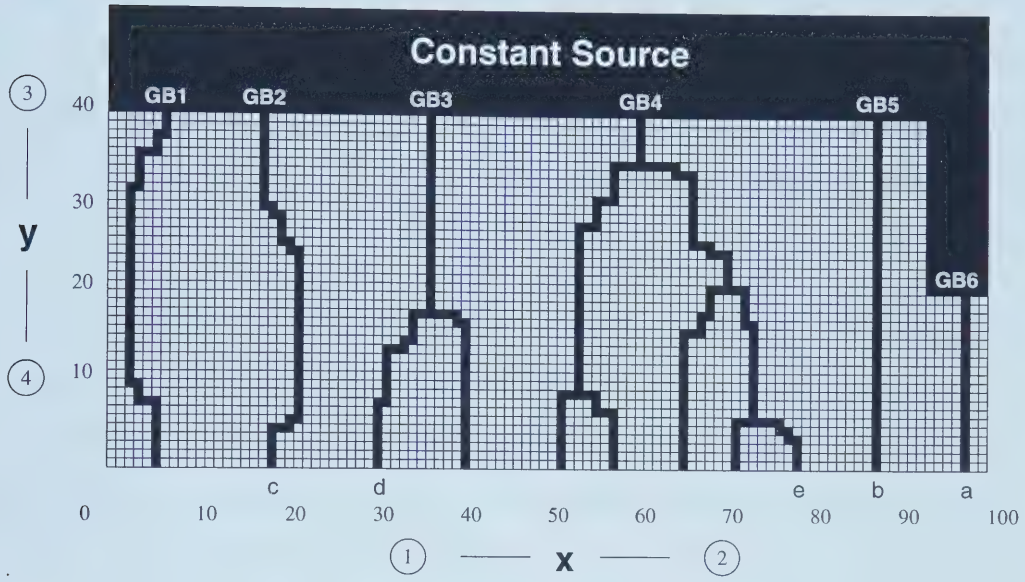

Figure 9.1 A simplified test microstructure of diffusion barriers to demonstrate and validate the modeling method. There are six separate grain boundaries (GB1 - GB6) with different configurations in the film. Also, five specific positions at the lower surface (a) - (e) are used for further analysis. The circled numbers denote the orthogonal directions [130].

film diffusion barriers with six grain boundaries (GB1-GB6) as shown in Figure 9.1. Its corresponding data file is manually created for the purpose of generating a functioning shape-factor array. There are several distinctive features in this structure. The first two grain boundaries on the left-hand side, GB1 and GB2, exhibit different circuitous arrangements to join the elemental cells but possess an identical effective diffusion distance. As a result, the concentrations near the exit ends of the two paths are expected to be exactly the same at any elapsed diffusion time. As for GB3, there are two branches originating from a triple point. Furthermore, GB4 is intentionally

designed as a configuration with multiple triple points. Finally, both GB5 and GB6 are shaped from top straight down to the bottom, while the diffusion distance of the latter is halved with respect to the former. The aim of the presence of GB5 and GB6 in the structure is twofold: to serve as references for comparison and to demonstrate that the top surface needs not necessarily be flat.

The test structure described above can further be employed for establishing the approach of evaluating the diffusion barrier efficiency. Again, the implications with the boundary conditions of the problem are considerable. As shown in Figure 9.1, the top surface is in contact with a reservoir of the diffusing species, which is normalized to unity. The boundary condition at the backside of the diffusion barrier ($y = 0$) can be expressed in a general form [53] with the impurity out-diffusion flux (F) from the barrier layer

$$F = - D_b \frac{\partial C(x,0,t)}{\partial y} = \alpha C(x,0,t) \tag{9.1a}$$

or

$$D_b \frac{\partial C(x,0,t)}{\partial y} + \alpha C(x,0,t) = 0 \tag{9.1b}$$

where, $C(x,y,t)$ is the impurity concentration as a function of position and time, D_b is the grain-boundary diffusion coefficient, and α is a proportionality coefficient.

In general, this boundary condition allows for at least three different interpretations:

- From a thermodynamics point of view, the difference between concentrations in the problem space and outside drives a matter flux through the surface.

- Analogous to Ohm's law, the surface represents a resistance for the matter flux, leading to a concentration difference.
- The boundary condition itself is a continuity equation: the first term is the diffusion flux, which is proportional to the product of the diffusion coefficient and concentration gradient; while the second term is the convection flux, proportional to the product of the boundary concentration and out-diffusion velocity.

These interpretations are not contradictory, but supplementary to one another. Several important cases can be discussed in accordance with the TLM terminology:

(a) $\alpha = 0$. This means a zero out-diffusion flux or a totally inert substrate. It is commensurate with the OC boundary in the TLM method. Evidently, if such a boundary condition could be used for the present analysis, a diffusion-barrier layer would not be necessary.

(b) $\alpha \rightarrow \infty$. This requires the concentration at the backside surface to approach zero, $C(x, 0, t) \rightarrow 0$, so that the flux F becomes a finite value which depends solely upon the concentration gradient for a given material. This complete sink condition can be realized by the SC boundary in the TLM method.

(c) $0 < \alpha < \infty$. Unlike the above two extremities, this intermediate partial sink situation has a wide range for the flux, and the α-value itself could even be varied with backside concentration at different times. The TLM treatment of this general diffusion flux boundary condition [48] has been developed and discussed in Section 3.3.

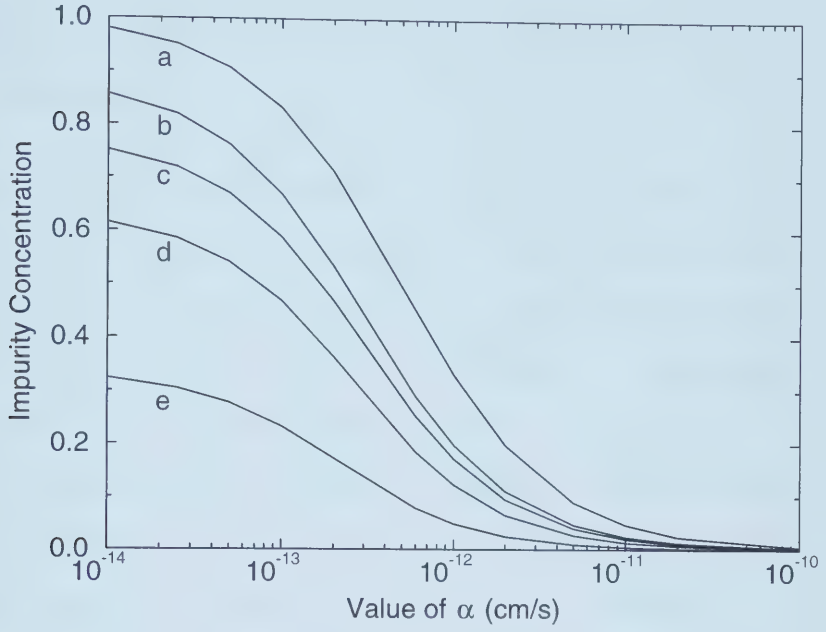

Figure 9.2 Steady-state impurity concentration at several different positions as indicated in Figure 9.1 vs the value of α [130]

Now I choose TiN as an example to show a number of fundamental results for the proposed structure, because TiN has attracted considerable interest over the years as a diffusion-barrier material in VLSI metallization systems. If Equation (7.7) for the grain-boundary diffusion of Al in reactively evaporated TiN films can be extrapolated to a normal device operating temperature of 350 K, then one can obtain that $D_b \approx 1\times 10^{-18}$ cm^2s^{-1}. Figure 9.2 shows the effect of varying the value of α over several orders of magnitude at steady state. A smaller α means a more inert substrate, while a larger α leads to a decreased concentration due to substrate interactions. As discussed in Section 3.3, the ML absorbing boundary in the TLM method is a special case of the general boundary condition (Equation (9.1)). Due to the lack of data for the Al-Si

interaction rate, the ML boundary could be a plausible approximation in light of its physical meaning.

Figure 9.3 shows the concentration variation with the diffusion time at several representative positions on the backside of the barrier layer, corresponding to those labeled "a" - "e" in Figure 9.1. Apparently, the impurity penetration to the backside of the barrier layer gradually increases with time until the concentration reaches a steady-state value. The time constant is longer for a more tortuous diffusion path down to the bottom. However, different positions are eventually found to have an identical α-value of 1.0×10^{-11} cm·s^{-1}. The parameter α has a dimension of velocity. It depends mainly on the diffusivity of Al in TiN, and characterizes how fast the Al atoms can move away from the backside surface of TiN upon emerging from its grain boundaries and simultaneously arriving at the underlying Si substrate. As indicated in Equation (9.1), the diffusion flux F, or the quantity of atoms "walking" into the Si substrate per unit area and time, can be available by multiplying $C(x,0,t)$ by α at various x positions. For example, 1% penetration of Al to the backside would result in a diffusion flux of $F = \alpha \times n_{Al} \times 1\% = 6.03 \times 10^{9}$ atoms·cm^{-2}s^{-1} (where n_{Al} is the atomic density of Al, being equal to 6.03×10^{22} atoms·cm^{-3}). This serves as a measure of the effectiveness of the TiN diffusion-barrier layer. Furthermore, an integration for the flux with respect to the operating time will give an estimation of Al atom density per unit area in the Si substrate over that period of time as the curve of $C(x,0,t)$ vs t has been obtained in the calculation.

Figure 9.4 shows the concentration on the backside of the barrier layer as a function of the lateral position at $t = 1.5 \times 10^{7}$ s, which is almost at steady state. As

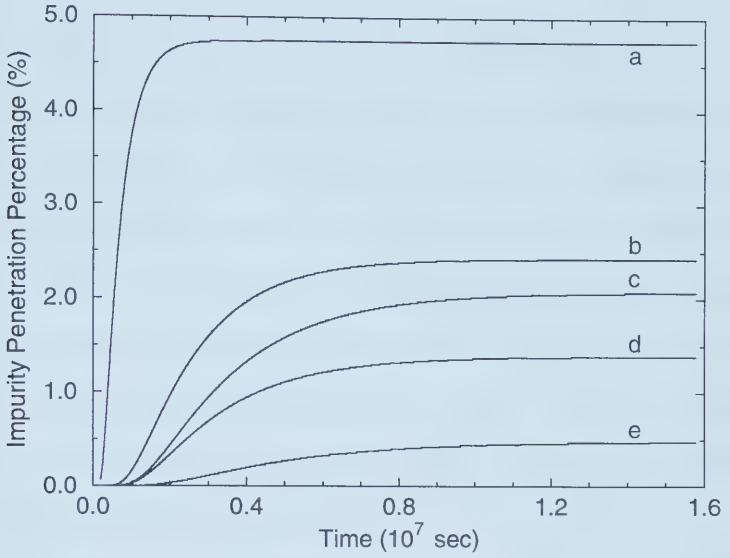

Figure 9.3 Impurity penetration percentage with respect to the constant concentration at the upper surface of the diffusion barrier as a function of time at several different positions, corresponding to those indicated in Figure 9.1 [49].

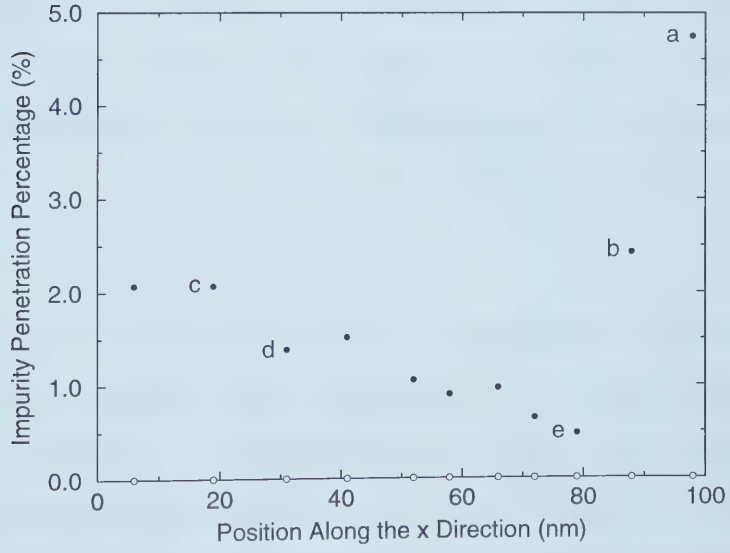

Figure 9.4 Impurity penetration percentage with respect to the constant concentration at the upper surface of the diffusion barrier as a function of position approximately at steady state for the simplified structure shown in Figure 9.1 [49].

anticipated, the first two grain boundaries on the left-hand side have the same final diffusion behavior, while the last two on the right-hand side have a strict twofold relationship in terms of the concentration. Evidently, a winding path can effectively slow down the diffusion process, and grain-boundary branches can split the concentration value compared with the situation of the straight direct grain boundary. It should be noted that neither a free outside surface for diffusing species (as conceived in the analysis of the measurement of grain-boundary diffusivity at low temperatures by the surface accumulation method [102]) nor an average TiN/Si interfacial diffusivity is assumed in our study. The data points displayed in Figure 9.4 are discrete for separate grain-boundary positions touching the bottom surface of the diffusion-barrier layer. For this reason, I have marked the corresponding coordinates at the x-axis using the small opaque circles. In addition, it is worthwhile to note that grain-boundary traps and blockages may play a role in stopping impurity diffusion through a diffusion barrier [132]. These effects may be simulated by specifying the grain-boundary diffusion coefficient as a function of position in the present model. A constant diffusion coefficient is currently being used, which would generate worst case results.

After testing the grain-boundary diffusion modeling method with the simplified geometry, this approach is now implemented on a more realistic thin-film microstructure generated by GROFILMS [133]. Different from a number of other thin-film process simulation algorithms based on particle aggregation [134]-[137] or surface profiling [138], [139], GROFILMS depicts the surface topography and film microstructure by describing each grain within the film through a string of line segments. The evolution of film growth is governed by the incorporation of interfacial

and surface energy calculations, surface diffusion effects and the geometrical considerations of a ballistic depositing flux. Films generated using GROFILMS are the combined result of the above processes as well as nucleation, substrate wetting, grain boundary grooving, columnar growth and grain competition. GROFILMS provides both surface profiles and microstructure details of the resultant thin films, which can also be used for further analyses.

Figure 9.5(a) shows a simulated diffusion-barrier layer over a via with an aspect ratio (height-to-width) of 1.5 and an 85°-angled sidewalls. This type of structure is generally employed for a contact in VLSI metallization systems, and is formed by plasma etching through the SiO_2 dielectric layer. An Al layer will be deposited on the top of the diffusion barrier for providing a proper electrical connection. The present analysis, however, only focuses on the diffusion-barrier layer between the Al and the underlying semiconductor or contact material. The simulated film in that region consists of many densely packed columnar grains. The smaller grains close to the substrate have been shadowed by larger ones and hence have not continued to grow [140]. Although the film deposition time during simulation has been constrained to a certain degree, the gradual increase in the film thickness from the corners to the center is still readily visible. I choose to focus on the bottom left-hand side part, which is shown within the rectangular box in Figure 9.5(a) and highlighted with the labeled x and y coordinates in Figure 9.5(b), to illustrate the simulation results for the grain-boundary diffusion and diffusion-barrier efficiency evaluation. This representation is consistent with the conducting film microstructure that may be obtained experimentally by physical vapor deposition (PVD) techniques [17]. Figure 9.6 displays a scanning electron microscope (SEM) photograph of a real film deposited

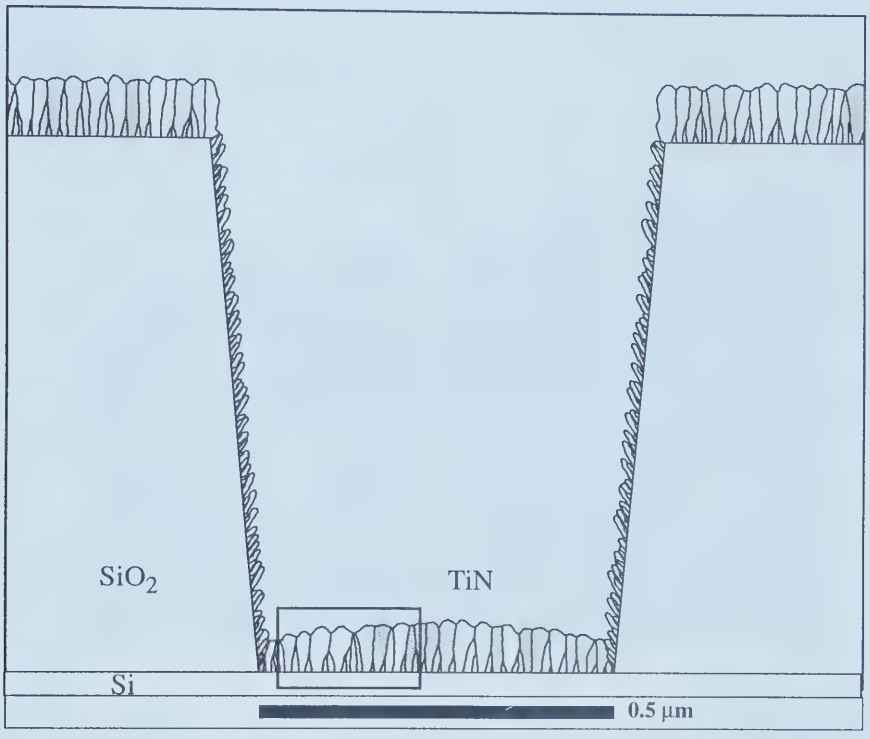

(a)

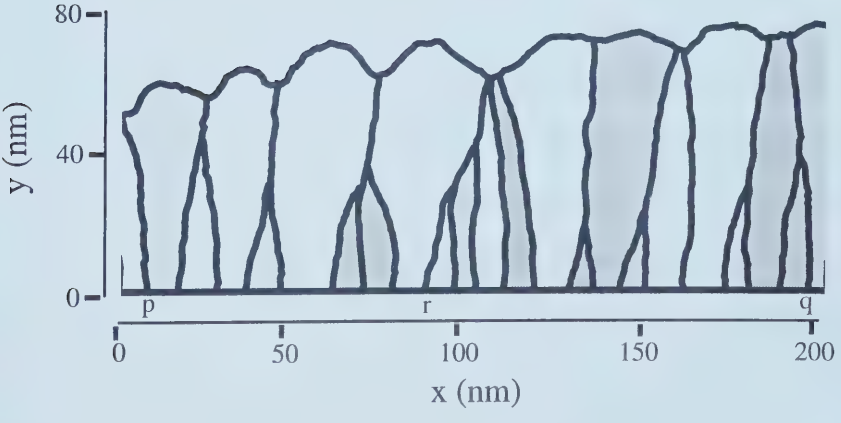

(b)

Figure 9.5 **(a)** GROFILMS-generated thin-film diffusion barrier over a 0.5-μm via in integrated circuit metallizations. **(b)** The region enclosed by the rectangular box in (a) for TLM grain-boundary diffusion simulation [49].

by magnetron sputtering.

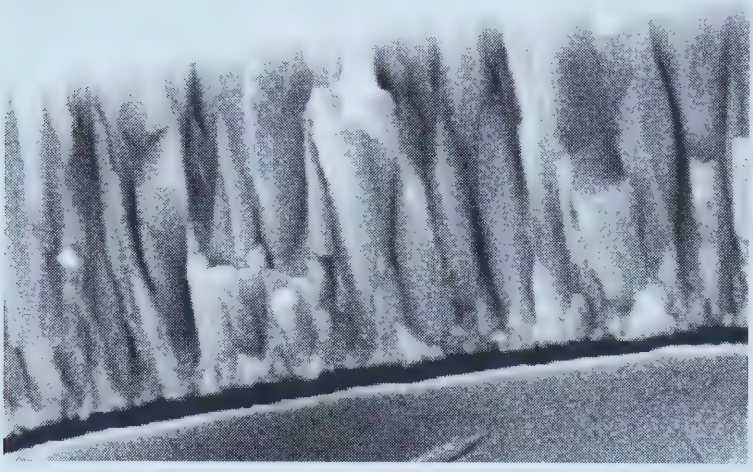

Figure 9.6 An SEM photograph of TiW films, showing the columnar microstructure (Courtesy of R. N. Tait, Alberta Microelectronic Centre, Canada).

As mentioned earlier, the graphical representation of the thin film by GROFILMS can be superimposed onto an orthogonal mesh suitable for the current TLM diffusion study. The GROFILMS-generated data file for the structure shown in Figure 9.5(b) is placed onto a 200×80 mesh (200-nm wide by 80-nm thick). The displayed thickness in the range of 50 to 80 nm is typical of TiN diffusion barriers considered for submicron silicon VLSI metallizations [115]. Three specific positions at the left-most side (with no triple point), the right-most side (with one triple point) and in the middle (with multiple triple points) are chosen and referred to as "p", "q", and "r", respectively. Similar to the analysis presented above, the curves of concentration vs diffusion time particularly for the three indicated locations are shown in Figure 9.7,

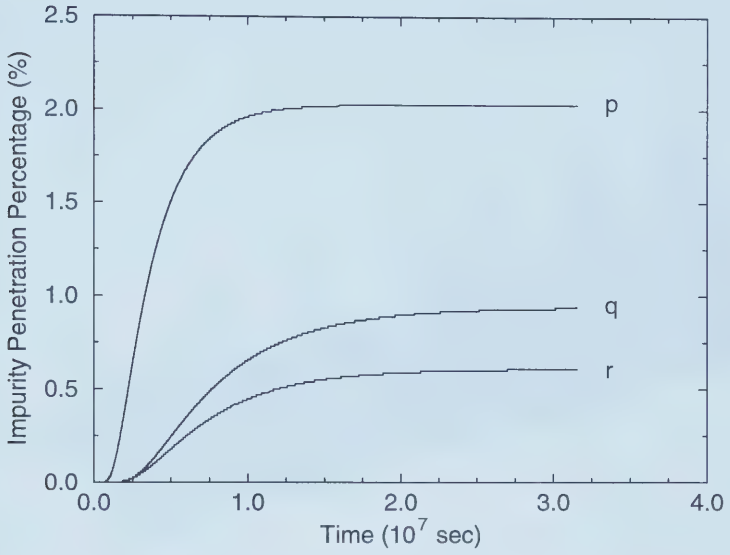

Figure 9.7 Impurity penetration percentage with respect to the constant concentration at the upper surface of the diffusion barrier as a function of time at several different positions, corresponding to those indicated in Figure 9.5 [49].

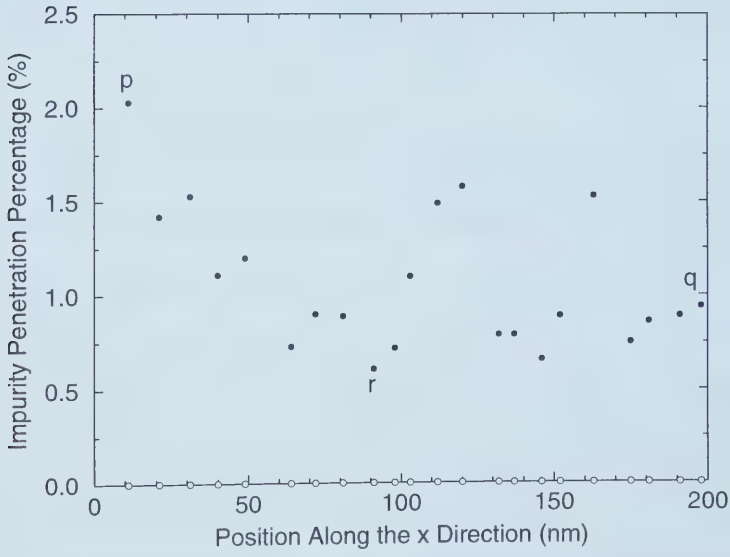

Figure 9.8 Impurity penetration percentage with respect to the constant concentration at the upper surface of the diffusion barrier as a function of position approximately at steady state for the microstructure shown in Figure 9.5 [49].

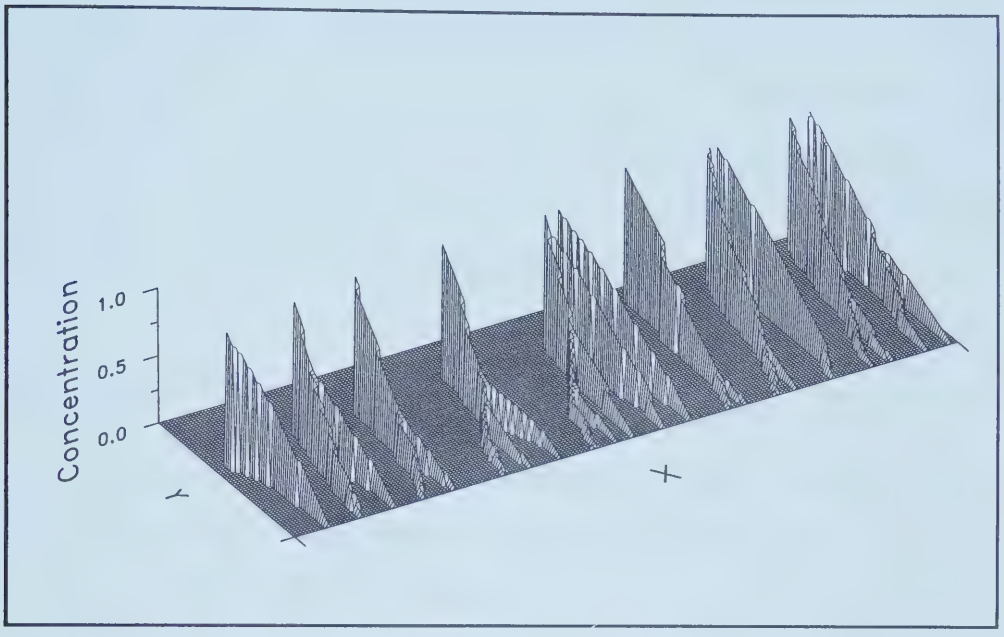

Figure 9.9 Isometric view of the concentration distribution in equilibrium for the microstructure shown in Figure 9.5 [49].

while the concentration variation with the x-coordinate on the barrier-layer backside is shown in Figure 9.8. Owing to an increased thickness of TiN films when compared with the previous simplified structure, the time constant becomes longer and the impurity permeation to the backside of the barrier layer is reduced. However, the equilibrium transfer rate α at the interface between the diffusion barrier and the substrate is unchanged. In Figure 9.8, the diffusion-barrier efficiency is clearly shown to depend quite substantially on the thin-film microstructure. In fact, variations by a factor of more than three in the impurity penetration can be seen over very short distances across the diffusion barrier structure. This can have important consequences

for practical thin-film diffusion barriers, although a precise criterion for device failures based on the impurity penetration percentage is yet to be investigated. Figure 9.9 shows the ultimate concentration visualization in the steady state using the same grid frame as that used for the numerical solution. This gives a comprehensive view of the solution to the problem over the entire 2D space under consideration.

9.4 Concluding Comments

In this chapter I have demonstrated that a more detailed picture with respect to grain-boundary diffusion and the effectiveness of thin-film diffusion barriers can be gained through undertaking a suitable numerical modeling exercise. The barrier effectiveness has been shown to vary significantly with local film structure. The ability to model barrier performance based upon microstructural details may be a valuable tool for optimizing deposition processes and resultant thin-film diffusion barriers. The combined Monte Carlo film-growth and TLM diffusion simulation can be aimed at a particular geometry and process technology of interest for given materials. The TLM method has proved to be versatile in dealing with this class of problems. However, it is of vital importance to treat various boundary conditions with caution. For problems requiring large spatial domains, the computation time should not be excessive as only the space of a grain-boundary network is concerned with type C diffusion kinetics. It is straightforward to extend the present approach to other realistic situations, such as a multi-level stacked structure consisting of different materials. In Chapters 7 and 8, I have shown the 3D TLM simulation of impurity diffusion and electromigration in thin-film diffusion barriers with regular geometries. The present analysis could also

be performed fully in three dimensions if the corresponding film representation were available.

Chapter 10

Concluding Remarks

With the continuing trend of VLSI and beyond, device structures are becoming increasingly sophisticated. Multicomponent metallization is now at the heart of many current integrated circuits. An objective for the research and development of metallization in microelectronic devices is to design-in reliability rather than to try and achieve it by substantial work in a production environment, which would be both expensive and time consuming. Also, it is often very difficult, if not impossible, to perform direct measurement experimentally in detail due to the small interconnect feature sizes. Therefore, modeling and simulation of various processes and degradation modes during both manufacturing and operation can play an essential role in the design, analysis, prediction and optimization of metallization structures. Unlimited to these direct applications, a powerful information handling tool may be able to provide insight into the new physical contexts and to aid in the formulation of ideas and points of view for the analysis of device performance and reliability.

Thermal and atomic diffusion phenomena have been recognized as fundamental and important reliability issues for the development of VLSI devices. With the reduction of interconnect dimension, the increase of current density and correlated Joule heating can raise the conductor temperature. Metallization overheating manifests itself as a remarkable instantaneous failure mechanism, such as thermal burnout occurring in fuse or antifuse like devices. Also, a higher temperature can accelarate atomic diffusion and mass transport through thin films, which is important in controlling the rate at which a degradation reaction proceeds. In terms of metallization, the maximum current density imposed by electromigration tolerance is considered as one of the significant limiting factors for further integration [141], and also a figure-of-merit for selecting interconnect alternatives [20]. Calculated results [142] predict that lowering the operation temperature moderately is very effective to relax the limit for electromigration reliability from the point of view of interconnection scaling.

In this thesis, thermal and particle diffusion phenomena (as described by the diffusion equation and the diffusion/drift equation) in VLSI metallization structures have been investigated successfully by an alternative and useful approach, the TLM method. The extension of this highly flexible method to more general situations (including some particular algorithms) is still at an early stage of development. The TLM method may find its way into a wider realm of application in microelectronic devices in the future. Solutions for the differential equations governing evolution of mechanical stresses [124], [143], [144] and electromigration behavior under time-dependent current stresses [54], [147] are such examples. Beyond the problems associated with metallization systems, the TLM method of solving the general

continuity transport equation in semiconductor devices has been developed theoretically [43], [52] but the implementation to a real device structure has yet to be done.

* * *

This thesis is written based primarily on ten papers that have been completed since I entered the Electrical Engineering Department at the University of Alberta as a graduate student in early 1993. Among these papers, seven [49], [50], [67], [82], [83], [113], [120] were published in five different international journals, one [130] in a conference proceedings, one [48] is now in press and a further one [145] has been submitted for publication in another international journal. Some relevant material contained in the articles which I authored and co-authored [18], [29], [31], [32], [47], [51], [52], [64] prior to the present Ph.D. program are also mentioned in the thesis whenever necessary. The main originality concerned in the work may be summarized briefly as follows:

Thermal diffusion in VLSI metallization structures

- 3D steady-state thermal analysis of high density triple-level interconnect structures and a comparison with that of single-level structures [67]
- The influence of interlevel and passivation dielectrics on thermal performance [67], [82], [83]
- Transient simulation of single-level and multilevel thin-film interconnect failure caused by high current pulses, especially the effects of thermal capacity of passivation materials [82], [83]

Particle diffusion in VLSI metallization structures

- Grain-boundary diffusion phenomena have been studied by utilizing the TLM method for the first time, comparisons with other available solutions were made, and extensions of including substrate and interface effects illustrated [50]
- 3D simulation of impurity diffusion in thin-film diffusion barriers [113]
- Simulation of "vertical" electromigration in thin-film diffusion barriers [120]
- Grain-boundary diffusion modeling and efficiency evaluation of thin-film diffusion barriers considering microstructural details [49], [130]

The TLM numerical method

- A general expression of boundary condition in TLM diffusion modeling [145], [48].
- The analysis and use of an error parameter (m) in TLM diffusion modeling [29], [31], [32], [50], [52], [64], [67], [82], [113], [120]
- General expressions for time step transformation [32], [31]
- Extension of solution of the diffusion/drift equation to multiple dimensions [52], [120], [48]
- Treatments of boundary conditions for grain-boundary diffusion in thin films [49], [50], [130]
- A comparative study of two TLM networks for diffusion modeling [51]

It is hoped that this thesis will serve as a ground work for further in-depth investigations with respect to diffusion and diffusion-related processes in microelectronic devices.

Appendix

Further Comments on a General Boundary Condition in TLM Diffusion Modeling

It is well known that TLM diffusion modelling is convenient and versatile in dealing with a variety of boundary conditions. This is evidenced by the electrical SC (reflection coefficient $\rho = -1$) and OC ($\rho = 1$) terminations of the linking transmission line in a boundary cell, corresponding to the continuous Dirichlet and Neumann conditions, respectively. In chapter 3, the treatment of the general (Robin) boundary condition

$$D\frac{\partial \Phi}{\partial x} + \alpha \Phi \Big|_{x=0} = 0 \tag{A.1}$$

has been illustrated in an approximate way by the use of a controlled current source [48]. Meanwhile, the ML boundary ($\rho = 0$) was shown numerically to be a special

---

This appendix is a result of some additional thought that was given after the first draft of the thesis had been completed. The material in this appendix has been submitted for publication as Reference [145].

case of the Robin condition [48]. In this appendix, I will give an explicit expression of the ML boundary condition through a more consistent treatment with the fundamental operation of a TLM routine.

Following the derivation by Al-Zeben, Saleh and Al-Omar [43], we have

$$D\frac{\partial \Phi}{\partial x} = -\frac{IZ\Delta x}{\Delta t} \tag{A.2}$$

where I is the electrical current. Therefore, Equation (A.1) can be written as

$$-\frac{IZ\Delta x}{\Delta t} + \alpha V_B = 0 \tag{A.3}$$

where V_B is the voltage at the $x = 0$ boundary. This equation suggests an equivalent boundary resistor† given by

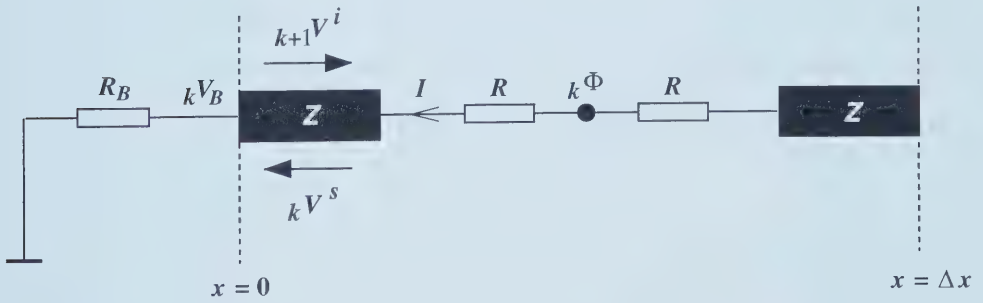

Figure A.1 Termination of a TLM network at $x = 0$ with a boundary resistor R_B.

† The original idea of using the boundary resistor was due to P. B. Johns and S. H. Pulko [44]. Similar treatment was also performed by Dr. A. H. M. Saleh [146].

$$R_B = \frac{V_B}{I} = \frac{Z\Delta x}{\alpha \Delta t} \tag{A.4}$$

By referring to Figure 1, we can see that the incident pulse from the boundary of interest (x=0) at the adjacent node for the (k+1)th iteration will be determined by the pulse scattered from the opposite direction at the kth iteration and a reflection coefficient due to the impedance discontinuity, namely,

$${}_{k+1}V^i = \rho_k V^s = \frac{R_B - Z}{R_B + Z}{}_kV^s = \frac{\Delta x - \alpha \Delta t}{\Delta x + \alpha \Delta t}{}_kV^s \tag{A.5}$$

As indicated in chapter 3 [48], the boundary voltage ${}_kV_B$ is needed in the calculation of the drift term in a diffusion-drift equation. It can be given by

$${}_kV_B = {}_kV^s + {}_{k+1}V^i = \frac{2\Delta x}{\Delta x + \alpha \Delta t}{}_kV^s \tag{A.6}$$

Equations (A.5) and (A.6) along with the fundamental TLM scattering algorithm are sufficient for a diffusion or diffusion-drift problem involving the Robin boundary condition. Important special cases include: i) $\alpha \to \infty$, which is equivalent to a short-circuit boundary where ${}_{k+1}V^i = -{}_kV^s$ and ${}_kV_B = 0$. ii) $\alpha = 0$, which is equivalent to an open-circuit boundary where ${}_{k+1}V^i = {}_kV^s$ and ${}_kV_B = 2{}_kV^s$.

Finally, I clarify the special situation of the matched-load boundary that corresponds to ρ=0. According to Equation (A.5), this simply requires

$$\alpha = \frac{\Delta x}{\Delta t} \tag{A.7}$$

Equation (7) means that the diffusing species can move an elemental distance away from the boundary within an elemental time. It is this particular velocity that leads to the distinctive features of ${}_{k+1}V^i = 0$ and ${}_kV_B = {}_kV^s$. The numerical observation presented

in chapter 3 [48] actually serves as an adequate confirmation example of Equation (A.7), in which case the atoms diffuse from a constant source through grain boundaries present in a thin film and reach its backside where the boundary condition is given by Equation (A.1). The specific values of $\Delta x = 1 \times 10^{-6}$ cm, $\Delta t = 25$ sec and $\alpha = 4 \times 10^{-8}$ cm/sec that satisfy Equation (A.7) were found to represent the matched-load boundary condition precisely.

In summary, the general diffusion boundary condition as given by Equation (A.1) can be represented by a voltage reflection coefficient due to the discontinuity between the transmission-line impedance and an attached boundary resistance. This reflection coefficient can be expressed in terms of α, the parameter characterizing the out-diffusion mobility of the diffusing species from the boundary, together with Δx and Δt, the fundamental spatial and temporal modelling parameters, as $\rho = (\Delta x - \alpha \Delta t)/(\Delta x + \alpha \Delta t)$. Special cases of the short-circuit ($\rho = -1$), open-circuit ($\rho = 1$) and matched-load ($\rho = 0$) boundaries can be succinctly described by $\alpha \rightarrow \infty$, $\alpha \rightarrow 0$, and $\alpha = \Delta x/\Delta t$, respectively. The generality nature of this representation should ease programming and computational effort especially for problems where the boundary condition may be varied with time.

References

[1] A. G. Sabnis, "Multilevel metallization schemes", in *VLSI Electronics, vol. 15: VLSI Metallization,* edited by N. G. Einspruch, S. S. Cohen, and G. Sh. Gildenblat, Academic Press, Orlando, 1987, pp. 293-343.

[2] G. K. Rao, *Multilevel Interconnect Technology*, McGraw-Hill, New York, 1993.

[3] J. Schutz, "A CMOS 100 MHz microprocessor", *IEEE Int. Solid State Circuits Conf. Dig.*, IEEE, New York, 1991, pp. 91-92.

[4] See, for example, papers contained in *VLSI Metallizations: Reliability & Technologies*, edited by K. Shenai, Artech House, Boston, 1991.

[5] E. K. Broadbent (editor), *Tungsten and Other Refractory Metals for VLSI Applications*, Materials Research Society, Pittsburgh, 1987.

[6] F. M. d'Heurle and P. S. Ho, "Electromigration in thin films", in *Thin Films—Interdiffusion & Reactions*, edited by J. M. Poate, K. N. Tu, and J. W. Mayer. Wiley, New York, 1978, pp. 243-303.

[7] D. Pramanik and A. N. Sexena, "VLSI metallization using aluminum and its alloys: Part I", *Solid St. Technol.*, vol. 26, no. 1, pp. 127-133, 1983.

[8] D. Pramanik and A. N. Sexena, "VLSI metallization using aluminum and its alloys: Part II", *Solid St. Technol.*, vol. 26, no. 3, pp. 131-138, 1983.

[9] C.-K. Hu, B. Luther, F. B. Kaufman, J. Hummel, C. Uzoh, and D. J. Pearson, "Copper interconnection integration and reliability", *Thin Solid Films*, vol. 262, pp. 84-92, 1995.

[10] P. S. Ho, "General aspects of barrier layers for very-large scale integration applications. I. Concepts", *Thin Solid Films*, vol. 96, pp. 301-316, 1982.

[11] R. S. Nowicki and M.-A. Nicolet, "General aspects of barrier layers for very-large scale integration applications. II. Practice", *Thin Solid Films*, vol. 96, pp. 317-326, 1982.

[12] H. P. Kattelus and M.-A. Nicolet, "Diffusion barriers in semiconductor contact metallization", in *Diffusion Phenomena in Thin Films and Microelectronic Materials*, edited by D. Gupta and P. S. Ho, Noyes, Park Ridge, NJ, 1988, pp. 432-498.

[13] J. Hems, "Barrier layers: the advantages of titanium nitride", *Semicond. Int.*, vol. 13, no. 12, pp. 100-102, 1990.

[14] D. L. Smith, "Evaporation", in *Thin-Film Deposition*, McGram-Hill, New York, 1995, pp. 63-118.

[15] D. W. Skelly, T. M. Lu, and D. W. Woodruff, "Metallization techniques", in *VLSI Electronics, vol. 15: VLSI Metallization,* edited by N. G. Einspruch, S. S. Cohen, and G. Sh. Gildenblat, Academic, Orlando, 1987, pp. 101-157.

[16] A. Sherman, *Chemical Vapor Deposition for Microelectronics*, Noyes, Park Ridge, New Jersey, 1987.

[17] R. N. Singh, "Metallurgical properties of thin conducting films", in *VLSI Electronics, vol. 15: VLSI Metallization,* edited by N. G. Einspruch, S. S. Cohen, and G. Sh. Gildenblat, Academic, Orlando, 1987, pp. 41-100.

[18] G. B. Gao and X. Gui, "Reliability physics as a new discipline", *Microelectron. Reliab.*, vol. 28, no. 5, pp. 713-720, 1988.

[19] P. S. Ho and T. Kwok, "Electromigration in metals", *Rep. Prog. Phys.*, vol. 52, no. 3, pp. 301-348, 1989.

[20] S.-Y. Oh and K.-J. Chang, "2001 needs for multi-level interconnect technology", *IEEE Circuit & Devices Magazine*, vol. 11, no. 1, pp. 16-21, 1995.

[21] P. Kücher, H. Aochi, J. Gambino, T. Licata, T. Matsuda, S. Nguyen, M. Okazaki, H. Palm, and M. Ronay, "Advanced metallization technology for 256M DRAM", *Applied Surface Science*, vol. 91, pp. 359-366, 1995.

[22] D. Gupta, D. R. Campbell and P. S. Ho, "Grain boundary diffusion", in *Thin Films—Interdiffusion & Reactions*, edited by J. M. Poate, K. N. Tu, and J. W. Mayer, Wiley, New York, 1978, pp. 161-242.

[23] D. Pramanik and V. Jain, "Barrier metals for ULSI: processing and reliability", *Solid St. Technol.*, vol. 34, no. 5, pp. 97-102, 1991.

[24] J. C. Strikwerda, *Finite Difference Schemes and Partial Differential Equations*, Wadsworth & Books/Cole Advanced Books & Software, Pacific Grove, CA, 1989.

[25] O. C. Zienkiewicz and R. L. Taylor, *The Finite Element Method*, 4th ed., McGraw-Hill, New York, 1989.

[26] P. B. Johns, "A simple, explicit, and unconditionally stable numerical routine for the solution of the diffusion equation," *Int. J. Numer. Meth. Eng.*, vol. 11, pp. 1307-1328, 1977.

[27] S. H. Pulko and P. B. Johns, "Modelling of thermal diffusion in three dimensions by the transmission line matrix method and the incorporation of nonlinear thermal properties", *Comms. Appl. Numer. Methods*, vol. 3, pp. 571-579, 1987.

[28] D. de Cogan and M. Henini, "TLM modelling of the thermal behaviour of conducting films on insulating substrates", *J. Phys. D: Appl. Phys.*, vol. 20, pp. 1445-1450, 1987.

[29] X. Gui, P. W. Webb and G. B. Gao, "Use of the three-dimensional TLM method in the thermal simulation and design of semiconductor devices", *IEEE Trans. Electron Devices*, vol. ED-39, no. 6, pp. 1295-1302, 1992.

[30] S. H. Pulko, A. Mallik, R. Allen, and P. B. Johns, "Automatic timestepping in TLM routines for the modelling of thermal diffusion processes", *Int. J. Numer. Model.: Electron. Netw. Devices Fields*, vol. 2, no. 2, pp. 127-136, 1990.

[31] X. Gui, P. W. Webb and D. de Cogan, "An error parameter in TLM diffusion modelling," *Int. J. Numer. Model.: Electron. Netw. Devices Fields*, vol. 5, no. 2, pp. 129-137, 1992.

[32] P. W. Webb and X. Gui, "Implementation of timestep changes in transmission-line matrix diffusion modelling", *Int. J. Numer. Model.: Electron. Netw. Devices Fields*, vol. 5, no. 4, pp. 251-257, 1992.

[33] P. B. Johns, "The art of modelling", *Electronics & Power*, vol. 25, no. 8, pp. 565-569, 1979.

[34] P. B. Johns and R. L. Beurle, "Numerical solution of 2-dimensional scattering problems using a transmission-line matrix", *Proc. IEE*, vol. 118, no. 9, pp. 1203-1208, 1971.

[35] C. Huygens, "Traité de la lumière", Leiden, 1690.

[36] P. B. Johns, "A new mathematical model to describe the physics of propagation", *Radio Electron. Eng.*, vol. 44, no. 12, pp. 657-666, 1974.

[37] W. J. R. Hoefer, "The transmission-line matrix (TLM) method", in *Numerical Techniques for Microwave and Millimeter-Wave Passive Structures*, edited by T. Itoh, Wiley, New York, 1989, pp. 496-591.

[38] W. J. R. Hoefer, "Huygens and the computer—a powerful alliance in numerical electromagnetics", *Proc. IEEE*, vol. 79, no. 11, pp. 1459-1471, 1991.

[39] C. Christopoulos, *The Transmission-Line Modeling Method*, IEEE, New York, and Oxford University Press, Oxford, 1995.

[40] P. B. Johns and G. Butler, "The consistency and accuracy of the TLM method for diffusion and its relationship to existing methods," *Int. J. Numer. Meth. Eng.*, vol. 19, pp. 1549-1554, 1983.

[41] A. H. M. Saleh and P. Blanchfield, "Analysis of acoustics radiation patterns of array transducers using the TLM method", *Int. J. Numer. Model.: Electron. Netw. Devices Fields*, vol. 3, pp. 39-56, 1990.

[42] P. B. Johns and M. O'Brien, "Use of the TLM method to solve non-linear lumped networks", *Radio Electron. Eng.*, vol. 50, no. 1/2, pp. 59-70, 1980.

[43] M. Y. Al-Zeben, A. H. M. Saleh and M. A. Al-Omar, "TLM modelling of diffusion, drift and recombination of charge carriers in semiconductors", *Int. J. Numer. Model.: Electron. Netw. Devices Fields*, vol. 5, no. 4, 219-225, 1992.

[44] P. B. Johns and S. H. Pulko, "Modelling of heat and mass transfer in foodstuffs", in *Food Structure and Behaviour*, edited by J. Blanshard and P. Lillford, Academic, Orlando, 1987, pp. 199-218.

[45] P. Enders and D. de Cogan, "The efficiency of transmission-line matrix modelling — a rigorous viewpoint," *Int. J. Numer. Model.: Electron. Netw. Devices Fields*, vol. 6, no. 2, pp. 109-137, 1992.

[46] Y. Taitel, "On the parabolic, hyperbolic and discrete formulation of the heat conduction equation", *Int. J. Heat Mass Transfer*, vol. 15, pp. 369-371, 1972.

[47] D. de Cogan, P. Enders, and X. Gui, "Impedance transformations and mesh coarsening in TLM heat flow modelling", *Numerical Heat Transfer B*, vol. 21, no. 3, pp. 327-342, 1992.

[48] X. Gui, S. K. Dew, and M. J. Brett, "TLM treatment of a general diffusion flux boundary condition", *Int. J. Numer. Model.: Electron. Netw. Devices Fields*, vol. 9, 1996 (to appear).

[49] X. Gui, L. J. Friedrich, S. K. Dew, M. J. Brett, and T. Smy, "Grain-boundary diffusion modeling and efficiency evaluation of thin-film diffusion barriers considering microstructure effects", *J. Appl. Phys.*, vol. 78, no. 7, pp. 4438-4443, 1995.

[50] X. Gui, S. K. Dew, M. J. Brett, and D. de Cogan, "Transmission-line-matrix modeling of grain-boundary diffusion in thin films", *J. Appl. Phys.*, vol. 74, no. 12, pp. 7173-7180, 1993.

[51] X. Gui and P. W. Webb, "A comparative study of two TLM networks for the modelling of diffusion processes", *Int. J. Numer. Model.: Electron. Netw. Devices Fields*, vol. 6, no. 2, pp. 161-164, 1993.

[52] X. Gui, G. B. Gao, and H. Morkoç, "Transmission-line matrix method for solving the multidimensional continuity equation", *Int. J. Numer. Model.: Electron. Netw. Devices Fields*, vol. 6, no. 3, pp. 233-236, 1993.

[53] C. Y. Chen and H. L. Huang, "Grain boundary diffusion in thin film couples", *J. Vac. Sci. Technol.*, vol. 18, no. 2, pp. 398-400, 1981.

[54] The analytical solution of the boundary value problem (Example 2 on pages 30-31) was obtained more than fifty years ago for a diffusion effect in liquids: S. R. de Groot, "Théorie phénoménologique de l'effet Soret", *Physica*, vol. 9, no. 7, pp. 699-708, 1942. The solution has recently been reused for modelling electromigration process in integrated circuits: J. J. Clement, "Vacancy supersaturation model for electromigration failure under dc and pulsed dc stresses", *J. Appl. Phys.*, vol. 71, no. 9, pp. 4264-4268, 1992.

[55] G. M. Dusinberre, "Transient flow—geometrical subdivisions—one dimension", *Numerical Analysis of Heat Flow*, McGraw-Hill, New York, 1949, pp. 114-147.

[56] D. de Cogan and P. Enders, "Discrete Green's functions and hybrid modelling of thermal and particle diffusion", *Int. J. Numer. Model.: Electron. Netw. Devices Fields*, vol. 7, no. 6, pp. 407-418, 1994.

[57] D. de Cogan and A. K. Shah, "Stub TLM modelling of heat flow in semiconductor devices", *J. Phys. D: Appl. Phys.*, vol. 19, pp. 721-725, 1986.

[58] S. H. Pulko, A. Mallik, and P. B. Johns, "Application of transmission-line modelling (TLM) to thermal diffusion in bodies of complex geometry", *Int. J. Numer. Meth. Eng.*, vol. 23, pp. 2303-2312, 1986.

[59] C. C. Wong and W. S. Wong, "Multigrid TLM for diffusion problems", *Int. J. Numer. Model.: Electron. Netw. Devices Fields*, vol. 2, pp. 103-111, 1989.

[60] R. Ait-Sadi, A. J. Lowery, and B. Tuck, "Combined fine-coarse mesh transmission-line modelling method for diffusion problems", *Int. J. Numer. Model.: Electron. Netw. Devices Fields*, vol. 3, pp. 111-126, 1990.

[61] S. H. Pulko, I. A. Halleron, and C. P. Phizacklea, "Substructuring of space and time in TLM diffusion applications", *Int. J. Numer. Model.: Electron. Netw. Devices Fields*, vol. 3, pp. 207-214, 1990.

[62] P. W. Webb and I. A. D. Russell, "Application of the TLM method to transient thermal simulation of microwave power transistors", *IEEE Trans. Electron Devices*, vol. ED-42, no. 4, pp. 624-631, 1995.

[63] S. M. Sze, *Physics of Semiconductor Devices*, 2nd ed., Wiley, New York, 1981, p. 51.

[64] X. Gui, G. B. Gao, and H. Morkoç, "Simulation study of peak junction temperature and power limitation of AlGaAs/GaAs HBT's under pulsed and CW operation", *IEEE Electron Device Lett.*, vol. EDL-13, no. 8, pp. 411-413, 1992.

[65] D. de Cogan and P. Enders, "Microscopic effects in TLM heat flow modelling", *IEE Colloquium on "Transmission-Line Matrix Modelling"*, Digest No. 1991/157, pp. 8/1-8/11, London, Oct. 1991.

[66] D. de Cogan and A. K. Shah, "A two-dimensional transmission line matrix model for heat flow in power semiconductors" *J. Phys. D: Appl. Phys.*, vol. 18, pp. 507-516, 1985.

[67] X. Gui, S. K. Dew, and M. J. Brett, "Three-dimensional thermal analysis of high density triple-level interconnection structures in very large scale integrated circuits", *J. Vac. Sci. Technol. B*, vol. 12, no. 1, pp. 59-62, 1994.

[68] P. A. Flinn, A. S. Mack, P. R. Besser, and T. N. Marieb, "Stress-induced void formation in metal lines", *MRS Bulletin*, vol.18, no. 12, pp. 26-35, 1993.

[69] T. Kwok, T. Nguyen, P. S. Ho, and S. Yip, "Current density and temperature distribution in multilevel interconnection with studs and vias", *Proc. 25th Int. Reliab. Phys. Symp.*, IEEE, New York, 1987, pp. 130-133.

[70] W. Allegretto, A. Nathan, K. Chau, and H. P. Baltes, "Two-dimensional numerical simulations of electrothermal behaviour in very large scale integrated contacts and vias", *Can. J. Phys.*, vol. 67, no. 4, pp. 212-217, 1989.

[71] F. Matsuoka, H. Iwai, K. Hama, H. Itoh, R. Nakata, T. Nakakubo, K. Maeguchi, and K. Kanzaki, "Electromigration reliability for a tunsten-filled via hole structure", *IEEE Trans. Electron Devices*, vol. ED-37, no. 3, pp. 562-568, 1990.

[72] K. Weide and W. Hasse, "Three-dimensional simulations of temperature and current density distribution in a via structure", *Proc. 30th Int. Reliab. Phys. Symp.*, IEEE, New York, 1992, pp. 361-365.

[73] J. T. Trattles, A. G. O'Neill, and B. C. Mecrow, "Three-dimensional finite-element investigation of current crowding and peak temperatures in VLSI multilevel interconnections", *IEEE Trans. Electron Devices*, vol. ED-40, no. 7, pp. 1344-1347, 1993.

[74] T. Smy, D. J. Reny and M. J. Brett, "Simulation of the effect of thin film microstructure on current and temperature distributions in very large scale integrated metallization structures", *J. Vac. Sci. Technol. B*, vol. 10, no. 5, pp. 2267-2276, 1992.

[75] P. W. Webb and I. A. D. Russell, "Thermal simulation of transients in microwave devices", *IEE Proc.-G*, vol. 138, no. 5, pp. 329-334, 1991.

[76] P. W. Webb, "Thermal modeling of power gallium arsenide microwave integrated circuits", *IEEE Trans. Electron Devices*, vol. ED-40, no. 5, pp. 867-877, 1993.

[77] M. Wittmer, "Barrier layers: principles and applications in microelectronics", *J. Vac. Sci. Technol. A*, vol. 2, no. 2, pp. 273-280, 1984.

[78] K. G. Steiner, C. S. Pai, R. M. Stanton, and C. W. Wilkins, "Comprehensive characterization of reliable PECVD silicon oxynitride process", *Proc. 10th VLSI Multilevel Interconnection Conf.*, IEEE, New York, 1993, pp. 78-83.

[79] A. N. Saxena and M. A. Bourgeois, "Thermal conductivity of thin dielectric films and its impact on multilevel metallizations", *Proc. 10th VLSI Multilevel Interconnection Conf.*, IEEE, New York, 1993, pp. 251-257.

[80] J. R. Black, "Electromigration—a brief survey and some recent results", *IEEE Trans Electron Devices*, vol. ED-16, no. 4, pp. 338-347, 1969.

[81] J. R. Black, "Electromigration failure modes in aluminum metallization for semiconductor devices", *Proc. IEEE*, vol. 57, no. 9, pp. 1587-1593, 1969.

[82] X. Gui, S. K. Dew, and M. J. Brett, "Thermal simulation of thin-film interconnect failure caused by high current pulses", *IEEE Trans. Electron Devices*, vol. ED-47, no.7, pp. 1386-1388, 1995.

[83] X. Gui, S. K. Dew, and M. J. Brett, "Thermal simulation of energetic transients in multilevel metallisation systems", *Electron Lett.*, vol. 31, no. 22, pp. 1954-1956.

[84] J. S. Suehle and H. A. Schafft, "The electromigration damage response time and implications for DC and pulsed characteristics", *Proc. 27th Int. Reliab. Phys. Symp.*, IEEE, New York, 1989, pp. 220-228.

[85] J. Tao, N. W. Cheung, and C. Hu, "Electromigration failure model for interconnects under pulsed and bi-directional current stressing", *IEEE Trans. Electron Devices*, vol. ED-41, no. 4, pp. 539-545, 1994.

[86] D. G. Pierce, E. S. Snyder, S. E. Swanson, and L. W. Irwin, "Wafer-level pulsed-DC electromigration response at very high frequencies", *Proc. 32th Int. Reliab. Phys. Symp.*, IEEE, New York, 1994, pp. 198-206.

[87] E. Hamdy, J. McCollum, S. Chen, S. Chiang, S. Eltoukhy, J. Chang, T. Speers, and A. Mohsen, "Dielectric based antifuse for logic and memory ICs", in *IEDM Tech. Dig.*, IEEE, New York, 1988, pp. 786-789.

[88] S. S. Cohen, J. I. Raffel, and P. W. Wyatt, "A novel double-metal structure for voltage-programmable links", *IEEE Electron Device Lett.*, vol. EDL-13, no. 9, pp. 488-490, 1992.

[89] J. E. Murguia and J. B. Bernstein, "Short-time failure of metal interconnect caused by current pulses", *IEEE Electron Device Lett.*, vol. EDL-14, no. 10, pp. 481-483, 1993.

[90] K. Y. Kim and W. Sachse, "Dynamic fracture test of metal thin films deposited on an insulating substrate by a high current pulse method", *Thin Solid Films*, vol. 205, no. 2, pp. 176-181, 1991.

[91] J. M. Towner, A. G. Dirks, and T. Tien, "Electromigration in titanium doped aluminum alloys", *Proc. 24th Int. Reliab. Phys. Symp.*, IEEE, New York, 1986, pp. 7-11.

[92] J. C. Hwang, P. S. Ho, J. E. Lewis, and D. R. Campbell, "Grain boundary diffusion of aluminum in polycrystalline silicon films", *J. Appl. Phys.*, vol. 51, no. 3, pp. 1576-1581, 1980.

[93] A. D. Buonaquisti, W. Carter, and P. H. Holloway, "Diffusion characteristics of boron and phosphorous in polycrystalline silicon", *Thin Solid Films*, vol. 100, pp. 235-248,1983.

[94] D. L. Losee, J. P. Lavine, E. A. Trabka, S.-T. Lee, and C. M. Jarman, "Phosphorus diffusion in polycrystalline silicon", *J. Appl. Phys.*, vol. 55, no. 4, pp. 1218-1220, 1984.

[95] A. G. O'Neill, C. Hill, J. King, and C. Please, "A new model for the diffusion of arsenic in polycrystalline silicon", *J. Appl. Phys.*, vol. 64, no. 1, pp. 167-174, 1988.

[96] J. Pelleg and S. P. Murarka, "Phosphorus distribution in $TaSi_2$ films by diffusion from a polycrystalline silicon", *J. Appl. Phys.*, vol. 54, no. 3, pp. 1337-1345, 1983.

[97] J. C. Fisher, "Calculation of diffusion penetration curve for surface and grain boundary diffusion", *J. Appl. Phys.*, vol. 22, no. 1, pp. 74-77, 1951.

[98] R. T. P. Whipple, "Concentration contours in grain boundary diffusion", *Phil. Mag.*, vol. 45, pp. 1225-1136, 1954.

[99] T. Suzuoka, "Lattice and grain boundary diffusion in polycrystals", *Trans. Jpn. Institute Metall.*, vol. 2, p. 25, 1961.

[100] G. H. Gilmer and H. H. Farrell, "Grain-boundary diffusion in thin films. I: The isolated grain boundary", *J. Appl. Phys.*, vol. 47, no. 9, pp. 3792-3798, 1976.

[101] G. H. Gilmer and H. H. Farrell, "Grain-boundary diffusion in thin films. II: Multiple grain boundaries and surface diffusion", *J. Appl. Phys.*, vol. 47, no.10, pp. 4373-4380, 1976.

[102] J. C. Hwang and R. W. Balluffi, "Measurement of grain-boundary diffusion at low temperatures by the surface accumulation method. I: Method and analysis", *J. Appl. Phys.*, vol. 50, no. 3, pp. 1339-1348, 1979.

[103] J. C. Hwang, J. D. Pan, and R. W. Balluffi, "Measurement of grain-boundary diffusion at low temperatures by the surface accumulation method. II: Results for gold-silver system", *J. Appl. Phys.*, vol. 50, no. 3, pp. 1349-1359, 1979.

[104] J. Unnam, J. A. Carpenter and C. R. Houska, "X-ray diffraction approach to grain boundary and volume diffusion", *J. Appl. Phys.*, vol. 44, no. 5, pp. 1957-1967, 1973.

[105] P. H. Holloway, D. E. Amos and G. C. Nelson, "Analysis of grain-boundary diffusion in thin films: Chromium in gold", *J. Appl. Phys.*, vol. 47, no. 9, pp. 3769-3775, 1976.

[106] D. Gupta, "Some formal aspects of diffusion: bulk solids and thin films", in *Diffusion Phenomena in the Thin Films and Microelectronic Materials*, edited by D. Gupta and P. S. Ho, Noyes, Park Ridge, NJ, 1988, pp. 1-72.

[107] W. Krakow and D. A. Smith, "The observation of various grain boundary atomic structure in Au by high-resolution electron microscopy", *J. Mater. Res.*, vol. 1, no. 1, pp. 47-59, 1986; also, see Figure 13.1 in *Electronic Thin Film Science for Electrical Engineers and Materials Scientists*, edited by K.-N. Tu, J. W. Mayer, and L. C. Feldman, Macmillan, New York, 1993, p. 336.

[108] C. Kittel, *Introduction to Solid State Physics*, 5th ed., John Wiley & Sons, New York, 1976, pp. 542-543.

[109] S. D. Mukherjee, D. V. Morgan and M. J. Howes, "Interdiffusion and degradation of Si/Cr/Pt/Ag IMPATT diode metallization", *J. Electrochem. Soc.*, vol. 126, pp. 1047-1053, 1979.

[110] P. M. Hall and J. M. Morabito, "Diffusion problems in microelectronics packaging", *Thin Solid Films*, vol. 53, pp. 175-182, 1978.

[111] L. G. Harrison, "Influence of dislocations on diffusion kinetics in solids with particular reference to the alkali halides", *Trans. Faraday Soc.*, vol. 57, pp. 1191-1199, 1961.

[112] N. L. Peterson, "Diffusion mechanisms and structural effects in grain boundaries", *J. Vac. Sci. Technol. A*, vol. 4, no. 6, pp. 3066-3070, 1986.

[113] X. Gui, S. K. Dew, and M. J. Brett, "Three-dimensional simulation of impurity diffusion in thin-film diffusion barriers", *J. Electron. Mater.*, vol. 23, no. 12, pp. 1309-1314, 1994.

[114] J. Kucera, B. Million, J. Zidu, and V. Hermansky, "Resistance change in thin film integrated circuits caused by interdiffusion", *Thin Solid Films*, vol. 230, no. 2, pp. 183-190, 1993.

[115] E. Kobeda, J. D. Warnock, J. P. Gambino, S. B. Brodsky, B. Cunningham, and S. Basavaiah, "Diffusion barrier properties of TiN films for submicron silicon bipolar technologies", *J. Appl. Phys.*, vol. 72, no. 7, pp. 2743-2748, 1992.

[116] T. Kikkawa, H. Aoki, E. Ikawa, and M. Drynan, "A quarter-micrometer interconnection technology using a TiN/Al-Si-Cu/TiN/Al-Si-Cu/TiN/Ti multilayer structure", *IEEE Trans. Electron Devices*, vol. ED-40, no. 2, pp. 296-302, 1993.

[117] K. G. Grigorov, G. I. Grigorov, M. Stoyanova, J. L. Vignes, J. P. Langeron, P. Denjean, and J. Perriere, "Diffusion of silicon in titanium nitride films: Efficiency of TiN barrier layers", *Appl. Phys. A*, vol. 55, no. 5, pp. 502-504, 1992.

[118] G. I. Grigorov, K. G. Grigorov, M. Stoyanova, J. L. Vignes, J. P. Langeron, and P. Denjean, "Aluminum diffusion in titanium nitride films: Efficiency of TiN barrier layers", *Appl. Phys. A*, vol. 57, no. 3, pp. 195-197, 1993.

[119] J. D. Hodge, "A Monte Carlo solution to the problem of diffusion in grain boundaries", *J. Am. Ceram. Soc.* vol. 74, no. 4, pp. 823-829, 1991.

[120] X. Gui, S. K. Dew, and M. J. Brett, "Simulation of electromigration in thin-film diffusion barriers by the transmission-line matrix method", *J. Vac. Sci. Technol. B*, vol. 13, no. 5, pp. 2100-2104, 1995.

[121] I. A. Blech, "Electromigration in thin aluminum films on titanium nitride", *J. Appl. Phys.*, vol. 47, no. 4, pp. 1203-1208, 1976.

[122] S. Vaidya, T. T. Sheng, and A. K. Sinha, "Linewidth dependence of electromigration in evaporated Al-0.5% Cu", *Appl. Phys. Lett.*, vol. 36, pp. 464-466, 1980.

[123] C. V. Thompson and J. Cho, "A new electromigration testing technique for rapid statistical evaluation of interconnect technology", *IEEE Electron Device Lett.*, vol. EDL-7, no. 12, pp. 667-668, 1986.

[124] M. A. Konhonen, P. Bϕrgesen, K. N. Tu, and C.-Y. Li, "Stress evolution due to electromigration in confined metal lines", *J. Appl. Phys.*, vol. 73, no. 8, pp. 3790-3799, 1993.

[125] M. L. Dreyer, K. Y. Fu, and C. J. Varker, "An electromigration model that includes the effects of microstructure and temperature on mass transport", *J. Appl. Phys.*, vol. 73, no. 10, pp. 4894-4902, 1993.

[126] J. S. May, "Electromigration characteristics of vias in Ti:W/Al-Cu(2%) multilayered metallization", *Proc. 29th Int. Reliab. Phys. Symp.*, IEEE, New York, 1991, pp. 91-96.

[127] K. L. Tai and M. Ohring, "Grain-boundary electromigration in thin films. I. Low-temperature theory", *J. Appl. Phys.*, vol. 48, no. 1, pp. 28-35, 1977.

[128] K. L. Tai and M. Ohring, Grain-boundary electromigration in thin films. II. Tracer measurements in pure Au", *J. Appl. Phys.*, vol. 48, no. 1, pp. 36-45, 1977.

[129] P. S. Ho, "Analysis of grain-boundary electromigration", *J. Appl. Phys.*, vol. 49, no. 5, pp. 2735-2742, 1978.

[130] X. Gui, L. J. Friedrich, S. K. Dew, M. J. Brett, and T. Smy, "TLM modeling of grain-boundary diffusion in thin films with microstructural details", *Proc. 1st*

Int. Workshop Transmission-Line Matrix (TLM) Modeling—Theory and Applications, Vitoria, BC, Canada, 1995, pp. 129-132.

[131] J. P. Lavine and D. L. Losee, "Monte Carlo treatment of impurity diffusion in polycrystalline films", *J. Appl. Phys.*, vol. 56, no. 4, pp. 924-926, 1984; *ibid.* vol. 58, p. 4483 (Erratum), 1985.

[132] J. P. Lavine, "Monte Carlo simulation of impurity diffusion in thin-film diffusion barriers", *J. Appl. Phys.* vol. 59, no. 6, pp. 1986-1991, 1986.

[133] L. J. Friedrich, S. K. Dew, M. J. Brett, and T. Smy, "Thin film microstructure modelling through line-segment simulation", *Thin Solid Films*, vol. 266, no. 1, pp. 83-88, 1995.

[134] P. K. Swaminathan, C. S. Murthy, and M. J. Redmon, "Computer simulations of epitaxial growth", *Phys. Rev. B*, vol. 39, no. 7, pp. 4541-4547, 1989.

[135] P. Meakin, P. Ramanlal, L. M. Sander, R. C. Ball, "Ballistic deposition on surfaces", *Phys. Rev. A*, vol. 34, no. 6, pp. 5091-5103, 1986.

[136] M. J. Brett, "Structural transitions in ballistic aggregation simulation of thin-film growth", *J. Vac. Sci. Technol. A*, vol. 6, no. 3, pp. 1749-1751, 1988.

[137] S. K. Dew, T. Smy, and M. J. Brett, "Simulation of elevated temperature aluminum metallization using SIMBAD", *IEEE Trans. Electron Devices*, vol. ED-39, no. 7, pp. 1599-1606, 1992.

[138] C. H. Ting and A. R. Neureuther, "Application of profile simulation for thin film deposition and etching processes", *Solid St. Technol.*, vol. 25, no. 2, pp. 115-123, 1982.

[139] S. Lichter and J. Chen, "Model for columnar microstructure of thin solid films", *Phys. Rev. Lett.*, vol. 56, no. 13, pp. 1396-1399, 1986.

[140] D. J. Srolovitz, "Grain growth phenomena in films: a Monte Carlo approach", *J. Vac. Sci. Technol. A*, vol. 4, no. 6, pp. 2925-2931, 1986.

[141] D. S. Gardner, J. D. Meindl, and K. C. Saraswat, "Interconnection and electromigration scaling theory", *IEEE Trans. Electron Devices*, vol. ED-34, no. 3, pp. 633-643, 1987.

[142] Y.-W. Yi, K. Ihara, M. Saitoh, and N. Mikoshiba, "Electromigration-induced integration limits on the future ULSI's and the beneficial effects of lower operation temperatures", *IEEE Trans. Electron Devices*, vol. ED-42, no. 4, pp. 683-688, 1995.

[143] J. J. Clement, C. V. Thompson, and A. Enver, "Modeling electromigration-induced stress buildup due to nonuniform temperature", *Mat. Res. Soc. Symp. Proc.*, vol. 338, Materials Research Society, Pittsburgh, PA, 1994, pp. 353-360.

[144] J. J. Clement and C. V. Thompson, "Electromigration-induced stress evolution in confined metal lines", *J. Appl. Phys.*, vol. 78, no. 2, pp. 900-904, 1995.

[145] X. Gui, D. de Cogan, S. K. Dew, and M. J. Brett, "A general expression of boundary conditions in TLM diffusion modelling", *Int. J. Numer. Model.: Electron. Netw. Devices Fields*, submitted for publication, 1996.

[146] A. H. M. Saleh, Private communications, 1992.

[147] X. Gui *et al.*, "Numerical solution of the electromigration boundary value problem under pulsed dc conditions", manuscript in preparation.

Vita and Publication List

Vita

Xiang Gui received the B.Sc. (1982) and M.Sc. (1988) degrees from Beijing Polytechnic University, China, and expects to receive the Ph.D. degree (spring 1996) from the University of Alberta, Canada, all in electrical engineering. He was a lecturing staff in the Electronic Engineering Department at Beijing Polytechnic University, China (09/82 - 08/90), a Visiting Research Fellow in the School of Electronic and Electrical Engineering at the University of Birmingham, U.K. (09/90 - 01/92), and a Visiting Scholar in the Coordinated Science Laboratory and Materials Research Laboratory at the University of Illinois at Urbana-Champaign, U.S.A. (01/92 - 01/93). His research interests are in transmission-line matrix (TLM) diffusion modeling, thin-film metallization studies, reliability physics, failure mechanism modeling, and thermal simulation and design of semiconductor devices. He has published more than 30 technical papers in referred international journals and conference proceedings.

Publication List

I. Refereed Journal Publications:

1. **X. Gui** *et al.*, "Numerical solution of the electromigration boundary value problem under pulsed dc conditions", manuscript in preparation.

2. **X. Gui**, D. de Cogan, S. K. Dew, and M. J. Brett, "A general expression of boundary conditions in TLM diffusion modelling", *Int. J. Numer. Model.: Electron. Netw. Devices Fields*, submitted for publication.

3. **X. Gui,** S. K. Dew, and M. J. Brett, "TLM treatment of a general diffusion flux boundary condition", *Int. J. Numer. Model.: Electron. Netw. Devices Fields*, vol. 9, 1996 (to appear).

4. **X. Gui**, S. K. Dew, and M. J. Brett, "Thermal simulation of energetic transients in multilevel metallisation systems", *Electron. Lett.*, vol. 31, no. 22, pp. 1954-1956, Oct. 1995.

5. **X. Gui**, L. J. Friedrich, S. K. Dew, M. J. Brett, and T. Smy, "Grain-boundary diffusion modeling and efficiency evaluation of thin-film diffusion barriers considering microstructure effects", *J. Appl. Phys.*, vol. 78, no. 7, pp. 4438-4443, Oct. 1995.

6. **X. Gui**, S. K. Dew, and M. J. Brett, "Simulation of electromigration in thin-film diffusion barriers by the transmission-line matrix method", *J. Vac. Sci. Technol. B*, vol. 13, no. 5, pp. 2100-2104, Sept./Oct. 1995.

7. **X. Gui**, S. K. Dew, and M. J. Brett, "Thermal simulation of thin-film interconnect failure caused by high current pulses", *IEEE Trans. Electron Devices*, vol. ED-42, no. 7, pp. 1386-1388, July 1995.

8. **X. Gui**, S. K. Dew, and M. J. Brett, "Three-dimensional simulation of impurity diffusion in thin-film diffusion barriers", *J. Electron. Mater.*, vol. 23, no. 12, pp. 1309-1314, Dec. 1994.

9. **X. Gui**, G. B. Gao, and H. Morkoç, "The effects of surface metallization on the thermal behavior of GaAs microwave power devices", *IEEE Trans. Microwave Theory Tech.*, vol. MTT-42, no. 2, pp. 342-344, Feb. 1994.

10. **X. Gui**, S. K. Dew, and M. J. Brett, "Three-dimensional thermal analysis of high density triple-level interconnection structures in very large scale integrated circuits", *J. Vac. Sci. Technol. B*, vol. 12, no. 1, pp. 59-62, Jan./Feb. 1994.

11. **X. Gui**, S. K. Dew, M. J. Brett, and D. de Cogan, "Transmission-line-matrix modeling of grain-boundary diffusion in thin films", *J. Appl. Phys.*, vol. 74, no. 12, pp. 7173-7180, Dec. 1993.

12. **X. Gui**, G. B. Gao, and H. Morkoç, "Transmission-line matrix method for solving the multidimensional continuity equation", *Int. J. Numer. Model.: Electron. Netw. Devices Fields*, vol. 6, no. 3, pp. 233-236, Aug. 1993.

13. F. Y. Huang, A. Salvador, **X. Gui**, N. Teraguchi, and H. Morkoç, "Resonant-cavity GaAs/InGaAs/AlAs photodiods with a periodic absorber structure", *Appl. Phys. Lett.*, vol. 63, no.2, pp. 141-143, July 1993.

14. Z. Wang, M. E. Lin, D. Biswas, B. Mazhari, N. Teraguchi, Z. Fan, **X. Gui**, and H. Morkoç, "Si_3N_4/Si/*n*-GaAs capacitor with minimum interface density in the 10^{10} eV^{-1} cm^{-2} range", *Appl. Phys. Lett.*, vol. 62, no. 23, pp. 2977-2979, June 1993.

15. **X. Gui** and P. W. Webb, "A comparative study of two TLM networks for the modelling of diffusion processes", *Int. J. Numer. Model.: Electron. Netw. Devices Fields*, vol. 6, no. 2, pp. 161-164, May 1993.

16. P. W. Webb and **X. Gui**, "Implementation of timestep changes in transmission-line matrix diffusion modelling", *Int. J. Numer. Model.: Electron. Netw. Devices Fields*, vol. 5, no. 4, pp. 251-257, Nov. 1992.

17. **X. Gui**, G. B. Gao, and H. Morkoç, "Simulation study of peak junction temperature and power limitation of AlGaAs/GaAs HBTs under pulsed and CW operation", *IEEE Electron Device Lett.*, vol. EDL-13, no. 8, pp. 411-413, Aug. 1992.

18. **X. Gui**, P. W. Webb, and G. B. Gao, "Use of the three-dimensional TLM method in the thermal design and simulation of semiconductor devices", *IEEE Trans. Electron Devices*, vol. ED-39, no. 6, pp. 1295-1302, June 1992.

19. D. de Cogan, P. Enders, and **X. Gui**, "Impedance transformations and mesh coarsening in TLM heat flow modelling", *Numerical Heat Transfer B*, vol. 21, no. 3, pp. 327-342, May-June 1992.

20. **X. Gui**, P. W. Webb, and D. de Cogan, "An error parameter in TLM diffusion modelling", *Int. J. Numer. Model.: Electron. Netw. Devices Fields*, vol. 5, no. 2, pp. 129-137, May 1992.

21. **X. Gui**, M. Z. Wang, and G. B. Gao, "Monte Carlo simulation for improving electro-migration lifetime by balancing temperature and structural gradients", *Microelectron. Reliab.*, vol. 31, no. 2/3, pp. 389-400, Feb.-Mar. 1991.

22. A. Chen, **X. Gui,** and G. B. Gao, "Modelling of thermal fatigue failure in soft-soldered semiconductor devices using the internal variable method", *Microelectron. Reliab.*, vol. 30, no. 5, pp. 839-843, May 1990.

23. G. B. Gao, M. Z. Wang, **X. Gui**, and H. Morkoç, "Thermal design studies of high power heterojunction bipolar transistors", *IEEE Trans. Electron Devices*, vol. ED-36, no. 5, pp. 854-863, May 1989.

24. G. B. Gao and **X. Gui**, "Reliability physics as a new discipline", *Microelectron. Reliab.*, vol. 28, no. 5, pp. 713-720, May 1988.

25. **X. Gui**, "Book review: Reliability Physics of Semiconductor Devices", *IEEE Trans. Reliab.*, vol. R-36, no. 5, p. 550, Dec. 1987.

26. **X. Gui**, W. C. Wu, and G. B. Gao, "An improved model of thermal stresses in power transistors", *Acta Electron. Sin.*, vol. 14, no. 3, pp. 123-125, May 1986.

II. Papers in Refereed Conference Proceedings:

27. **X. Gui**, L. J. Friedrich, S. K. Dew, M. J. Brett, and T. Smy, "TLM modeling of grain-boundary diffusion in thin films with microstructural details", *Proc. 1st Int. Workshop Transmission-Line Matrix (TLM) Modeling—Theory and Applications* (Vitoria, BC, Canada), pp. 129-132, Aug. 1995.

28. C. Z. Lu, M. Z. Wang, **X. Gui**, G. B. Gao, and B. J. Yi, "Fast measurement of the peak junction temperature of power transistors using the electrical method", *Proc. 7th Ann. Symp. Semicond. Temperature & Thermal Management* (Phoenix, AZ, USA), pp. 39-43, Feb. 1991.

29. C. Z. Lu, M. Z. Wang, **X. Gui**, and G. B. Gao, "Studies on non-destructive electrical technique for measuring the peak junction temperature of power transistors", *Proc. 5th Ann. Symp. CIE R&QC Society* (Xi'an, China), pp. 175-180, May 1990.

30. G. B. Gao and **X. Gui**, "The effect of metallization system on chip temperature distribution", *Proc. 4th Int. Conf. Interconnection Technol. Electronics* (Fellbach, West Germany), pp. 119-121, Feb. 1988.

31. **X. Gui** and G. B. Gao, "A study of electrical overstress effect on thin film metallizations", *Proc. 1st Int. Symp. Physical & Failure Analysis of ICs* (Singapore), pp. 130-135, Oct. 1987.

32. G. B. Gao, W. C. Wu, **X. Gui**, J. J. Zhu, and M. Miao, "Measurement of temperature distribution on semiconductor chip using infra-red micro imager", *Proc. Int. Conf. Semicond. & IC Technology* (Beijing, China), pp. 664-667, Oct. 1986.

33. G. B. Gao, A. Chen, and **X. Gui**, "A layer damage model for calculating thermal fatigue lifetime of power devices", *Proc. 24th IEEE Int. Reliab. Phys. Symp.* (Anaheim, California, USA), pp. 79-86, Apr. 1986.

34. **X. Gui**, "Electromigration in thin film conductors", presented at *the 2nd Ann. Symp. Reliab. Res. Society, Chinese Electrotechnical Institute* (Beijing, China), Jan. 1985.

III. Translated Book and Articles (from English into Chinese)

- *Reliability and Degradation: Semiconductor Devices and Circuits* (edited by M. J. Howes and D. V. Morgan, Wiley, New York, 1981. 444 pages), translated by J. L. Li *et al.*, revised by **X. Gui**, Science Press, Beijing, China, 1989.
- About 20 translated articles have been published in several Chinese journals.

University of Alberta Library
0 1620 0487 2238
B45250